Inferring Parafoil Glide Slope by Extending Unsettled Trajectories via Simulation

Roberto Gomes
Supervisor: Prof. C. Redelinghuys

A dissertation submitted to the Department of Mechanical Engineering at the University of Cape Town, in partial fulfilment of the requirements for the degree of Master of Science in Mechanical Engineering

July, 2014
Cape Town, South Africa

Declaration

1. I know that plagiarism is wrong. Plagiarism is to use another's work and pretend that it is one's own.
2. I have used the *ISO 690 - Numerical Reference* convention for citation and referencing. Each significant contribution to, and quotation in, this dissertation from the work(s) of other people has been attributed, and has been cited and referenced.
3. This dissertation is my own work.
4. I have not allowed, and will not allow anyone to copy my work with the intention of passing it off as his or her own work.

Signature .....

Abstract

A unique catapult has been developed at the University of Cape Town for launching parafoils from a hilltop or into a quarry. The initial objective to determine optimum glide slope of a parafoil using Design of Experiments via flight testing presented challenges. The flight tests and supporting simulations were carefully planned, and were to be conducted by making use of Design of Experiments to investigate the influence of factor effects on glide slope. The two factors to be investigated were the trim settings; plumb line length and trim angle. Each of these factors was to be tested at three discrete levels and it was decided that a 3^2 factorial will be used with the aid of Taguchi's methods. Due to serious flight test damages to the parafoil canopy, lines and payload, it was deemed necessary to revise the project objectives. The required repairs implied that testing could not continue within an acceptable period of time. The revised objective of this project was to ascertain if unsettled trajectory measurements could be extended by means of simulation to infer the steady glide slope.

In order to conduct the simulations required, a rudimentary theoretical model of the unsteady parafoil motion was developed to investigate the influence of line length and trim angle on glide slope. The aerodynamic model focused only on the longitudinal motion of the parafoil-payload system, however the effects of wind and atmospheric turbulence were also investigated. The experimental flight tests in the quarry were unsuccessful due to flight test damages sustained and the focus of this investigation shifted to simulated results rather than experimental results. The simulated results suggest that increasing the plumb line length or the trim angle results in an increase in the settled glide angle of the system. On average, trim angle had a 2-3 times greater effect on glide angle than plumb line length. In addition, due to the lack of sufficient height in the quarry, simulations were run to extend the unsettled trajectory to a steady state in an attempt to estimate the glide angle. These simulations were capable of estimating a settled glide angle with reasonable accuracy in certain atmospheric conditions.

Acknowledgements

I would like to express my sincere gratitude to my supervisor Prof. Chris Redelinghuys for his full support, advice, expert guidance, understanding and continuous encouragement throughout the duration of my research. His contributions to this project are truly appreciated, and without it this dissertation would not have been made possible. I would also like to thank the National Aerospace Centre (NAC) and UCT's University Research Committee (URC) for their financial support.

To my fellow colleagues who were apart of this research project; Jordan Adams, Steven Rhodes, Gideon van der Kolf, Attie Grunwald, Tracy Booysen and Donal Phair: I thank them for their assistance, guidance and advice during the last two years; and for making my time on this research project an overall enjoyable experience. In addition, I would like to thank Douw Grobler, the surveyor who joined us during flight tests.

I would like to extend my gratitude to the Principal Technical Officer of the University of Cape Town Workshop, Glen Newins, and his fellow technicians in the Mechanical Engineering department for their expertise in manufacturing and machining of some components required for this project. Their willingness to help during the last two years is greatly appreciated.

Finally, I would like to thank my friends and family who encouraged me and supported me throughout the duration of my Masters. Especially my parents and my sister, who have continuously supported me throughout my studies. To my friends, for their patience and understanding, I thank them sincerely.

Roberto Gomes.
July, 2014

Contents

List of Figures

List of Tables

Nomenclature

Symbols

$(\dot{})$	Derivative	
$(\hat{})$	Directional unit vector	
$(\vec{})$	Vector	
$[T]$	Transformation matrix	
α	Angle of attack or incidence	$(^\circ)$
α	Ground roughness exponential coefficient	
AR	Aspect ratio	
β	Angle between trim and chord line	$(^\circ)$
β	Sideslip angle	$(^\circ)$
δ	Deflection or increment	
η	Gaussian noise function	
Γ	Angle between $\vec{V}_H$ and horizontal	$(^\circ)$
γ	Glide angle	$(^\circ)$
μ	Trim angle or rigging angle	$(^\circ)$
μ_s	Dimensionless mass for longitudinal stability	
ω	Angular velocity or angular rate	(rad/s)
ω_n	Undamped natural frequency (dimensionless)	

ϕ	Angle of incidence (alternative notation)	($^\circ$)
ϕ	Roll angle	($^\circ$)
ϕ_c	Suspension line angle of attack	($^\circ$)
ψ	Yaw angle	($^\circ$)
ρ	Air density	(kg/m^3)
σ	Turbulence intensity	(m/s)
τ	Trim angle (alternative notation)	($^\circ$)
θ	Pitch angle	($^\circ$)
θ	Tether angle	($^\circ$)
θ_c	Suspension line pitch angle	($^\circ$)
ζ	Damping ratio	
b	Wing span	(m)
c	Chord length	(m)
C_D	Drag coefficient	
C_L	Lift coefficient	
C_m	Pitching moment coefficient	
C_{D0}	Drag coefficient at zero alpha	
$C_{D\alpha}$	Drag coefficient as function of alpha	$(/rad)$
C_{DL}	Drag coefficient due to lines	
C_{L0}	Lift coefficient at zero alpha	
$C_{L\alpha}$	Lift coefficient as function of alpha	$(/rad)$
C_{m0}	Pitch moment coefficient at zero alpha	
$C_{m\alpha}$	Pitching moment coefficient as function of alpha	$(/rad)$
D	Drag force	(N)
d	Distance	(m)

d	Line diameter	(m)
D_{LR}	"Rotational" line drag force	(N)
D_{LS}	Steady line drag force	(N)
F	Force	(N)
g	Gravitational acceleration	(m/s^2)
h	Height	(m)
I_{yy}	Moment of inertia the y axis	$(kg.m^2)$
k	von Karman's constant	
L	Lift force	(N)
L	Plumb line length	(m)
L	Rolling moment	(Nm)
L	Turbulence scale length	(m)
l	Perpendicular distance from $\vec{F}_P$ line of action to hinge point	(m)
M	Pitching moment	(Nm)
m	Mass	(kg)
N	Yawing moment	(Nm)
n	Number of lines	
p	Roll rate	(rad/s)
q	Dynamic pressure	(Pa)
q	Pitch rate	(rad/s)
R	Mean line length	(m)
r	Yaw rate	(rad/s)
r_H	Distance from payload CG to hinge point	(m)
S	Wing reference area	(m^2)

S_{refpl}	Payload reference area	(m^2)
T	Phugoid period	(s)
T	Sampling time	(s)
U	Axial velocity component	(m/s)
$u*$	Friction velocity	(m/s)
u_g	Longitudinal turbulence velocity	(m/s)
u_w	Wind velocity	(m/s)
u_{20}	Wind speed at 20 feet	(m/s)
V	Airspeed	(m/s)
V	Lateral velocity component	(m/s)
W	Normal velocity component	(m/s)
w	Weight	(N)
w_g	Vertical turbulence velocity	(m/s)
X	Axial force component	(N)
x	Longitudinal coordinate in axis system	
X_{refpl}	Payload reference length	(m)
Y	Lateral force component	(N)
y	Lateral coordinate in axis system	
Z	Normal force component	(N)
z	Normal coordinate in axis system	
z_0	Ground roughness length	(m)
z_g	Height above ground	(m)

Subscripts

$\perp$	Perpendicular

b, B	Body axis
c, C	Canopy
$c/4$	Quarter chord position
g	Turbulent gust
H	Hinge
I	Inertial axis
l	Line
$L1$	Associated with steady line drag
$L2$	Associated with "rotational" line drag
$para$	Parafoil canopy and lines
pay	Payload (alternative notation)
pl	Payload
R	Resultant
s	Payload (alternative notation)
w	Mean wind

Superscripts

B	Body axis
f	Number of factors
I	Inertial axis
T	Transpose
W	Wind axis

Abbreviations

ALDS	Advanced Logistics Delivery System

ANOVA	Analysis of Variance
CAD	Computer-Aided Design
CG	Centre of Gravity
CRV	Crew Return Vehicle
DOE	Design of Experiments
DOF	Degree of Freedom
ERADS	Extended Range Aerial Delivery System
GPADS	Guided Parafoil Delivery System
GPS	Global Positioning System
HMMWV	High Mobility Multi-Purpose Wheeled Vehicle
IMU	Inertial Measurement Unit
ODE	Ordinary Differential Equation
RF	Radio Frequency
RSM	Response Surface Methodology
SLADS	Ship Launched Aerial Delivery System
SRDW	Semi Rigid Deployable Wing
SV	State Vector
UAV	Unmanned Aerial Vehicle
UCT	University of Cape Town

Chapter 1

Introduction

1.1 Subject of and Motivation for Research

In this project, the aim was to infer a parafoil's glide slope by extending unsettled trajectory measurements via simulation. Initially, investigating the systematic adjustment of parafoil trim settings, using Design of Experiments (DOE) and flight testing was to be explored, in an effort to find the trim setting resulting in an optimum glide angle. However, simulations were required to simulate flight in various atmospheric conditions, and to investigate the influence of line length and trim angle on glide slope, as obtaining sufficient data was a concern. Therefore, theoretical modelling of the longitudinal motion of a parafoil system was to be attempted.

1.2 Background to Investigation

Parafoils are unpowered, synthetic fabric wings that achieve flight using aerodynamic lift, and consist of multiple cells that inflate when the parafoil is launched from high ground or from an aircraft. Apart from its use in skydiving and paragliding, parafoils have gained widespread use and importance in the accurate aerial delivery of equipment, medicines or food to remote areas where aircraft cannot land. The parafoil is provided with electronic instrumentation allowing it to steer automatically to a predetermined landing site. Autonomous parafoil systems are also used in the recovery of UAV's (Unmanned Aerial Vehicles), and substantial research is currently being undertaken on the flight behaviour of autonomous parafoil and payload systems.

A unique catapult launcher has been developed at the University of Cape Town for launching parafoils from a hilltop or into a quarry. In addition, al-

though unused in this project, an electronic steering unit for the automated steering of the parafoil system has been developed. Following the development of the catapult for launching parafoils, tests needed to be conducted to verify the functioning of it. The parafoil launcher has been proven to work well in previous research. However, it is widely known that launching at different trim settings influence the glide performance of the parafoil. It was decided that a study be done in an effort to infer the optimum glide slope and trim setting of the parafoil for optimal performance with the steering unit. Therefore, between 2012 and 2014, flight tests were performed by varying various trim settings and implementing Design of Experiments. The flight tests were performed at the Lafarge decommissioned quarry in Durbanville, Western Cape.

It is believed that the research and development currently being undertaken at the University of Cape Town, using this parafoil flight testing system, will pave the way in developing low-cost systems that meet the basic accuracy demands.

1.3 Research Objectives

The objectives of this research are therefore:

1. Original:

   (a) The determining of the optimum glide slope of a parafoil cost effectively using DOE via flight testing.

   (b) To develop a theoretical model capable of simulating the aerodynamics of a parafoil system to support flight test results to infer glide slope.

   The initial objective to determine optimum glide slope using DOE via flight testing presented challenges, not in the approach to implement DOE, but with unfortunate circumstances regarding flight testing. The windy weather combined with the swirling effect this creates in the quarry where testing commenced, hampered the progress. Serious damages to the parafoil canopy, lines and payload resulted in many repairing delays. With the time costs associated with flight testing beginning to escalate, a recommended alternative proposed by the supervisor was made. However, despite objectives changing, substantial work was done on the original objectives and hence presented in this document.

2. Modified:

   (a) To investigate the influence of line length and trim angle on glide slope via simulation of flight in various atmospheric conditions and using DOE.

   (b) To test the following hypothesis: The glide angle can be inferred from i) simulating the parafoil trajectory for flights that have not fully reached steady state, supported by ii) extending the measured trajectory to a steady state via simulations.

   The value of hypothesis 2b, if confirmed, lies in the ability to apply a similar approach to actual quarry flight tests combined with simulations.

1.4 Limitations and Scope of Investigation

The scope of this project is widely dispersed, touching on a few different fields within engineering. They include mechanical and electrical design, aerodynamics, experimentation and theoretical modelling. However, the mechanical and electrical design of the launcher and steering unit respectively is not of main importance in this investigation. Developing an entirely new theoretical model capable of simulating all the aerodynamics of a parafoil system is outside the scope of this project. However, a rudimentary 4-DOF (degree of freedom) theoretical model has been developed to simulate the longitudinal motion of a parafoil-payload system's flight, and has been used to approximate the glide slope of a parafoil. The purpose of the model is to extend unsettled trajectory measurements obtained via experimental flight tests, and to accommodate for atmospheric conditions such as mean wind and turbulence.

Due to the time constraints of the project, it was decided that a relatively small testing matrix be implemented using Design of Experiments for the flight tests and simulations. Therefore, it was decided that the testing matrix only consist of two factors at three levels each. Thus it follows that a 3^2 full factorial design was adequate. The two factors investigated were the trim settings; plumb line length and trim angle. The three levels for the plumb line length were 0.9, 1 and 1.1 times the span of the parafoil, and the three levels for the trim angle were 9, 11 and 13 degrees. In total, nine combinations are possible. In order to estimate the standard deviation of the glide slope, a number of replicate rigging configurations was proposed

to be tested. Replication increases the total number of runs, which in turn increases the experimentation time, and it is for this reason a small testing matrix was implemented.

The experimental flight tests were to be conducted on relatively calm days, meaning that tests could not be run on days where the wind speed exceeded 5 m/s (approximately 10 knots). Although other issues emerged during testing, the investigation focused primarily on inferring the glide angle of the parafoil and the influence trim settings have on glide slope.

1.5 Report Outline

The report begins with a literature review to gain background knowledge on aspects that affect this investigation, such as; aerodynamics and glide performance of parafoils, techniques for launching parafoils, means of determining optimum glide slope and Design of Experiments to name a few. This is followed by a theoretical approach where an algorithm capable of simulating the longitudinal motion of parafoil systems is used to approximate glide slope as a function of the trim settings of the parafoil. It then focuses on the method of the investigation, describing the experimental details and testing procedure. This is followed by the experimental results collected during testing and then the simulated results from the model. A brief discussion explaining these results is also included. Conclusions are then drawn on the basis of these findings and finally, recommendations are made, based on these conclusions.

Chapter 2

Literature Review

2.1 Parafoils and their Performance

2.1.1 Origin of the Parafoil

Early parachutes had a round planform and descended vertically, but with a coning or pendulum oscillation. Accidently when a parachute tore one day, it was realised that the removal of one or two gores at the rear of a parachute stabilised it and resulted in drive [1]. This was essentially the birth of gliding parachutes. Slots or vents were symmetrically cut in the canopy and this stabilised the highly unstable parachute and produced a certain degree of glide. Low glide parachutes have lift-drag ratios of less than 1.5 and the earliest forms of gliding parachutes were simply modified circular canopies. High glide parachutes have lift-drag ratios of greater than 1.5. The Sailwing, the Parawing, the Pioneer Volplane and the most recent and most developed type is the ram air parachute; are all examples of high glide parachutes [1].

The ram-air parachute was invented by Domina Jalbert in the early 1960's and these devices have glide ratios of 3:1 [1, 2]. The high glide ability and controllability allow for the delivery of troops and supplies. Once inflated, a ram-air parachute resembles a low aspect ratio aerofoil or wing and this is essentially how the parafoil got its name. The wing has upper and lower membrane surfaces (double membrane), an aerofoil cross section and a rectangular planform. The leading edge of wing is open over its entire length so that ram air pressure maintains the wing shape [1].

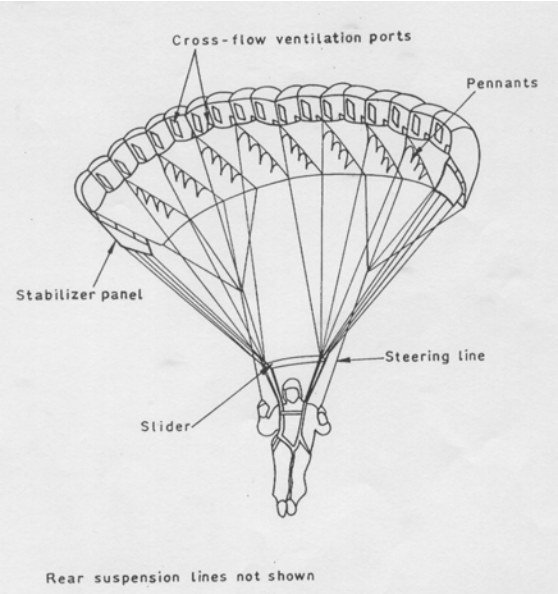

Figure 2.1: The Ram-Air Parachute [1]

2.1.2 General Parafoil Design

A parafoil is essentially a wing manufactured from nonporous fabric and lines. The fabric used is to be as nonporous as possible, because any increase in permeability will cause a reduction in the maximum obtainable lift-drag ratio due to pressure losses [1, 3–5]. In order to support its fold-able characteristics, there are no rigid components and therefore a parafoil can be packed easily [1, 6]. However, this pure and elegant design necessitates in all flight conditions sufficiently high internal pressure to maintain its shape and aerodynamic function. In many design cases, the wing follows a circular (negative dihedral) arc in order to produce the necessary lateral tension and providing directional stability [7]. Essentially there are only three components to consider in the design of a parafoil system. They are the canopy, the lines and the payload; each of which is explained in more detail below.

The canopy has upper and lower membrane surfaces (i.e. double membrane), an aerofoil cross-section, and often a rectangular platform. The aerofoil section is formed by aerofoil shaped ribs sewn chord-wise between the upper and lower membrane surfaces at a number of span wise intervals forming a series of cells [1, 5]. The canopy consists of pennants, stabilizer panels, ribs and cells. Pennants are often triangular in shape pieces of fabric dis-

tributed along the lower surface to which suspension lines are attached. They evenly distribute the aerodynamic load to the suspension lines, thus helping to maintain the lower surface profile. Pennants also partially channel the flow of air into two dimensional patterns, reducing tip loss and aiding in directional stability [5]. The pennants can be seen in Fig. 2.1.

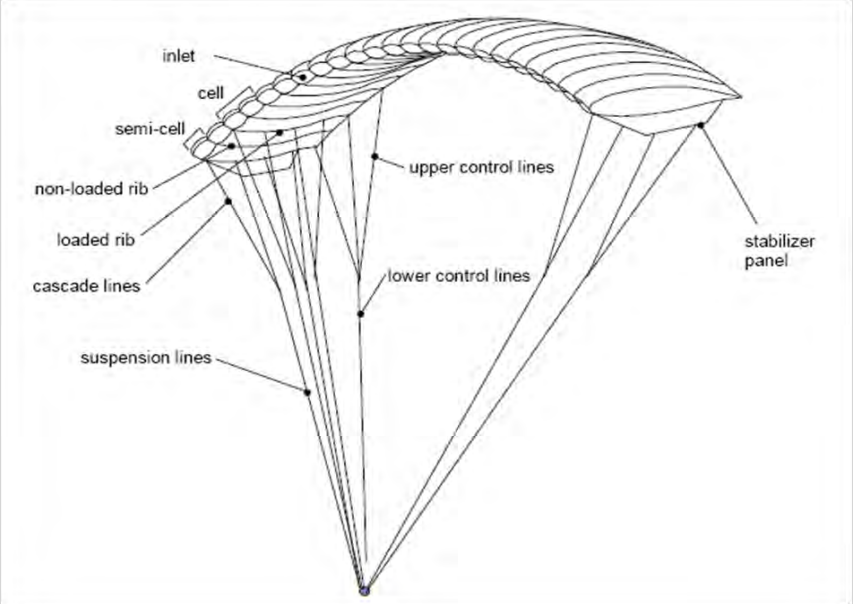

Figure 2.2: The Parafoil and its Components [3]

Stabilizer panels are installed on the ends of the lower surface of the canopy and run from near the leading edge to the trailing edge of the canopy. They act like an end plate on an aircraft wing [8]. Ribs are the sections of fabric installed between the upper and lower surfaces of the canopy that give the canopy its aerofoil shape [8]. There are two types of ribs, load bearing and non load bearing. Cells are the components formed between two load bearing ribs [8]. The suspension lines are attached to the loaded ribs at the line attachment points [5,8]. Cross-port vents are cut in the ribs to allow airflow between cells to ensure even pressurization across the entire canopy [5]. During inflation and pressure equalisation, cells allow the air to flow into the canopy.

Parafoil systems make use of many lines that connect the payload to the parafoil canopy and transfer the weight of the payload to the canopy. The payload can be a human being, or an inanimate assembly of cargo and

navigation equipment. Two types of lines are used, suspension lines and control lines. Suspension lines are generally attached to alternate ribs at multiple chord-wise positions. Suspension lines are necessary to maintain the chord-wise profile of the lower surface of the canopy. These lines are often cascaded to reduce drag [5, 8]. Control lines, also known as steering or brakes lines, are used to steer and adjust the forward speed of the parafoil. Butler [8] gives a more detailed account on the functioning of the control lines but essentially pulling down on one line causes the trailing edge on one side of the canopy to deflect. These lines provide means for lateral-directional and longitudinal control. Turn control is effected by asymmetric pull on the steering lines, and angle of incidence control and flare-out are accomplished by an even pull of the control lines [5]. Figure 2.2 shows a parafoil and its components.

2.1.3 Aerodynamics of Parafoils

Parafoils posses aspects of both aerofoils and parachutes. Whereas parachutes only produce drag, parafoils also generate lift, allowing for useful gliding performance [2]. Sobieski [9] gives a detailed physical account of the aerodynamics of ram-air parachutes. He explains the behaviour of flow over a conventional aerofoil and parafoil canopy, and proceeds to the lift produced with the help of Bernoulli's equation and thus demonstrates how aerodynamic forces act on a parafoil. In a paper by Guglieri [10], he states that the overall behaviour of parachutes is related to various parameters: aerodynamic added masses, filling time, parachute shape (canopy), porosity, suspension line length, reefing, clustering, snatch loads at deployment, and aeromechanical and inflation instability. With all these parameters, it is clear to see why the dynamics of parafoil and payload systems are so complex.

Prakash [5] takes a closer look at the aerodynamic forces acting on a parafoil and payload system. During flight, parafoil and payload systems are acted upon by aerodynamic and gravity forces. The aerodynamic forces are generated due to interaction between the motion of the system and the surrounding atmosphere. The aerodynamic forces are exerted on each and every component, namely; canopy, lines and payload of the system. The lift force is the component of the aerodynamic force normal to the flight path and the parallel component is known as the drag force. These are explained in greater detail below. The force acting vertically downward at the centre of gravity of the system is due to gravity. Figure 2.3 shows all forces acting on a parafoil and payload system.

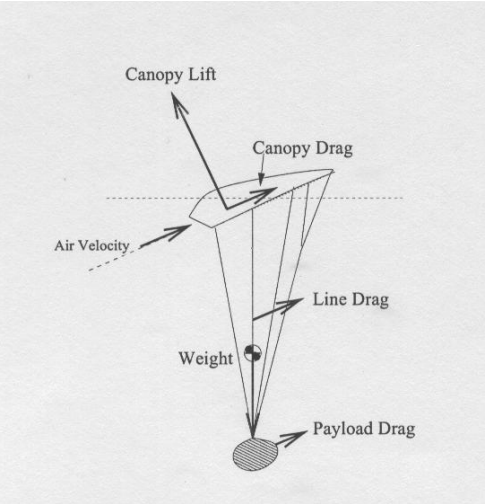

Figure 2.3: Forces Acting on a Parafoil and Payload System [5]

The lift force acts approximately at the quarter chord position of the parafoil canopy in the perpendicular direction of the flight path [2, 3, 5, 11]. The canopy of the parafoil is the source of the lift force because the canopy has an aerofoil shape cross-section. As a result of this, the increased air velocity over the upper surface relative to the air velocity over the lower surface gives rise to circulation, and thus a lift force. The leading edge of the canopy is open to allow for inflation as it moves forward. In order for a system to fly, there must be enough lift force so that one does not only rely on drag to balance the total weight of the system. The lift force is often represented in aerodynamics in its non-dimensional form as the lift coefficient C_L, which is defined as:

$$C_L = \frac{L}{\frac{1}{2}\rho V^2 S} \tag{2.1}$$

Factors affecting lift force generated by a parafoil canopy are the aspect ratio and arc anhedral. Based on lifting line theory, Lingard [3] and Prakash [5] give a more detailed explanation of these factors affecting the lift force. As mentioned before, the drag force is the component of the resultant aerodynamic force in the direction of the flight path. Sources of drag in a parafoil and payload system are the canopy, the lines and the payload. The canopy drag is made up of profile drag and induced drag. Like the lift force, drag force is often represented in aerodynamics in its non-dimensional form as the drag coefficient C_D, which is defined as:

$$C_D = \frac{D}{\frac{1}{2}\rho V^2 S} \tag{2.2}$$

The canopy produces drag force largely due to the nose opening (inlet drag). Pressure drag is due to the integral of the pressure force component over the canopy surface having a non-zero value in the relative wind direction. Skin friction on the upper and lower surface of the canopy results in *skin friction drag*. As mentioned above, profile drag and induced drag make up the total drag experienced by the canopy. Profile drag is due to zero lift drag and induced drag is primarily pressure drag due to trailing edge and tip vortices of the canopy wing. Lingard [3] and Prakash [5] define these types of drag in more detail and provide equations which approximate the magnitude of these drag components.

The drag due to the lines is called line drag. Lingard [3] estimates the contribution of line drag to the total system drag to be:

$$C_{DL} = \frac{nRd}{S} \cos^3 \alpha \tag{2.3}$$

Prakash [5] states that higher aspect ratio leads to large number of lines which in turn results in an increase in the line drag force. Also, as seen by the equation proposed by Lingard above, large line lengths and more lines mean increased line drag. The drag of a parafoil and payload system can be summed up as follows: Normally the highest contribution to total drag is from inlet drag, followed by canopy induced drag and then line drag. Inlet drag makes up nearly a half of the total drag of the system. Induced drag makes up one fourth of the total drag and line drag makes up about 15% of total drag. The payload drag often contributes to only a small amount of the total drag, about 4%, and can be reduced even further by using streamlined containers.

The lift to drag ratio is a measure of aerodynamic efficiency of the parafoil and payload system. It is the ratio of lift produced by a parafoil canopy and payload to the total drag produced by all the components of a parafoil and payload system [5]. The higher the lift to drag ratio of a parafoil and payload system, the further the distance covered by the gliding system. Prakash [5] briefly explores the effects on the gliding performance of the system, caused by the components of the parafoil and payload system, the aspect ratio and the line length. In Fig. 2.4, Prakash shows the typical lift to drag ratio breakdown as a function of angle of attack. Note, as to be expected, that the lift to drag ratio is reduced by the addition of a payload and lines. He also shows that increasing aspect ratio increases the aerodynamic performance of the gliding system. Prakash states that there is an optimum value of line

length for a given aspect ratio which results in the best performance of the gliding system [5].

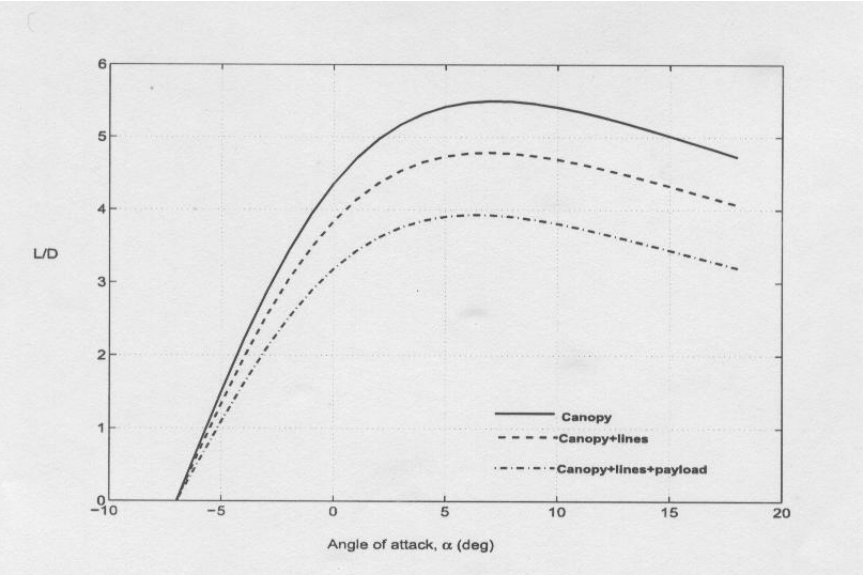

Figure 2.4: Effect of Components of a Parafoil System on L/D Ratio [5]

2.1.4 Glide Slope and Trim Settings

The angle formed between the glide path of the payload and the horizon in still air is called the *glide slope angle* [5, 8]. The standard equation of aerodynamic efficiency in gliding flight is given by:

$$\frac{C_L}{C_D} = \frac{L}{D} = \frac{1}{\tan\gamma} \tag{2.4}$$

The glide angle can thus be rewritten as:

$$\gamma = \tan^{-1}\frac{D}{L} = \tan^{-1}\frac{C_D}{C_L} \tag{2.5}$$

Lift and drag coefficients for parafoils of various aspect ratios can be found in the paper by Nicolaides and Tragarz [6]. Matos et al [12] tested a 2.5 aspect ratio parafoil and concluded that the L/D ratio (glide slope) was 3.1, this is essentially a glide angle of 17.9°. From Equation 2.5, the higher the lift-drag ratio, the smaller the glide angle becomes and the greater the gliding range for a given height loss, thus the greater the aerodynamic efficiency. In a paper by Brown [13], he cleverly fixes the glide angle during testing of the performance

of full scale parafoils, and measures the airspeed in order to determine the parafoil's L/D ratio and lift coefficient. Some use of trigonometry in his testing technique enables him to replace the glide angle with what he calls the *tether angle* so that Equation 2.4 can be implemented in his calculations.

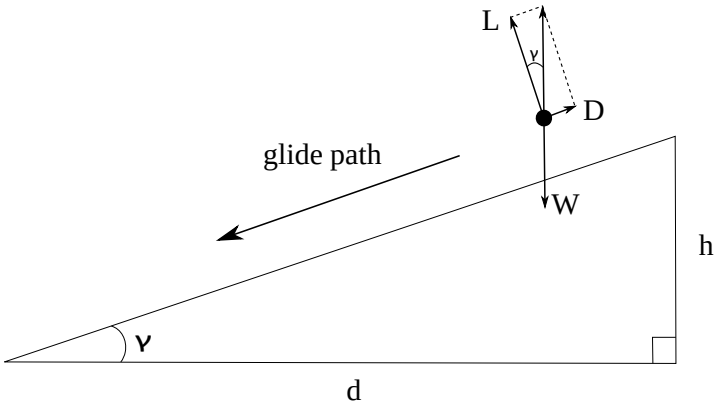

Figure 2.5: Schematic of Glide Slope Angle

In more general terms, the glide slope is just the ratio of the vertical distance to the horizontal distance travelled or h/d. Therefore, the glide angle can also be calculated by:

$$\gamma = \tan^{-1} \frac{h}{d} \tag{2.6}$$

Theoretically, Equations 2.5 and 2.6 should produce the same result because the lift force acts perpendicularly to the glide path, and the drag force acts parallel to the glide path but in the opposite direction. Figure 2.5 shows this simple bit of trigonometry.

It is desirable for a parafoil system to have the ability to adjust its flight path angle as it approaches the target. Therefore, glide slope control is generally required. Rotation of the parafoil's canopy will cause changes to the canopy lift and drag vectors resulting in changes in the equilibrium glide slope [14]. Ward [15] investigates the glide slope control for a parafoil and payload aircraft. In his thesis, he concludes that large changes in glide slope can be achieved by using coupled incidence angle variation and trailing edge brake deflections. He also concluded that flight tests using autonomous landing with glide slope control mechanism demonstrated an improvement in landing accuracy by a factor of 2 or more especially in windy conditions [15].

Figure 2.6 illustrates glide ratio versus aspect ratio for a variety of parafoil canopies of parafoil-payload systems in use today. There are two distinct groups in this plot compiled by Ward, the lower aspect ratio/lower glide ratio group is composed of airdrop systems, and the higher aspect ratio/higher glide ratio group is composed of paragliding canopies designed for soaring flight. The work done by Ward focuses on canopies at the higher end of the spectrum of air-drop systems [15].

This current project focuses on determining the glide slope of a parafoil with an aspect ratio of about 2.6.

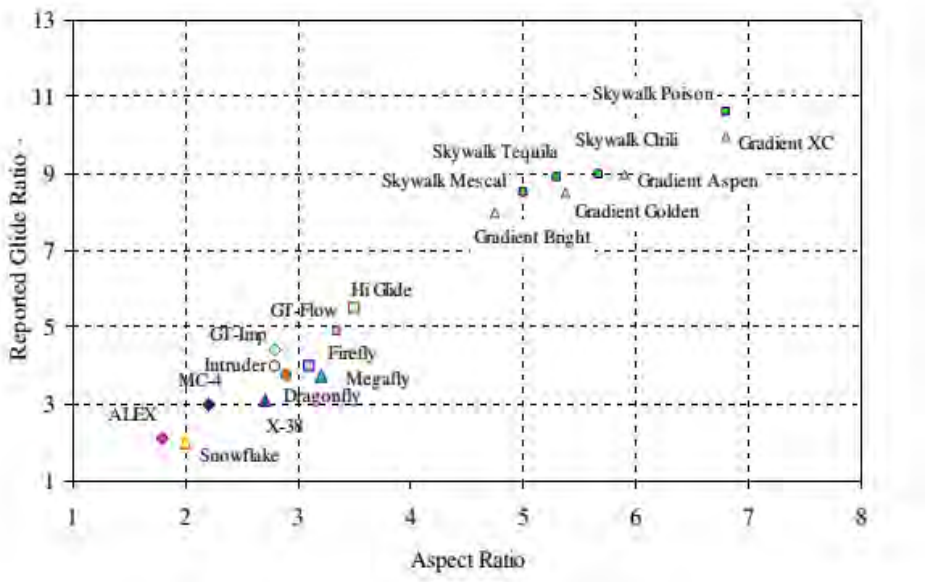

Figure 2.6: Reported Glide Ratio vs. Aspect Ratio for Several Parafoil Systems [15]

It is obvious that the glide slope angle depends on the lift-drag ratio and can be manipulated mid-flight with symmetric flap deflections. However, changes in only flap setting increase the lift coefficient as well as drag, resulting in only a slight decrease in lift-drag ratio [2]. In a paper by Gavrilovski et al [16], a novel approach of integrating aerodynamic spoilers into the canopy in order to generate glide slope control is explored. Both an upper surface slit-spoiler and a lower surface flap-spoiler were investigated. It was shown that significant glide slope control can be achieved with either device. Previous research has shown that improved landing accuracy of autonomous parafoils can be achieved using glide slope control generated by dynamic modification of the canopy incidence angle. An example of such work is shown in the

paper by Slegers et al [17] and the flight test results for parafoil canopies of various aspect ratios are summarised in the paper by Ward et al [18].

In order to better understand trim settings (which directly affect the glide performance) of a parafoil, the definitions of trim angle and trim line are important. *Trim line* is defined as the straight line formed using the furthest forward and furthest aft suspension line attachment points as endpoints, whereas *chord line* is the straight line joining the leading and trailing edges. The trailing edge may be used as the aft reference point only if it is not used as a control surface or deployment aid. The *plumb line* is the straight line from the quarter chord point to the confluence point [8]. The complementary angle to the angle formed formed by the trim line and the plumb line is called the *trim angle* (μ). This is illustrated in Figs. 2.7 and 2.8. It should be noted that the trim angle is not the same as the tether angle mentioned earlier. Referring to Fig. 2.7, the tether angle is denoted by θ. Also, in Fig. 2.8, Butler [8] uses tau (τ) to denote the trim angle. Both these figures are for trimmed flight.

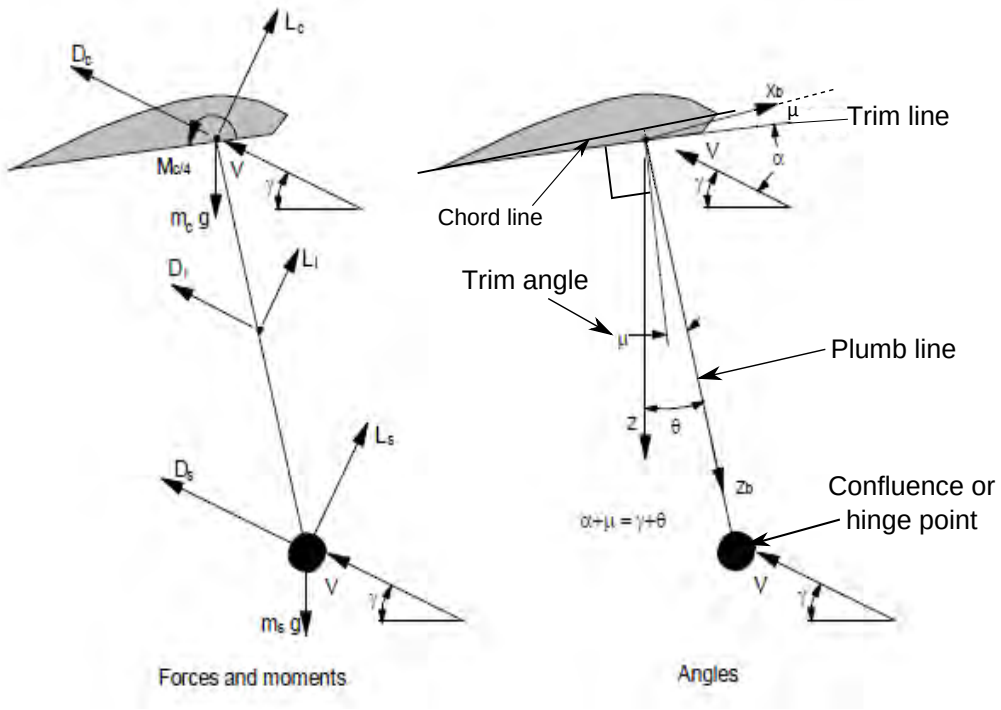

Figure 2.7: Parafoil System in Steady Trimmed Flight Adapted from Lingard [3]

The reference line, as depicted in Fig. 2.8, passes through the quarter chord point perpendicular to the plumb line [8]. Trim angle is positive when the trim line is nose up relative to the reference line, as illustrated in Fig. 2.8. However, in Fig. 2.7, trim angle is negative because the trim line is nose down relative to the reference line. The reference line will be horizontal during steady glide only if $C_{m,c/4} = 0$. Otherwise, the confluence point is to be moved forward or backwards to sustain the same canopy orientation relative to earth. This has an influence on control forces. $C_{m,c/4} > 0$ is desired. Refer to Fig. 2.8.

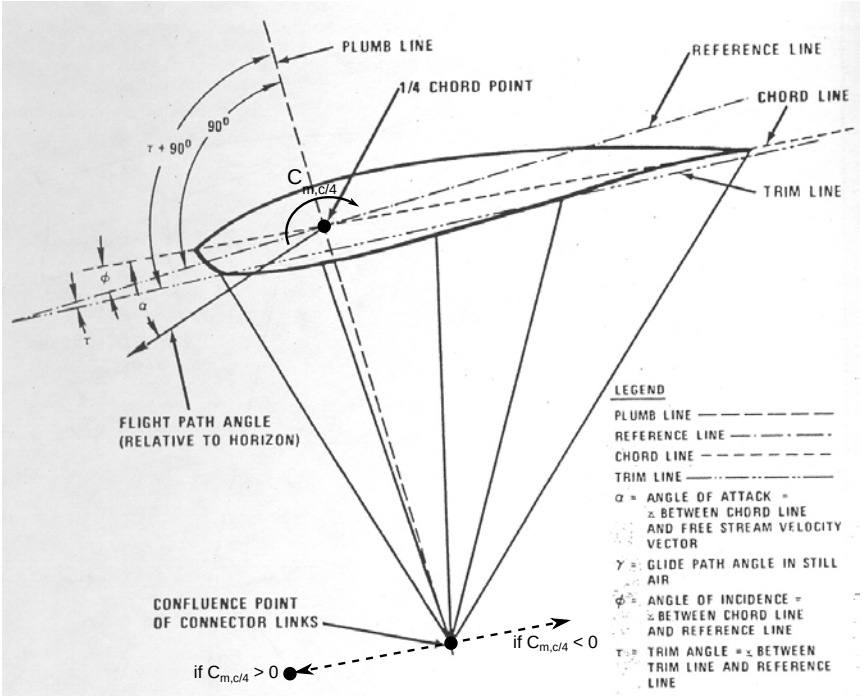

Figure 2.8: Reference System for Parafoils Adapted from Butler [8]

The trim setting of the parafoil used in this project is essentially adjusted by changing the trim angle and varying the relative suspension line lengths. This alters the position of the confluence or hinge point. Therefore, for a certain trim angle setting, the plumb line length can be increased or decreased, and the effect on glide slope for a specific configuration can be investigated. Increasing the line length though is destabilizing and great care must be taken when rigging a parafoil [3, 19]. Slegers and Costello [20] used a non-linear 9 degree of freedom simulation model to show that canopy tilt provides a powerful lateral control mechanism and rigging angle provides a

viable longitudinal control mechanism. Therefore, by the same notion, trim angle can provide a similarly viable longitudinal control mechanism because rigging angle and trim angle are closely related. Rigging angle is the angle between the parafoil's reference line and the chord line [8, 21], and is essentially the angle of incidence [8, 20], denoted by ϕ in Fig. 2.8 and 2.9.

In fact, the relationship between rigging angle (or angle of incidence) and trim angle is illustrated in Fig. 2.9. Using Butler's [8] convention, with the exception that μ denotes trim angle and not τ, it follows from Fig. 2.9 that $\mu = \phi + \beta$. It should be noted that μ and ϕ have negative values in this figure because trim line and chord line are nose down with respect to the reference line. Here beta (β) is the angle between the trim line and chord line. For a given parafoil canopy, the trim line and chord line does not change, therefore the angle β is a constant. Thus, sometimes in literature, rigging angle and trim angle can mean the same thing. The smaller the rigging angle, the greater the angle of attack, which in turn means a greater glide slope. However, smaller rigging angles result in a greater chance that the parafoil will stall and collapse. Typically the rigging angle is between 5 and 15 degrees [21].

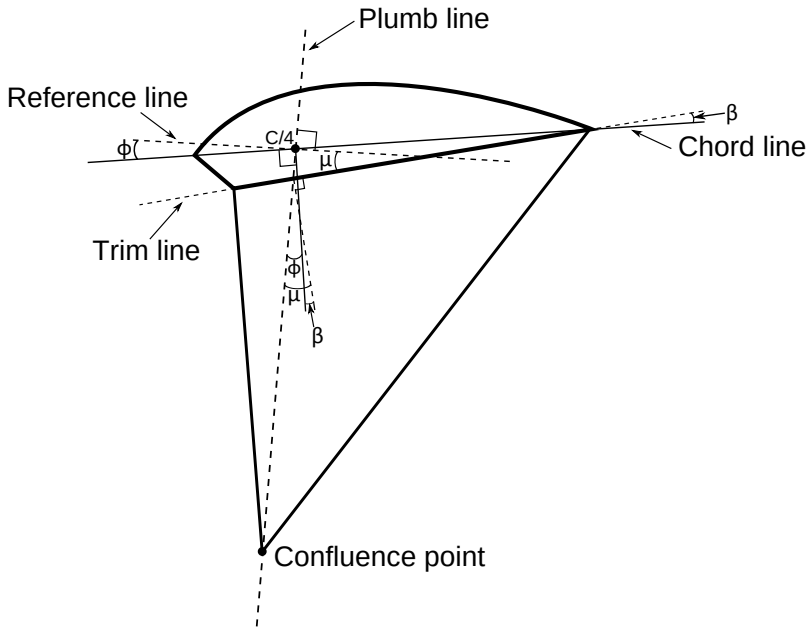

Figure 2.9: Relationship between Rigging Angle and Trim Angle

In the work done by Ward [15], he states that the effect of changing the incidence angle on a parafoil and payload system is very similar to the effect

of the elevator on a fixed wing aircraft in glide. "Just as the elevator alters the trim angle of attack of the wing, altering the incidence angle produces a change in the trim angle of attack of the parafoil canopy. Assuming that the pitch angle of the system is constant (location of the centre of pressure of the canopy is constant), the sum of the incidence angle and the angle of attack will be the flight path angle." Thus, there is a unique lift to drag ratio (glide slope) versus angle of attack curve determined by the aerodynamic characteristics of a given canopy. The intersection of the flight path angle curve for a given incidence angle setting and the glide slope curve for a given canopy represents the trimmed flight condition for that combination of incidence angle and canopy. This concept proposed by Ward is shown in Fig. 2.10 for two notional canopies [15]. For example, for an incidence angle of $-10°$ and a "low glide ratio canopy", the trimmed angle of attack is approximately 12° and the glide slope is approximately 2.4.

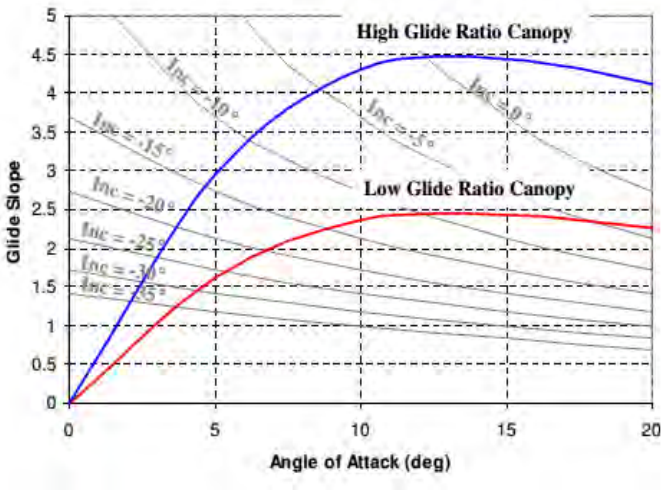

Figure 2.10: Conceptual Plot of Canopy Trim Conditions [15]

The parafoil system consists of mainly three components; the parafoil canopy, the lines and the payload, which all contribute to the stability (a concept eluded to before) of the entire system. The lines and canopy are considered unstable contributions, while the payload is stable [5]. Stability of a parafoil system, like an aircraft, is defined as the parafoil system's ability to sustain a specific, prescribed flight condition. Equilibrium and stability are closely related. A parafoil system is said to be in equilibrium, in a specific flight condition, when the sum of the forces and moments acting on the system is zero. It is important to distinguish between static and dynamic stability. Static stability describes the tendency of a parafoil system to retain its original orientation when subjected to any disturbances. Dynamic

stability describes the oscillatory motion of a statically stable system when it tries to retain its original position [22].

If the restoring aerodynamic moment opposes the disturbance angle of attack, and the system achieves its original attitude, the system is said to be statically stable. Lingard [1, 3] provides more information on ram-air parachute longitudinal static stability. Lindgard states that: "The parachute will be in stable equilibrium when the sum of moments acting on the system is zero and when the slope of the pitching moment curve, $dC_m/d\alpha$, is negative – that is when any small disturbance from equilibrium results in a restoring couple" [1, 3]. After experiencing a disturbance, a parafoil system is dynamically stable when it attempts to retain its attitude by reaching the equilibrium position through a series of decaying oscillations.

Müller [23] provides a more detailed explanation of lateral and longitudinal dynamic stability. In particular, Müller investigates the influence of certain factors on the longitudinal and lateral-directional modes. These factors include: the position of the coupling or hinge point, the nominal line length, the nominal distance of the payload's CG, and the control inputs (brake deflection settings). The longitudinal modes for a parafoil system, like an aircraft, are the short period and phugoid (long period). There is a third longitudinal motion mode that is unique to a parafoil system, and is investigated by Müller, it is known as the pendulum oscillations [23]. In addition, there are three types of possible lateral-directional dynamic motion, namely: spiral mode, roll subsidence mode, and Dutch roll mode.

In a paper by Iosilevskii [24], it was shown that the most forward CG position of a gliding parachute is limited by a loss in longitudinal stability and by a loss of control power, whereas the most rear CG position is limited by a requirement of stall-free controls range. Redelinghuys and Rhodes [25] draw similar conclusions in their study, in agreement with Iosilevskii [24]. Since parafoil and payload systems have fundamental non-linearities in their performance characteristics due to canopy aerodynamics and large vertical offset between the aerodynamic centre and the over-all centre of gravity of the system, bifurcation methods are convenient for numerical computation of trim and stability characteristics of the parafoil and payload systems with nonlinearity [26]. Bifurcation analysis requires the parafoil and payload system to be represented by a mathematical model consisting of a set of autonomous first-order ordinary differential equations. Bifurcation theory is used to study the solutions of parafoil system differential equations by varying one design parameter at a time while keeping all other parameters fixed [26].

2.1.5 Parafoil Modelling

The simplest and often taken approach in literature to modelling parafoil-payload aircraft is to assume the entire system is a rigid body, and to decouple the longitudinal and lateral dynamics to obtain a reduced order model. One use of these simplified models is to obtain insight into particular aspects of parafoil flight dynamics [15]. Figure 2.11 illustrates a simple six degree of freedom (6-DOF) parafoil system where the parafoil and payload are considered as one rigid body. The combined system of the parafoil canopy and the payload are often modelled with 6-DOF, including three inertial positions as well as the three Euler orientation angles [27]. Ward [15] and Tweedle [21] explore the details of the modelling and simulation for a six degree of freedom system. The three aerodynamic moments (rolling, pitching, yawing) are illustrated by L, M and N respectively. The accompanying roll, pitch and yaw rates are indicated by p, q and r. The three aerodynamic forces are the thrust force (X), side force (Y) and vertical force (Z). The lift and drag forces depicted in Fig. 2.3 contribute to the X and Z force components.

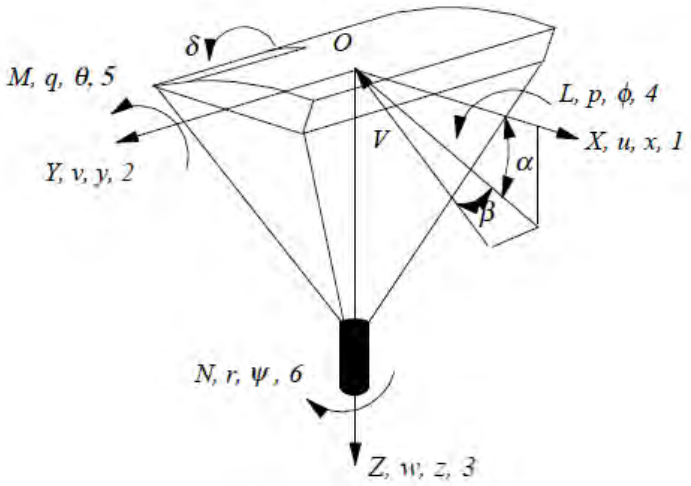

Figure 2.11: A 6-DOF Parafoil System [3]

In one of the first modelling efforts, Goodrick [28] used only a 3-DOF model to analyse both static and dynamic longitudinal stability of high performance gliding airdrop systems (parafoils). Iosilevskii [24] also used a 3-DOF longitudinal model to study the effect of forward and backwards shifting of the payload centre of gravity. More recently, Gorman and Slegers [29] investigated a 7-DOF model, where they were only interested in the relative yawing motion of a payload with respect to a parafoil. They concluded that a 7-DOF model was adequate to capture the most significant navigation features of the relative motion between the parafoil and payload [15, 29]. This

conclusion, however, depends on the number of relative degrees of freedom between canopy and payload permitted by the rigging.

Often for modelling and experimentation purposes, higher degree of freedom models are developed, such as an 8-DOF model, six for the air vehicle and two relative rotations for the parafoil [30]. Parafoil and payload relative motion is important because, although the most significant loads come from the canopy, the payload is normally where sensors are located [14]. Redelinghuys [31] has developed an 8-DOF model using analytical dynamics, where aerodynamic moments and forces acting on the parafoil system can be computed using coefficients which depend on the canopy (dimension, shape of the profile, etc.). Yakimenko [32] also investigates the developments of a scalable 8-DOF model for a generic parafoil-payload delivery system. Doherr and Schilling [33], Slegers and Costello [34], and Prakash and Ananthkrishnan [35] all analyse 9-DOF models, that capture the relative rotations in all three axes between the canopy and payload, in their respective studies. Toglia and Vendittelli [30] also investigated "a 9-DOF model based on Newton-Euler approach, useful for parafoil certification tests, and a 6-DOF model used for planning and control design." Wolf [19] went as far as using a 10-DOF model, five degrees of freedom for each body, with roll about axis symmetry being neglected, however this was for a non-rigid parachute and payload system.

Wind Model

To accurately model and simulate aircraft systems, and more specifically parafoil-payload systems, models are necessary to characterise environmental aspects. In particular, wind can have damaging effects to the landing accuracy of parafoil systems, and thus models are needed to accurately represent the wind profile. For the purpose of this investigation, only low-altitude models are considered. There are numerous ways of creating a mean wind velocity profile that can be implemented in a simulation investigating the gliding decent of a parafoil. Etkin [36] states that "the wind may have a mean structure which is not uniform in space, that is, there can be *spatial* gradients in the *time-averaged* velocity." The region of most concern is the boundary layer next to the ground produced by the wind blowing over it. Hence, Etkin proposed modelling mean wind variation based on power law profiles, where the mean wind is a function of: the height above the ground, the roughness of the underlying surface, and the speed and height outside the friction layer [36].

The power law, the first representation of the mean wind profile in horizontally homogeneous terrain, was proposed in as early as 1916 [37]. The general form of the power law is as follows:

$$U(z_{g1}) = U(z_{g2}) \left(\frac{z_{g1}}{z_{g2}} \right)^{\alpha} \tag{2.7}$$

where α is an exponent dependent on ground roughness, z_{g1} and z_{g2} denote heights above ground, and U denotes mean wind speed. According to Simiu and Scanlan [37], the logarithmic law or log wind profile is regarded by meteorologists as a superior representation of strong wing profiles in the lower atmosphere as compared to the power law. The logarithmic wind profile equation may be expressed as:

$$U(z) = \frac{u*}{k} \ln \left(\frac{z}{z_0} \right) \tag{2.8}$$

where U is the mean wind speed at the height z, $u*$ is the friction velocity, k is the von Karman's constant ($\simeq 0.40$) and z_0 is the roughness length. The roughness length is a measure of the eddy size at the ground [37, 38].

On occasions where the surface roughness may not be known, the power law and the logarithmic law cannot be used to simulate the mean wind profile. Therefore, military specifications [39, 40] propose a profile derived from a known wind velocity at 20 feet above the ground to find the magnitude of the wind scalar shear velocity as a function of altitude (h) only.

$$u_w = u_{20} \frac{\ln \left(\frac{h}{z_0} \right)}{\ln \left(\frac{20}{z_0} \right)} \tag{2.9}$$

With $z_0 = 0.15$ feet. Due to the fact that the military specifications are American, all values expressed in feet must be converted to metres. Often when modelling the mean wind profile, the wind velocity at 20 feet may not actually be known, therefore a wind of stochastic nature is assumed to be known. Thus, this can result in a tailwind or headwind, depending on the non-repeating random number generated from a Gaussian distribution. With respect to parafoil-payload systems, there is a significant difference in altitude between the canopy and the payload during flight. Therefore, it is also assumed that the mean wind is frozen in space, meaning that the mean wind encountered by the canopy and payload will be the same, regardless of this difference in altitude. In addition, the mean wind does not depend on

time and is thus deemed a stationary process [41]. Figure 2.12 compares the four mean wind profiles discussed above in a study done by fellow student Donal Phair.

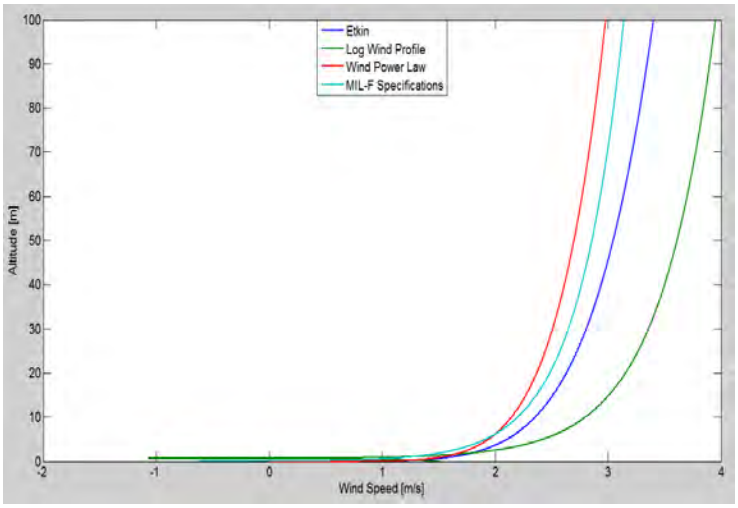

Figure 2.12: Comparison of Mean Wind Profiles Based on a 3 m/s Known Headwind [41]

Turbulence Model

In addition to mean wind, turbulence also needs to be considered when regarding the glide performance of a parafoil-payload system. Again, only low-altitude turbulence models are considered, because like mean wind, the region of most concern is the turbulent gusts in the boundary layer. A low-altitude model is defined as altitude less than or equal to 1000 feet (304.8 metres) [42]. Modelling turbulence through explicit functions of time and space is impossible, because turbulence is very much a random process. Therefore, only a statistical, probabilistic approach can be implemented [41]. Atmospheric turbulence is pretty well documented by Etkin [36] and he notes some fundamental assumptions required for accurate models. Like mean wind, turbulence is treated as *frozen* and *stationary*. Despite some contention amongst researchers that atmospheric turbulence is not necessarily *normal*, or *Gaussian*, many researchers have concluded that it may be modelled so for practical purposes in many situations. Another assumption widely employed is that turbulence is *homogeneous* along the flight path. Thus, with respect to horizontal translations, turbulence is assumed to be contained within one large homogeneous patch. Finally, Etkin mentions that at high altitudes the turbulence is *isotropic*, meaning that all the statistical properties at a point are independent of the orientation of the axes [36].

Beal [43] discusses the application of random turbulence to an aircraft simulation in an attempt to predict the response of an aircraft to the turbulence. The turbulence models most frequently used are the Dryden and von Kármán models. The power spectra for these models are defined analytically in MIL-F-8785C [40] and MIL-HDBK-1797 [39]. Yeager [44] presents three methods of implementing the Dryden power spectral density model for atmospheric turbulence. The three methods include: continuous, Tustin transform and Military Standard algorithms. The continuous model requires solving differential equations describing the Dryden turbulence model, while the Tustin and Military Standard implement recursive difference equations to compute components of turbulence [44]. The Dryden and von Kármán models are also well documented in a paper by Gage [42].

Low altitude models are defined by three values: turbulence scale length, turbulence intensity and turbulence axes orientation [42]. According to the military specification MIL-F-8785C [40], the turbulence scale lengths at low altitudes are defined as follows:

$$L_w = h \tag{2.10}$$

$$L_u = \frac{h}{(0.177 + 0.000823h)^{1.2}} \tag{2.11}$$

The turbulence intensities are given in the following equations:

$$\sigma_w = 0.1u_{20} \tag{2.12}$$

$$\frac{\sigma_u}{\sigma_w} = \frac{1}{(0.177 + 0.000823h)^{0.4}} \tag{2.13}$$

Typical wind speeds at 20 feet are dependent on the turbulence level [39, 40].

Table 2.1: Typical Wind Speeds at 20 feet [42]

Turbulence Level	u_{20}
Light	15 knots ($\simeq 7.7\ m/s$)
Moderate	30 knots ($\simeq 15.4\ m/s$)
Severe	45 knots ($\simeq 23.15\ m/s$)

The turbulence axes orientation in the low altitude region is defined as follows:

- Longitudinal turbulence velocity, u_g, along the horizontal relative mean wind vector, and
- Vertical turbulence velocity, w_g, aligned with the vertical [42].

The turbulent wind gust velocities in the vertical and headwind inertial axes can be calculated through application of the discrete Dryden turbulence spectrum difference equations derived from power spectral density functions [39–44]:

$$u_g(k) = \left(1 - \frac{V}{L_u}T\right) u_g(k-1) + \sqrt{2\frac{V}{L_u}T}\sigma_u\eta_1 \tag{2.14}$$

$$w_g(k) = \left(1 - \frac{V}{L_w}T\right) w_g(k-1) + \sqrt{2\frac{V}{L_w}T}\sigma_w\eta_2 \tag{2.15}$$

Where T is the sampling time, V is the airspeed and η represents the Gaussian noise forcing functions. In the MATLAB/Simulink environment, this is realised by implementing a non-repeating Gaussian white noise source [41]. The equivalent differential equations mentioned by Yeager [44] for the continuous implementation of the Dryden turbulence model take the following form:

$$\dot{u_g} = -\frac{V}{L_u}u_g + \sigma_u\sqrt{\frac{2V}{TL_u}}\eta \tag{2.16}$$

2.1.6 Applications of Autonomous Parafoil Systems

Parafoils are highly controllable when compared with conventional parachutes. Apart from skydiving and paragliding, parafoils have gained widespread use and importance in accurate aerial delivery to remote areas where aircraft cannot land. With the aid of automatic on-board guidance, parafoils have the potential for more precise landing than with conventional circular parachutes. The need for autonomous parafoil and payload systems is quite widespread. The main reasons to develop autonomous parafoil and payload delivery systems include the following:

1. The delivery of the payload without endangering life or property.
2. To develop a parachute with glide and control characteristics that can compensate inaccuracies in drop point and wind, and therefore not get lost [5].
3. And finally, to achieve a low vertical and horizontal velocity at landing, in order to minimize the potential damage to the payload.

Parafoils could be used in the recovery of unmanned aerial vehicles (UAV's) and crew return vehicles (CRV's). In a paper by Stein et al [45], an example of this application is shown. He states that the purpose of NASA's X-38 program was to develop a 25,000 lb (11,340 kg) CRV for re-entry from Earth's orbit, and it needed to be capable of reducing the landing speed from 250 knots (463 km/h) to 40 knots (74 km/h), thus an autonomously or manually steered parafoil capable of performing a dynamic flare was implemented.

Autonomous parafoil systems can be used to accurately air-drop cargo under adverse weather conditions and at large stand-off distances [46]. This can be achieved by precise trajectory control through the use of a radio-controlled homing parafoil capable of steering. Toohey [2] gives a detailed explanation of a couple of methods associated with trajectory guidance and control. The cargo in air-drops can be anything and usually includes food, medicine and equipment. A parafoil can be implemented in the recovery of sounding rockets used to investigate Earth's upper atmosphere. Yatoh et al [47] explore the navigation, guidance and control of a parafoil recovery system for an experimental rocket. The deployable parafoil is used as a landing system during the final stages of re-entry [45–48]. The sequence of events for the rocket payload recovery, as demonstrated in an experiment by Hiraki and Inoue [49] is as follows: The deployment of a pilot chute to initially slow down the rocket, the pilot chute deploys the parafoil, and then the parafoil inflates bringing the rocket safely to the ground. Parafoil systems may also be used for a vast variety of military operations, such as: the delivery of troops and ammunition, the recovery of troops and equipment, and the terminal guidance of shells, rockets and re-entry bodies [5, 50].

Figure 2.13: Cargo being Air-Dropped
Source: http://www.airplane-pictures.net

Figure 2.14: NASA's X-38 Program

2.2 Parafoil Launching Techniques

There are numerous ways one could get parafoil-payload systems, glider systems, delivery systems or UAV's into the sky. The most obvious way being air-drops; where these systems are dropped from fixed-wing aircraft or rotary-wing aircraft. The Guided Parafoil Delivery System (GPADS), the Semi Rigid Deployable Wing (SRDW) and the Extended Range Aerial Delivery System (ERADS) are all examples of air-dropped delivery systems [51]. The GPADS uses an avionics package hung underneath a parafoil to deliver its cargo from a high altitude air-drop, while the SRDW and ERADS are air-dropped inflatable wings [51].

Figure 2.15: Guided Parafoil Delivery System [51]

In a paper by Milgram et al [52] in 2003, they explore Advanced Logistics Delivery Systems (ALDS) and more specifically two autonomous glider systems for logistics delivery; a sea-based, catapult-launched glider, and an air-dropped glider with inflatable wings. In 2004, Hope and Kennell [51] study the latter, the aerodynamic design of a flying wing ALDS glider utilizing inflatable wing technology. They also investigate alternate delivery systems, but claim that at the time the ALDS remained the only logistics vehicle capable of being shipboard catapult-launched; providing a great asset to the Navy [51].

Shipboard catapults, however, have been used quite regularly to launch UAV's since then. In a report by Doyle [53], it was assumed that a catapult launching system would be used as the method of launching a UAV from a patrol boat. In the end, Doyle implemented a bungee cord launching device developed by Jack Francis [53]. Refer to Fig. 2.16. Shipboard catapults are not the only way ships can be utilised to launch aerial delivery systems. Ship Launched Aerial Delivery System (SLADS) is a concept in which cargo can be transferred from ship to shore using a parafoil-payload system. It is accomplished in two phases: An initial towing phase when the glider follows the towing vessel in a passive lift mode and an autonomous gliding phase when the system is guided to the desired point [54].

Figure 2.16: Bungee Cord Launching Device [53]

While many previous researchers have analysed the parafoil-payload system when it is released from another airborne vehicle, limited work has been done in the area of towing up the system from ground or sea [54]. Snowgoose, developed by the MMIST Company (Mist Mobility Integrated Systems Technology, Inc.), is a powered parafoil that is ground launched from the back of a pickup truck or high mobility multi-purpose wheeled vehicle (HMMWV) with a 35 mph (56.3 kph) head wind required for launch [51, 55]. See Fig. 2.17. This technique is similar to the initial deployment and inflation of a parafoil's canopy using a truck's acceleration presented by Brown [13].

Figure 2.17: Launch of the Snowgoose Powered Parafoil [55]

Rockets can also be used to launch parafoil-payload systems, glider systems, delivery systems or UAV's into the sky. In turn, parafoils can be used

for the recovery system of rockets. Yatoh et al [47] investigate a parafoil recovery system where it is deployed at the apogee of the trajectory and guides the rocket to a landing point, Fig. 2.18. In a paper by DeTurris et al [56], a 4 ft (1.2 m) tall rocket was designed and built to carry a 6 ft (1.8 m) wingspan parafoil and electronics package. Flight tests proved the launch system could successfully deploy the parafoil and activate the autonomous flight controller, however, there were problems encountered during the deploy event. Parafoil lines were often getting tangled or broken during deployment, resulting in an uncontrollable descent due to the fact that the delay charge was too long and deployment occurred 3-4 seconds late [56].

Hiraki and Inoue [49] also investigated the controlled recovery of a small rocket using a parafoil. During the test using a small rocket before deploying the parafoil system, the autonomous parafoil system missed its intended target by 1.7 km. This unsatisfactory result was caused by the change of the electromagnetic circumstances due to the malfunction of the wireless transmitter. A logical explanation for this provided by the authors was that during the combustion of the rocket, vibrations caused the transmitter to be turned off during flight and the servomotor that manipulates the control lines of the parafoil negatively affected [49]. This negative result, in conjunction with the work done by DeTurris et al [56], further illustrates some of the problems with launching parafoil-payload systems with rockets. Hiraki and Inoue also conducted an automatic flight test of a palm-top system from a helium-filled balloon, an air-drop, that had a much better result and only missed its intended target by 32 metres [49].

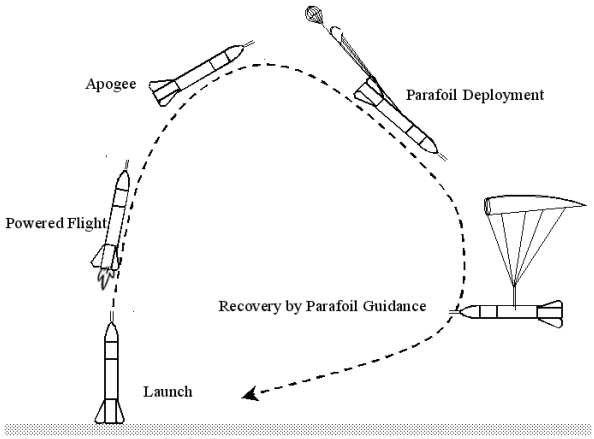

Figure 2.18: Parafoil Recovery System [47]

Another unique way of a launching parafoil-payload system was invented by Harold J. Liberman. In his patent entitled "Cannon Launched Reconnaissance Vehicle" [57], he describes a relatively inexpensive way to position an unmanned reconnaissance payload over a potential target area, using a cargo projectile launched from a conventional tubed artillery piece (cannon), under all weather and environmental conditions. The use of tow line between the ejected reconnaissance payload and the ballistic cargo projectile allow the payload with its parafoil to achieve a greater height, enter an orbit and extend a longer time over the target area [57]. Refer to Fig. 2.19.

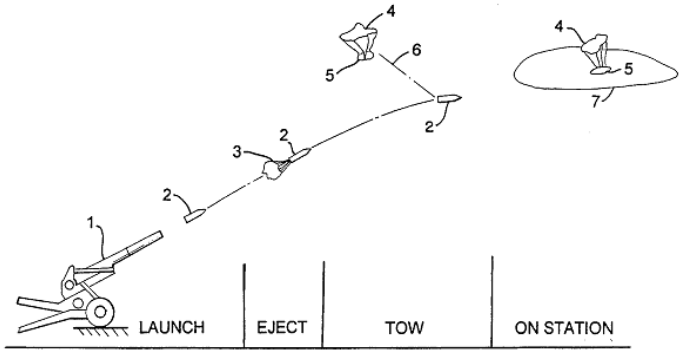

Figure 2.19: Cannon Launched Parafoil-Payload System [57]

UCT's Parafoil Launcher

A unique catapult that was originally designed by William Norton (during his studies at the University of Cape Town) for launching parafoils from a hilltop has undergone considerable modification over the past two years. Figure 2.20 shows a time lapse of William Norton's original parafoil launcher in action. Professor Christiaan Redelinghuys, Steven Rhodes, Jordan Adams and Tracy Booysen (all from the University of Cape Town) have invested considerable resources to refine William Nortons original parafoil launcher in efforts to better launch parafoils. With huge success, the University of Cape Town now have a parafoil launcher system capable of repeatedly launching parafoil systems of about 30 kg at a launch speed of 15 m/s. The essential components of the parafoil launcher system are: the trailer, the linear track, the arm structure, the linear accelerator, the carriage and the steering unit enclosure. Refer to Fig. 2.21. These components will be explained in a little more detail below, but as this is outside the scope of this investigation, consult Grunwald et al [58] for a more thorough explanation of the functioning of the parafoil launcher.

The working principle that the launcher relies on, is based on two distinct mechanisms that are activated sequentially: First, an arm performs a swing action to inflate the parafoil's canopy. As soon as the canopy is fully inflated, a linear launcher is triggered to accelerate the payload. The energy source for the launcher is a set of springs.

Figure 2.20: A Time Lapse of William Norton's Original Parafoil Launcher

The trailer of the parafoil launcher is about 6 metres in length and the linear accelerator and rotational arm structure is rigidly mounted to it. The trailer has four adjustable support legs, two at the front and two at the back, which support the trailer during launching and allows for adjustment of the launching angle. The trailer also supports a linear track for which the carriage containing the steering unit enclosure will run along.

The arm structure is bolted to the trailer and a winch tensions the springs. A release system, comprising of a release cord and a release shackle is connected to the arm and carriage respectively. Launch is effected by manually triggering the arm and as the arm swings over to a certain position before top dead centre, the release cord on the arm releases the shackle on the carriage, and the linear accelerator accelerates the carriage containing the steering unit along the track. In the released state, it is important that the springs still have a certain degree of pre-tension so that they can stop the recoil motion gradually after release and prevent the springs from *'thrashing'*. For more information on the method of pre-tensioning the springs consult Grunwald et al [58].

The linear accelerator comprises of a pulley and spring system. The po-

tential energy stored in this system is converted to kinetic energy accelerating the carriage along the linear track at the required velocity for launch. The pulley and spring system has been cleverly designed to give the accelerator a *'mechanical advantage'* and by energising these two mechanisms with one winch is a particularly elegant concept. This means that with the same energy in the springs, the carriage can travel the full length instead of half the length of the track which results in the acceleration to be more gradual. Therefore the force needed from the winch to tension the springs is halved, so that more energy can be put in the springs by pre-tensioning.

The carriage holds the steering unit enclosure by means of hooks. Before the acceleration of the linear accelerator, the steering unit enclosure is pressed backwards into these hooks which prevent it from lifting off the platform once the canopy generates lift as the arm swings round. As the arm is swung over and inflates the parafoil enough, it releases the carriage. At the end of the track however, the carriage will decelerate strongly, which causes the enclosure to move forward and release itself from the attachment. It is at this moment that the entire parafoil system (payload/steering unit and parafoil) is launched simultaneously. Figures 2.21-2.23 show the parafoil launcher in the pre-flight unloaded condition, ready for flight loaded condition and the after release condition respectively. See also Fig. 4.1.

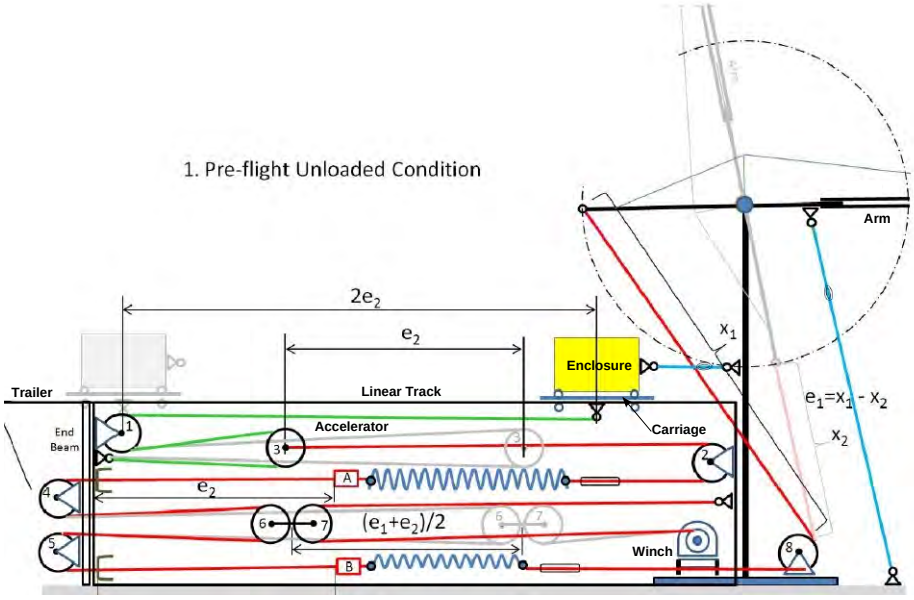

Figure 2.21: Parafoil Launcher in Pre-Flight Unloaded Condition [58]

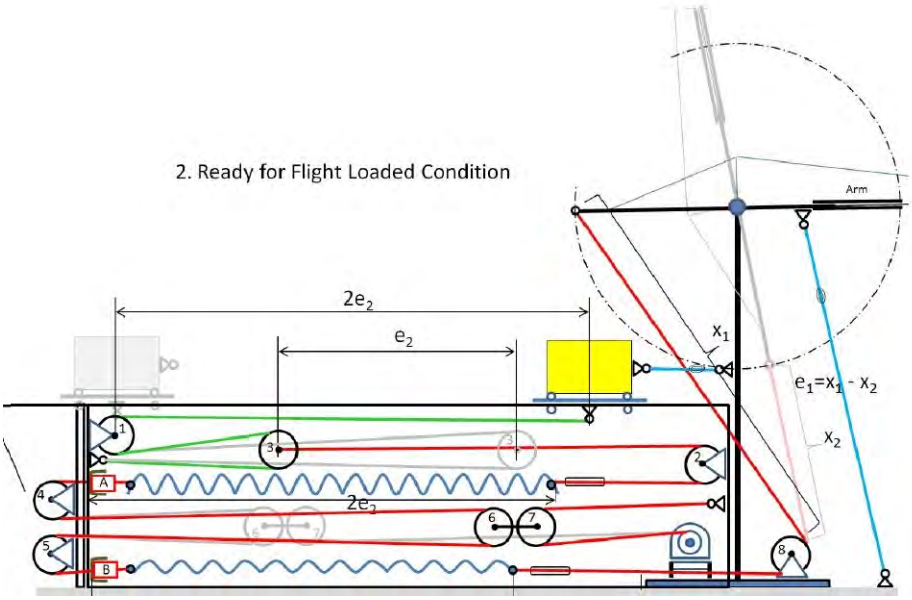

Figure 2.22: Parafoil Launcher Ready for Flight Loaded Condition [58]

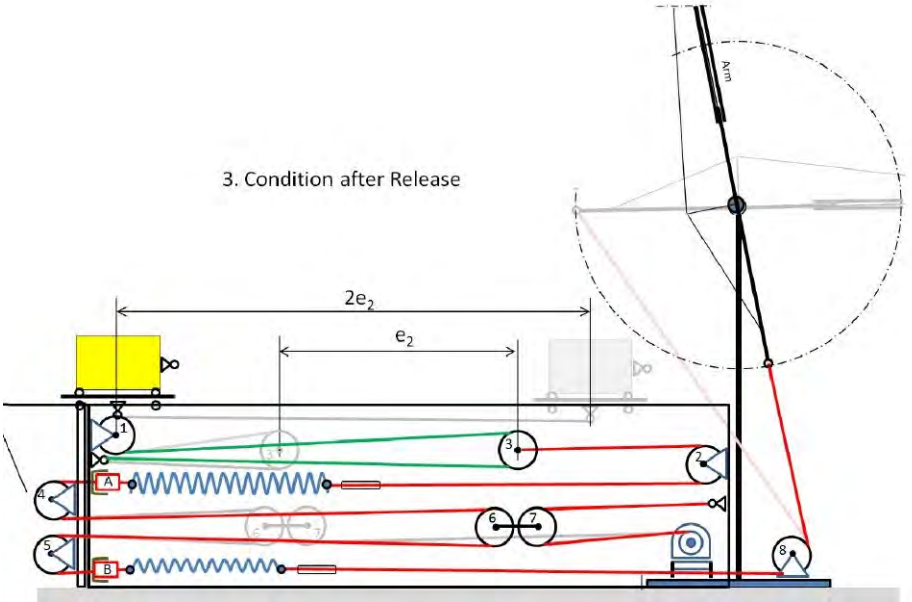

Figure 2.23: Parafoil Launcher Condition after Release [58]

Figure 2.24: An Aerial View of the Parafoil Launcher

Figure 2.24 illustrates the actual parafoil launcher in action during a dummy payload test. Frame one shows how the canopy inflates as the arm swings over and the second frame captures the moment just after the arm releases the carriage. In the third frame, the carriage can be seen at the end of the track and the steering unit enclosure has detached itself. The parafoil system is launched successfully and allowed to glide, with or without the aid of control inputs from the electronic steering unit.

Electronic Steering Unit

The electronic steering unit developed for the University of Cape Town parafoil research, although unused in this project, contains two servo motors that are connected to winch drums via planetary gearboxes. The winches are designed to rotate freely on two standard deep groove ball bearings (6004) that have static load ratings of 5 kN each. This ensures that in the event of a crash landing, the winch drum is well supported and the gearbox is somewhat protected [58]. The steering or control lines of the parafoil will be placed around the winch drums of the steering unit, which is indicated in Fig. 2.25 and Fig. 2.26.

The rest of the steering unit comprises of four lead-acid gel batteries, two controller boards and the avionics equipment. Two batteries are placed on either side of the longitudinal centreline of the payload box ensuring symmetry, embedded in the protective foam. The two controller boards with the on-board micro processor are placed between the two upper cylindrical tubes, with its cooling surface facing towards the middle. The space in the middle should be kept free of equipment for allowing air to pass through for cooling. The avionics equipment, the communication with the ground and supporting

electronics, must be insulated from the main assembly. The entire steering unit is enclosed using flexible foam rubber packaging as shock protectors. The foam padding is designed and cut into precise shape to snugly accommodate the assemblies, like the packaging used when transporting delicate instrumentation [58]. Refer to Fig. 2.26 which illustrates the steering unit layout.

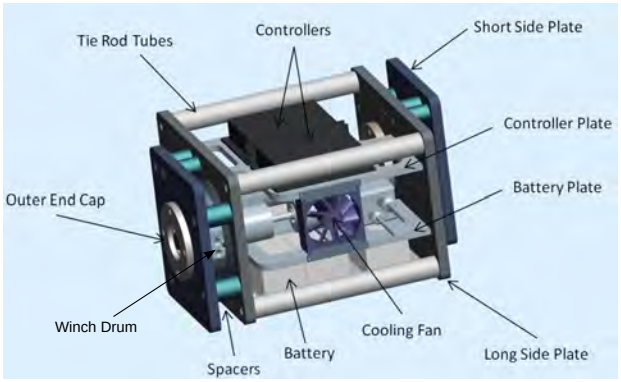

Figure 2.25: 3D CAD Model of the Electronic Steering Unit [58]

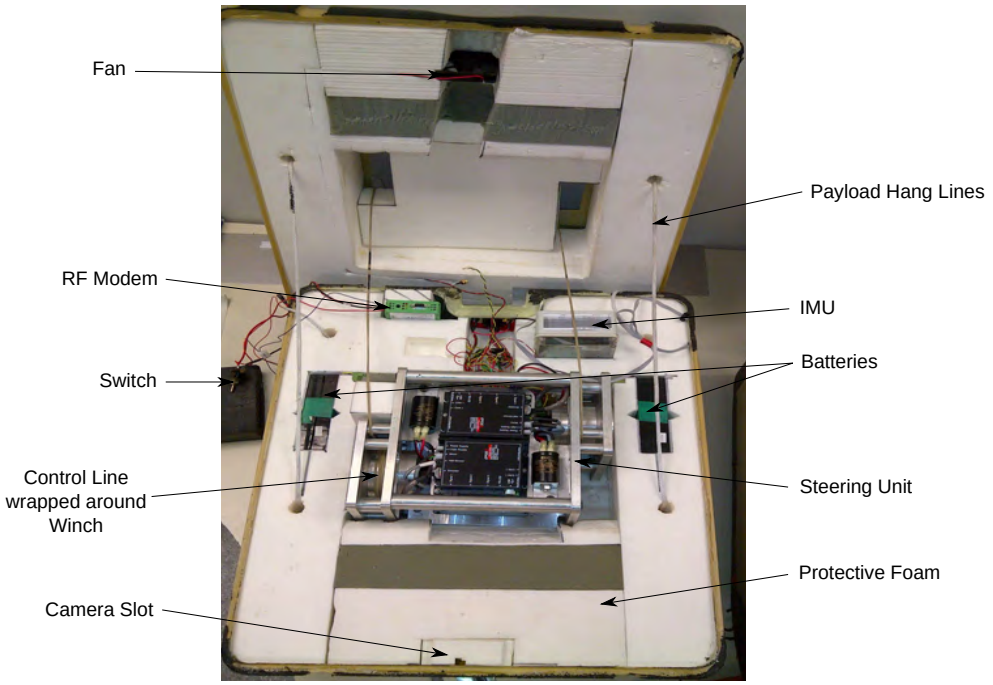

Figure 2.26: Layout of the Steering Unit

With respect to the functioning of the electronic steering unit, it consists of two computer-controlled winches that will manipulate the steering lines of the parafoil. See Fig. 2.26. These steering lines are connected to the two parafoil brakes, and just like a human being flying a para-glider pulls the steering lines by hand, the computer-controlled winches perform this human-like function by reeling in the control lines. Therefore; left turns, right turns and flares are easily performed. The servo motors, that rotate these winches, receive their commands remotely from a ground station or from an on-board flight computer. The electronic steering unit therefore allows for autonomous or unmanned flight of the parafoil. For more information on the functioning of the steering unit refer to Grunwald et al [58]. Yatoh et al [47] adopted a similar approach to controlling their parafoil recovery system for an experimental rocket. If the parafoil turns the rocket to the right or left direction, the servo motor rolls up the right or left riser respectively to decline the lifting surface. This operation can be realised by the riser control mechanism as shown in Fig. 2.27. The rocket is guided by the parafoil to a target position by repeating this operation [47].

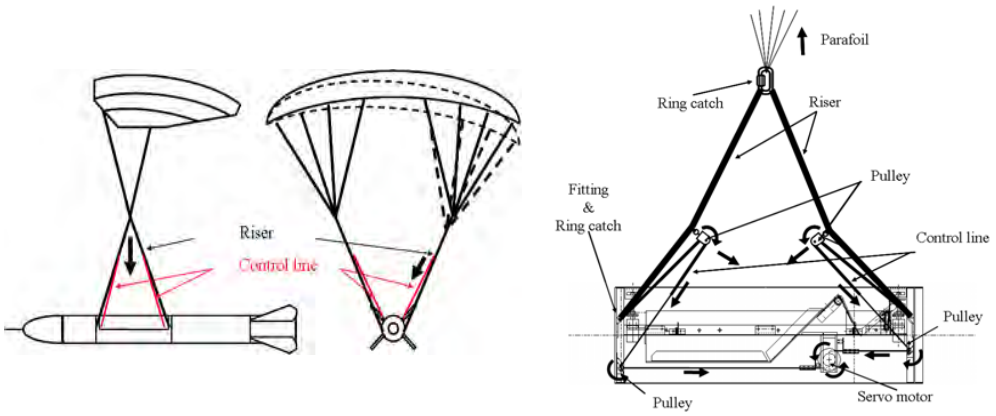

Figure 2.27: Riser Control Mechanism of Parafoil [47]

It should be noted that throughout the course of this project, minor adjustments and modifications, to both the functioning of the parafoil launcher and the electronic steering unit, might be performed as new problems and ideas arise. But as this is outside the scope of this project, the above section only describes the general functioning of these two systems, which is more likely to be the same regardless of any minor adjustments and modifications that might take place.

2.3 Approaches for Determining the Optimum Glide Slope

Following from Sections 2.1.3 and 2.1.4, one may assume, and indeed be correct in doing so, that in order to infer an optimum glide angle for a parafoil-payload system or glider, one would only need to determine the drag polar of the entire system and then ensure that trim changes allow for flight at the desired airspeed. A drag polar, defined in most aerodynamics textbooks, is the plot of drag coefficient versus lift coefficient and is often given by the following equation [59]:

$$C_D = C_{D0} + \frac{{C_L}^2}{\pi e \mathcal{R}} \tag{2.17}$$

The optimum glide angle can then be determined by a tangent line to the polar curve, because the tangent gives the maximum L/D point (see Fig. 2.28). An example of this approach is demonstrated by Geiger and Wailes [60] in their technical report. Using the standard equation of aerodynamic efficiency in gliding flight (refer to Equation 2.5), the higher the lift-drag ratio, the smaller the glide angle becomes and the greater the gliding range for a given height loss, thus the greater the aerodynamic efficiency.

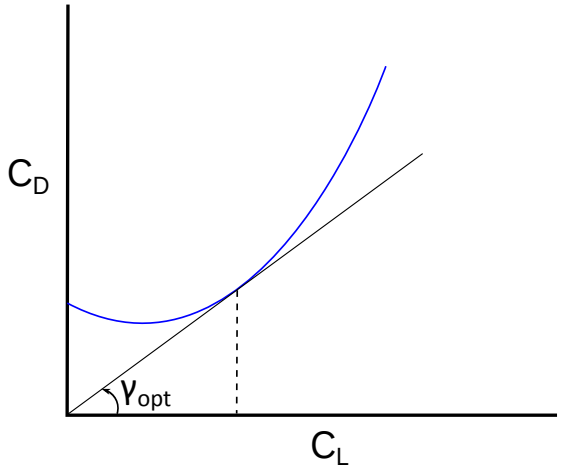

Figure 2.28: Drag Polar

With the aid of accurate IMU's and other sensors, lift and drag (and other aerodynamic) coefficients of the parafoil-payload system could be derived during flight tests from the sensor measurements. Precise photography and video recordings could also be used in an attempt to determine the glide slope. However, deriving lift and drag coefficients, particularly for analysis of the drag polar, from actual flight tests presents some difficulties. Firstly,

the approach is susceptible to turbulence and secondly, it could require high launching costs. For example, launching from altitude would require the parafoil-payload system to be dropped by an aircraft or for the entire system to be powered. Whereas the research and development currently being undertaken at the University of Cape Town, using this parafoil flight testing system, aims to pave the way in developing *low-cost* systems that meet the basic accuracy demands. The logistic and cost implications associated with launching from an aircraft or having a powered system are unrealistically high for this project, it is simply not feasible. There is also a trade-off by launching from higher altitude, for too long a flight would make recovery of the system difficult, especially if a fully operational steering unit has not been implemented.

Wind tunnel testing presents an alternative to flight testing, although it is also quite challenging to test parafoils or ram-air-inflated wings in a wind tunnel. Some of the issues include: 1) As with flight testing, canopy porosity and flexibility of the parafoil make it difficult to accurately measure lift and drag coefficients. Any increase in permeability will cause a reduction in the maximum obtainable lift-drag ratio due to pressure losses [1, 3–5]. 2) To test parafoils in a wind tunnel, small scale models are often required and the validity of scaling thus becomes questionable. Geiger and Wailes [60] state: "the problem is that the (scaled) models and the full scale parafoils may not distort in the same way or in the same relative amount." 3) The parafoil lines contribute significantly to the total drag of the system, and to accurately rescale the line characteristics (line length and line diameter) for wind tunnel testing is challenging. Nicolaides and Tragarz [6] computed lift and drag coefficients for parafoils of various aspect ratios in their study, by means of actual flight tests and wind tunnel tests. They reinstate that during flight tests, "variations in the wind made accurate measurements difficult."

Design of experiments is a disciplined statistical engineering process that seeks to find optima and the methodology does not necessarily require any knowledge of the underlying physical model. DOE could be used for optimisation of a system by means of flight tests, wind tunnel tests or simulations. More significantly, DOE provides insight to factor effects and their interaction, highlighting important system trends. Therefore, DOE offers the advantage of finding the optimum glide angle without access to a drag polar. If optima cannot be obtained, DOE could still provide useful information on the influence of more variables (trim settings) on a measured response (glide slope). The next section provides a more in depth view into DOE and a few of the aspects regarding DOE will be implemented in this investigation.

2.4 Design of Experiments

Designed experiments can be utilised in industry to systematically investigate the process or product variables that influence product quality. Once the process conditions and product components that influence product quality have been identified, improvement efforts can be made to enhance a product's manufacturability, reliability, quality, and field performance. Due to limited resources, it is of utmost importance to get the most information from each experiment performed. "Well-designed experiments can produce significantly more information and often require fewer runs than haphazard or unplanned experiments. In addition, a well-designed experiment will ensure that you can evaluate the effects that you have identified as important." An interaction effect occurs when one input variable is influenced by the level of another input variable [61].

Design of Experiments (DOE) and Taguchi's methods are used whenever the settings of important variables need to be investigated; and not only for manufacturing processes. DOE and the Taguchi approach are used in many fields such as: environmental sciences, agricultural sciences, physics, chemistry, statistics, management and business, and medicine [62]. Ilzarbe et al [63] explore the practical applications of Design of Experiments in the field of engineering. In their paper, the three most prominent fields of application are materials, mechanical and chemical engineering, in that specific order. With respect to aerodynamics and flight testing, DeLoach [64], Bordelon [65] and Fletcher [66] have all implemented DOE and Taguchi's methods in their respective studies.

The literature presented in this section follows closely from Fisher [67], Cox [68], Hicks [69], Hinkelmann and Kempthorne [70], Kirk [71], Fowlkes and Creveling [72], and Oehlert [73].

Introduction to Experimental Design

Let us begin by describing what an experiment is. According to Hicks [69]; "a true experiment may be defined as a study in which certain independent variables are manipulated, their effect on one or more dependent variables is determined, and the levels of these independent variables are assigned at random to the experimental units in the study." An experimental unit may be defined as the object independently treated or changed in an experiment. It may be a part, a person, a class, a group of parts, a time-frame (i.e. day, week or month), or the smallest division of the experimental material that

can be given different treatments. The experimental units make up an universe of all such units (i.e. the experimental material), and a population is defined as measurements taken on all experimental units in the universe [69].

Manipulation and randomisation are essential for a true experiment if one were to infer cause and effect. It is not always physically possible to assign some variables to the experimental units at random, but it may be possible to run a quasi-experiment in which groups of units are assigned to various levels of the independent variable at random [69]. Cox [68] states: "The requirements for a good experiment are then that the treatment comparisons should as far as possible be free from systematic error, that they should be made sufficiently precisely, that the conclusions should have a wide range of validity, that the experimental arrangement should be as simple as possible, and finally that the uncertainty in the conclusions should be assessable."

Experimental design consists of three main aspects: the experiment, the design and the analysis [69]. The experiment includes a statement of the problem to be solved. It is important to bring out all points of view to establish just what the experiment is intended to do. It is also necessary to define the independent variables or factors that may affect the dependent or response variable. These factors can be held constant, manipulated at certain specified levels, or be averaged out by a process of randomisation. Factors whose levels are set at specified values are called *fixed effects*, and those set at random levels *random effects*. The factors to be varied can be quantitative (such as temperature) or qualitative (such as operators) [69]. How the factor levels are to be combined must also be considered before conducting the experiment. For example, if one factor A is set at three levels and a second factor B is set at two levels, can one set all six combinations as follows?

Table 2.2: Example of a Factorial Experiment [69]

	A1	A2	A3
B1			
B2			

This is called a factorial experiment as all levels of A are combined with all levels of B [69]. It is an example of a treatment design, where the treatments may be determined by various treatment factors and level combinations of

such factors [70]. Factorial experiments will be discussed in more detail later.

The design must specify the number of observations to be taken, as well as the order of the experimentation, which should be random order. This is known as an error-control design. Considerations of how large a difference is to be detected, how much variation is present, and what size risks are to be tolerated are all important in deciding on the size of the sample to be taken for a given experiment [69]. Hicks [69] suggests that without this information it is best to take as large a sample as possible. That would result in an example of a sampling and observation design [70]. Once it has been decided to control certain variables at specified levels, despite there being a number of other variables that cannot be controlled, randomisation can be implemented. Randomisation of the order of experimentation will tend to average out the effect of these uncontrolled variables [67–70].

There are basically three ways to handle independent variables in an experiment, as documented by Hicks [69]:

1. Rigidly controlled. The variables remain fixed throughout the experiment, which, of course, means that any inferences drawn from the experiment are valid only for these fixed conditions.

2. Manipulated or set at levels of interest. These would be the variables whose effect on (say) y are to be studied. They could be either qualitative or quantitative and their levels either fixed or random. To be effective, every effort should be made to include the extreme levels of such variables to provide opportunity to maximize their effect, if present.

3. Randomised. As mentioned above, the order of experimentation is randomised to average out the effects of variables that cannot be controlled. Such averaging does not remove their effect completely as they still increase the variance of the observed data. Proper design of the experiment can also reduce or minimize the experimental error when such factors are anticipated.

In the design of the experiment, the experimenter must specify the method of randomization to be used (by flipping a coin, picking numbered balls out of a well-shaken bag, etc.). Aside from this, a mathematical model to describe the experiment and the hypotheses to be tested must be considered during the design phase of experimental design [69].

The final aspect of experimental design is the analysis. This includes the data collection and processing, the computation of test statistics, and the interpretation of results by the experimenter [69]. "A major aim of analysing data from designed experiments is to quantify and evaluate the importance of possible sources of variation. This can be achieved through the analysis of variance (ANOVA) associated with the underlying linear model." Given experimental observations, y say, the general idea of ANOVA is to partition the "total variability" (or total sum of squares), $SS(Total) = \Sigma(y - \bar{y})^2$, into component parts as specified by an underlying linear model [70].

According to Hinkelmann and Kempthorne [70], the linear model relates to the subject matter model and the experimental design. The general idea is to express the observations, generally denoted by y, in terms of *effects* which contribute to y. These effects or components can be categorised into three types: treatment effects, design effects, and error effects. Treatment effects are a reflection of the intervention procedure or treatment design as either single treatments or factor combinations are applied. Error-control designs establish what the design effects are, in particular, the effects due to the various kinds of blocking. Finally, the error effects represent different kinds of random variation [70].

$$\begin{aligned} \text{Observation} &= \text{Design effect} \\ &= + \text{ Treatment effect} \\ &= + \text{ Experimental error} \\ &= + \text{ Observational error.} \end{aligned}$$

Three Principles of Experimental Design

Replication is the first principle of experimental design. This means that the same treatment/condition (or some of the same treatments/conditions) must be applied to several experimental units. Replication facilitates in approximating the experimental (random) error among experimental units treated alike. [70, 71]. Fisher [67] claims that replication has two distinct purposes. It serves first to diminish the error and secondly, plays an important but limited role in increasing the precision of an experiment. It is clear to see that repeating the experiment will increase the sensitiveness.

To ensure validity of the estimate of experimental error, one must rely on the second principle which is that of *randomisation* [70]. This was also stated by Fisher [67] in his book entitled *"The Design of Experiments"*, where he

says: "The purpose of randomisation in this, as in the previous experiments exemplified, is to guarantee the validity of the test of significance, this test being based on an estimate of error made possible by replication." Randomisation leads to an unbiased estimate of variance as well as an unbiased estimate of treatment differences, i.e., estimates that are free from systematic differences due to otherwise uncontrolled variation [70, 71]. The basic operation of randomisation is that of arranging in "random order" a series of numbered objects. According to Cox [68], one of the essential features of randomisation is that it should be an objective impersonal procedure; to arrange things in random order does not mean just to manipulate them into some order that looks haphazard. One method of randomising is to shuffle numbered cards or to draw numbered balls out of a well-shaken bag. The main method is to use numerical random tables.

One of the main objectives in choosing an appropriate error-control design is, in fact the reduction of experimental error. In many cases this is achieved by means of the third principle, that of *local control* or *blocking* [70]. This concept, first introduced by Fisher, is indeed one of the most important concepts in the subject of experimental design and all error-control designs. The basic idea is to partition the total set of experimental units into subsets (blocks) that are as homogeneous as possible. In this way the effects of nuisance factors which contribute systematic variation to the differences among experimental units can be isolated [70, 71]. "This in turn will lead to a more sensitive analysis since, loosely speaking, the experimental error will be evaluated in each block so generated and then pooled over the whole experiment. Such blocking can occur in various ways and at various stages of the experiment, and is dictated by the experimental conditions and the requirements on the desired sensitivity of the experiment" [70].

The Latin square design and the split-plot design are examples of more complicated blocking structures. These will be discussed in greater detail later. An experiment becomes more sensitive the more blocking is done, however, only up to a certain point and it depends on the amount of systematic variability associated with blocking factors. Meaning that it is a function of the given experimental situation and the amount of knowledge one has about it. Also, increasing the amount of blocking will always lead to more complex experiments, complex from not only the point of view of the execution, but as well as the analysis [70].

Different Types of Experimental Designs

The following section serves to describe some (and not all) of the experimental designs used today. As most of these experimental designs are outside the scope of this project, only a brief summary of each will be provided for the reader.

Single Factor Experiments. Single factor experiments are experiments where only one factor is varied, whether the levels be quantitative or qualitative, fixed or random. [69]. Fisher [67] states that often in experimentation, it is common to find an excessive stress laid on the importance of varying the essential conditions *only one at a time*. This is also known as "One-Factor-at-a-Time Experiments" [72]. The first factor is thoroughly studied under fixed conditions, being careful to isolate the causes which contribute to a certain effect. Once it is well characterised and a *control* is established, the experimenter moves on to study another factor thoroughly, until all factors are well characterised. This approach has been successful in developing a scientific understanding of the effect of a parameter or single factor [72].

Randomised Complete Block Designs. In randomised complete block designs, the experimental material is divided into b sets or *blocks* of t experimental units each, such that the experimental units within a set are as homogeneous as possible and that differences among the experimental units are accounted for as much as possible by differences between the sets [70]. In other words, the blocks are the groupings of experimental units for homogeneity and randomisation is restricted within these blocks [69]. Therefore, within each block, the treatments are randomly assigned to the experimental units independently, each treatment occurring exactly once in a block [70,73]. Blocking an experiment is a valuable technique to decrease the experimental error and increase the precision of an experiment, because of the homogeneous blocks [69, 73].

Latin Square Designs. A design in which each treatment appears once and only once in each row and once and only once in each column is called a Latin square design [68–70, 73]. The two blocking factors or restrictions are represented by the rows and columns. "Such a design is only possible when the number of levels of both restrictions equals the number of treatment levels. In other words, it must be a square" [69]. The Latin square is a method which is singularly reliable in giving precise comparisons according to Fisher [67], because it eliminates the effects of two sources of uncontrolled variation [67–71]. Below is an example of a 3×3 Latin square in its standard

form [70] (i.e. the first row and the first column are arranged in alphabetical order):

$$\begin{array}{ccc} A & B & C \\ B & C & A \\ C & A & B \end{array}$$

Graeco-Latin Square Designs. An interesting and sometimes useful generalisation of the Latin square design is obtained by considering elimination of heterogeneity in more than two directions, i.e. imposing another restriction or blocking factor on the randomisation. This means superimposing two Latin squares on each other with the resulting third property. We refer to such an arrangement as two orthogonal Latin squares, or more specifically, as a Graeco-Latin square [68–70] (the name is suggested by the use of Greek and Latin letters). Superimposing three orthogonal Latin squares will yield a design that is homogeneous in four directions [70]. For four or more sources of variability, we use Latin Hyper-Squares [73]. Below is an example of a 3×3 Graeco-Latin square:

$$\begin{array}{ccc} A\alpha & B\beta & C\gamma \\ B\gamma & C\alpha & A\beta \\ C\beta & A\gamma & B\alpha \end{array}$$

Full Factorial Experiments. A full factorial experiment is one in which the treatments consist of all combinations of different *levels* of a set of *factors* [67–70, 72, 73]. Efficiency is one of the main advantages of experiments designed on the factorial system, because every trial run supplies information upon each of the main questions which the experiment is designed to examine [67, 69]. Some information is also obtained on possible interactions between factors [68–70]. Fisher [67] states that factorial arrangement possesses two advantages over experiments involving only single factors: (i) greater *efficiency* and (ii) greater *comprehensiveness*.

There are various ways to implement factorial experiments. One method would be to estimate the effect of a factor, say A, keeping all the other factors at a constant level in one experiment. Then in the next experiment, estimate the effect of factor A after changing the level of factor B, and keeping the remaining factors at a constant level. "This procedure of varying one factor at a time would generally be used when the purpose is to establish a fundamental law as it would lead to detailed knowledge of the effect of one factor when the others are held constant" [70]. Information about the reliance of the effects of a factor on the levels of other constant factors cannot be obtained.

In order to obtain such information, one needs to vary the levels of each of the factors and consider all possible level combinations simultaneously. This procedure would allow one to obtain information about the main effects and, more importantly, about interactions among various factors [67–70].

Treatment Name	Factors	
	A	*B*
(1)	-1	-1
a	1	-1
b	-1	1
ab	1	1

(a)

I	*A*	*B*	*AB*
1	-1	-1	1
1	1	-1	-1
1	-1	1	-1
1	1	1	1

(b)

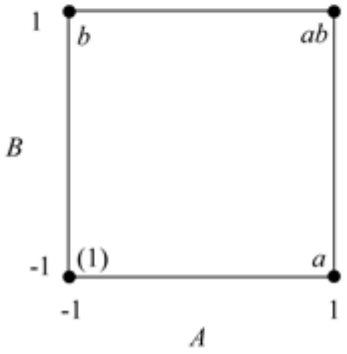

(c)

Figure 2.29: Example of a 2^2 Factorial Design [74]

The most commonly used factorial designs are the 2^f and the 3^f factorials, where f equals the number of factors; and 2 and 3 are the number of levels respectively [68–71, 73]. In the case of 2^f factorial experiments, these

levels may be two extremes of temperature, two extremes of pressure, two time values, two machines, etc [69]. The use of just two levels is advisable in experiments in which the object is to see whether the factor has an appreciable effect and in which direction the effect is. 2^f factorials are very useful for at least two reasons according to Hicks [69]: to introduce notation and concepts useful when more involved designs are discussed, and to illustrate what main effects and interactions there really are in this simple case. 3^f factorials consider f factors at three levels, thus there are 2 degrees of freedom between the levels of each of these factors. There is now a low, intermediate, and high level for each factor. Three levels should be used in order to give some estimate of the shape of the response curve [69, 70, 72, 73].

The simplest case to consider for 2^f factorials is one in which two factors (say A and B) are of interest and each factor is set at just two levels. The levels are generally denoted by -1 (low level) and $+1$ (high level). This is a $2 \times 2 = 2^2$ factorial, and the design will be considered as completely randomised. This gives four treatment combinations, unless there is some replication [68–70]. Often the notation used for this design is as follows: "If both factors are at their low levels, $a^0b^0 = (1)$, and (1) represents the response of both factors at their low level. $a^1b^0 = a$ represents the high level of A and the low level of B, $a^0b^1 = b$ represents B at its high level and A at its low level, and $a^1b^1 = ab$ represents the response when both factors are at their high levels. This notation can easily be extended to more factors, provided only two levels of each factor are involved" [69]. The treatment combinations of a 2^2 factorial can be represented by the vertices of a square. Refer to Fig. 2.29.

The effect of a factor is defined as the change of a response produced by a change in the level of that factor [67–73]. At the low level of B, the effect of A is then $a - (1)$, whereas the effect of A at the high level of B is $ab - b$ [69]. The average effect of A is then:

$$A = \frac{1}{2}[a - (1) + ab - b] \tag{2.18}$$

The average effect of B, based on low level of $A(b - (1))$ and high level of $A(ab - a)$, is:

$$B = \frac{1}{2}[b - (1) + ab - a] \tag{2.19}$$

To determine the effect of the interaction between A and B, note that at the high level of B the A effect is $ab - b$, and at the low level of B the A effect is $a - (1)$. If these two effects differ, there is an *interaction* between

A and B. Thus the interaction is the average difference between these two differences [69]:

$$\begin{aligned} AB &= \frac{1}{2}[(ab - b) - (a - (1))] \\ &= \frac{1}{2}[ab - b - a + (1)] \end{aligned} \tag{2.20}$$

This notation can easily be extended to 2^f factorials with more factors. In the case of three factors, the experiment will be a $2 \times 2 \times 2$ or 2^3 factorial. There are now 8 treatment combinations and they are: $(1), a, b, ab, c, ac, bc, abc$; and they may be represented as vertices of a cube, as shown in Fig. 2.30.

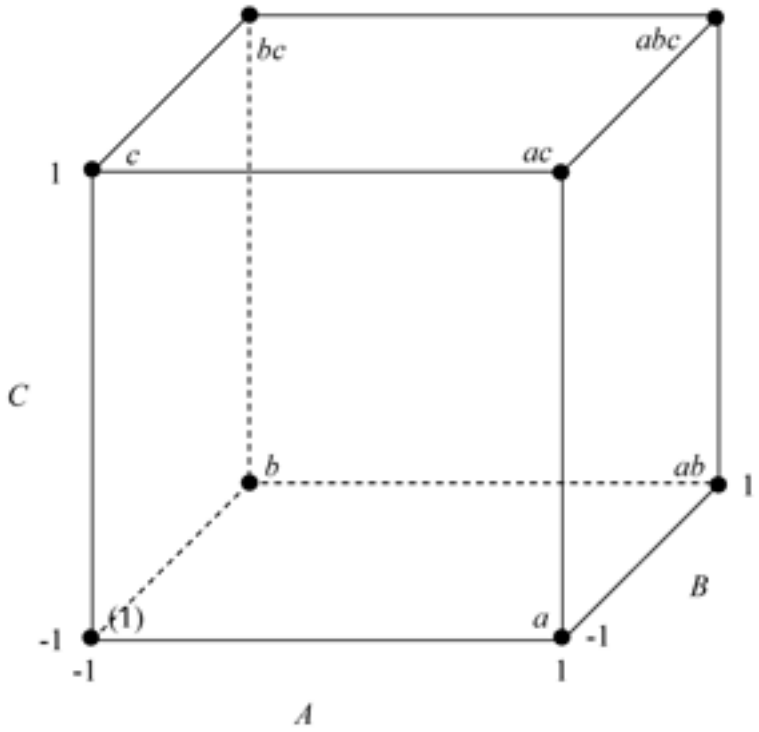

Figure 2.30: Schematic of a 2^3 Factorial Design [74]

The general rule for defining the main effects and interactions for the 2^f factorial, summarised by Hinkelmann and Kempthorne [70], is as follows. Any effect or interaction X say, can be represented as:

$$X = \frac{1}{2^{f-1}}(a^1 \pm a^0)(b^1 \pm b^0)(c^1 \pm c^0)(d^1 \pm d^0)\ldots \tag{2.21}$$

where the sign in each bracket is negative if the corresponding capital letter is contained in X and positive if it is not contained in X, and the whole expression on the right-hand side is to be expanded algebraically and interpreted in terms of treatment combination responses [70].

The simplest case to consider for 3^f factorials is one in which two factors (say A and B) are of interest and each factor is set at three levels. This is a $3 \times 3 = 3^2$ factorial, and there are $3 \times 3 = 9$ treatment combinations [68–70]. The levels are generally denoted by 0 (low level), 1 (intermediate level) and 2 (high level). Sometimes -1, 0 and $+1$ can be used to represent the low, intermediate and high levels of a factor respectively. This notation is often used for computational ease [75]. Figure 2.31 illustrates the data layout for a 3^2 factorial design. "Two digits are used to describe each of the nine treatment combinations. The first digit indicates the level of factor A, and the second digit the level of factor B" [69]. Thus, 10 means A is at its intermediate level and B is at its low level.

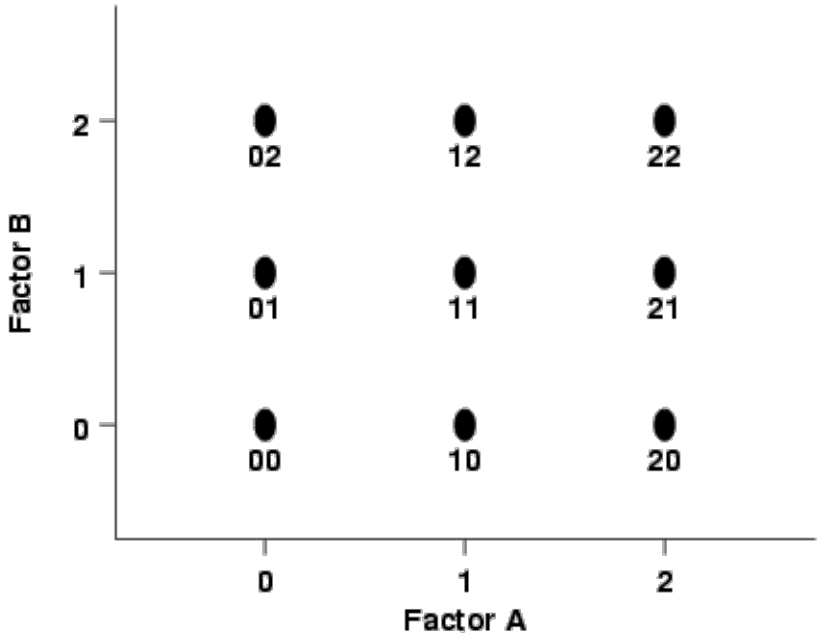

Figure 2.31: Schematic of a 3^2 Factorial Design [76]

This notation can also be easily extended to more factors and to as many levels as required. Consider a $3 \times 3 \times 3 = 3^3$ factorial design; where the experimenter has three factors (say A,B and C), each at three levels. Again, the levels are generally denoted by 0 (low level), 1 (intermediate level) and 2 (high level). Figure 2.32 illustrates the data layout for a 3^3 factorial design, showing all possible 27 treatment combinations. Three digits are now used to describe each of the 27 treatment combinations. The first digit indicates the level of factor A, the second digit the level of factor B, and the third digit the level of factor C. Thus, 012 means A is at its low level, B is at its intermediate level, and C is at its high level.

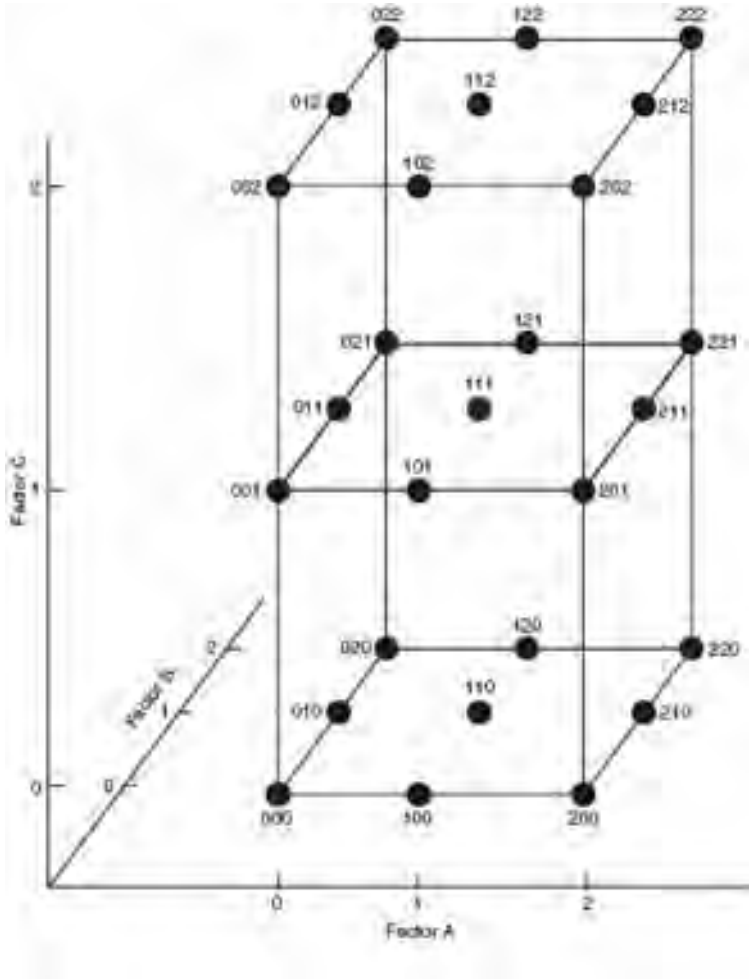

Figure 2.32: Schematic of a 3^3 Factorial Design [77]

Fractional Factorials. Increasing the number of factors in a factorial

experiment results in the number of treatment combinations increasing very rapidly (exponentially) [68–70]. An example of this can be demonstrated with a 2^f factorial where $f = 5$ requires 32 experiments for one replication, $f = 6$ requires 64, $f = 7$ requires 128, and so on. The number of high-order interactions increase with an increase in the amount of experimentation. High-order interactions are difficult to explain if found significant and therefore some of these high-order interactions, those above second order, may be used as error [69]. Table 2.3 illustrates the number of main effects, first-order, second-order, etc interactions that can be recovered if a complete 2^f factorial can be run.

Table 2.3: Build up of 2^f Factorial Effects [69]

f	2^f	Main Effect	1st	2nd	3rd	4th	5th	6th	7th
5	32	5	10	10	5	1			
6	64	6	15	20	15	6	1		
7	128	7	21	35	35	21	7	1	
8	256	8	28	56	70	56	28	8	1

In the case of $f = 7$, "there will be 7 degrees of freedom (df) for the seven main effects, 21 df for the 21 first-order interactions, 35 df for the 35 second-order interactions, leaving

$$35 + 21 + 7 + 1 = 64 \; degrees \; of \; freedom$$

for an error estimate, assuming no blocking. Even if this experiment were confounded in blocks, there is still a large number of degrees of freedom for the error estimate" [69]. "Confounding is a technique for arranging factorial experiments in blocks, with fewer units per block than there are treatments in the experiment, or in square or rectangular designs with fewer rows and columns than there are treatments. Information is sacrificed about certain selected contrasts, usually high-order interactions, in order that the remaining contrasts can be estimated with the higher precision that should result from the use of smaller blocks" [68]. In such cases, it may not be feasible to run a whole replicate of 128 observations. Perhaps as much information could be obtained by only half as many observations, saving time and money by only running half the experiment. When only a fraction of a replicate is run, the design is called a *fractional replication* or a *fractional factorial* [68–70, 73]. Therefore, a *fractional-factorial* design is a modification of a standard factorial that allows us to get information on main effects

and low-order interactions without having to run the full factorial design [73].

To see how a fractional replication is run, consider the simple case taken from Hicks' [69] book, entitled *"Fundamental Concepts in the Design of Experiments"*. Say there are three factors, each at two levels. However, the experimenter cannot afford $2^3 = 8$ experiments and settles for four. This suggests a one-half replicate of a 2^3 factorial. Suppose interaction ABC is confounded with blocks. The two blocks are then:

$$I = ABC$$

$$block1 : [(1)\ ab\ bc\ ac]$$

$$block2 : [a\ b\ c\ abc]$$

where $I = ABC$ is the *defining contrast*. This is merely an expression stating which effects are to be confounded with blocks. Say (for randomisation purposes), a coin is flipped and the decision is made to run only block 2. Table 2.4 shows a one-half fraction of a 2^3 factorial, and only the treatment combinations in block 2 are boxed and run. Notice that in the boxed area, ABC has all plus signs in block 2, which is a result of confounding blocks with ABC. Note also that the effect of A is

$$A = +a - b - c + abc$$

and

$$BC = +a - b - c + abc$$

so we cannot distinguish between A and BC in block 2. Two or more effects that have the same numerical value are called *aliases*. We cannot tell them apart. B and AC likewise are aliases, as are C and AB. Because of this confounding when only a fraction of the experiment is run, we must check the aliases and be reasonably sure they are not both present if such a design is to be of value. An analysis of this one-half replication of a 2^3 factorial would be as shown in Table 2.5.

A quick way to find aliases of an effect in a fractional replication of a 2^f factorial experiment is to multiply the effect by the terms in the defining contrast, modulus 2. The results will be aliases of the original effect. In the example above,

$$I = ABC$$

The alias of A is

$$A(ABC) = A = A^2BC = BC$$

The alias of B is

$$B(ABC) = B = AB^2C = AC$$

The alias of C is

$$C(ABC) = C = ABC^2 = AB$$

This simple rule works for any fractional replication for a 2^f factorial. It works also with a slight modification for a 3^f factorial run as a fractional replication.

Table 2.4: One-Half Replication of a 2^3 Factorial [69]

Treatment Combination	A	B	AB	C	AC	BC	ABC
(1)	−	−	+	−	+	+	−
a	+	−	−	−	−	+	+
b	−	+	−	−	+	−	+
ab	+	+	+	−	−	−	−
c	−	−	+	+	−	−	+
ac	+	−	−	+	+	−	−
bc	−	+	−	+	−	+	−
abc	+	+	+	+	+	+	+

Table 2.5: Analysis of an One-Half Replication of a 2^3 Factorial [69]

Source	df
A (or BC)	1
B (or AC)	1
C (or AB)	1
Total	3

This would be an impractical experiment unless the experimenter is sure that no first-order interactions exist and has some external source of error to use in testing A,B, and C. The real advantage of such fractioning is seen on designs with larger f values. For 2^f factorials, $\frac{1}{2}$,$\frac{1}{4}$,..., to $\frac{1}{2^k}$ fractions are available. For 3^f factorials, $\frac{1}{3}$,$\frac{1}{9}$,..., to $\frac{1}{3^k}$ fractions are available, and the previous concepts may easily be extended to a 3^f factorial [69].

Response Surface Designs. Many experiments have the goals of describing how the response varies as a function of the treatments and determining treatments that give optimal responses, perhaps maxima or minima [73]. "In general, the dependence of treatment effects on treatments can be represented as a response curve (if the treatments are represented by the levels of one treatment factor) or a response surface (if the treatments are level combinations of two or more treatment factors)" [70]. These curves or surfaces can be used to draw conclusions about treatment structure and the relationship between treatments and responses (i.e. describing the response), or between input and output variables. If one wants to determine the treatment combination which results in the optimal (highest or lowest) response, then the knowledge of this relationship is important [70]. Approximating these relationships are done by using methods of experimental design and regression analysis known as response surface methodology (RSM) [70, 75].

Split-Plot Type Designs. Sometimes complete factorial experiments cannot be run in one single day, or in one environmental chamber, and thus restrictions need to be placed on randomisation [69, 73]. In addition, there exist many situations where for a factorial experiment, different types of experimental units are being used and where the levels of some factors are applied sequentially [70]. Therefore, in such situations, split-plot type designs are implemented. Split-plots have two types or sizes of experimental units and two randomisations [73]. In the simplest case of split-plots, one has experimental units of a specific size for the levels of one factor. Those experimental units are then subdivided into smaller experimental units to which the levels of the second factor are applied. This procedure is referred to as the *split-unit principle* [70]. The term split-plot comes from agricultural experimentation where the levels of, say, treatment A are applied to relatively large plots of land (the whole plots). The whole plots are then split or subdivided, and the levels of treatment B are applied to the subplots within each whole plot [70, 71, 73]. Split-plot designs are generally used when some of the factors are more difficult or expensive to vary than others. The key features of split-plot designs are that they have more than one randomisation and more than one idea of experimental unit [73].

Taguchi Approach to Design of Experiments

Since the early 1980s Taguchi methods to quality control have been used to optimize the process of engineering experiments [78]. Dr. Genichi Taguchi developed an engineering method of quality improvement referred to as *Quality Engineering* in Japan and as *Robust Design* in the West [72]. Regardless

of the name, Robust Design is a disciplined engineering process that seeks to find the optimum product design. In experimental terms, several factors are to be investigated in an effort to find the best/optimum combination of levels [70]. "Best" is carefully defined to mean that the design is the lowest-cost solution to the product requirement specification, which is based on the customer needs [72, 78]. He has also made several significant contributions to industrial statistics problems [69]. These include:

1. Loss functions that convert performance characteristics into societal loss measured in monetary units.

2. Signal-to-noise ratios that summarise the performance characteristic in decibels. A robust (insensitive) system will have a high S/N ratio [78].

3. Orthogonal arrays for gathering experimental results and their associated linear graphs for designing experiments.

4. Analysis of variance for analysing the results of the experiment and making decisions.

We are more interested with points 3 and 4 here. An orthogonal array is a type of experiment where the columns for the independent variables are "orthogonal" to one another, meaning that the columns are independent of one another. Therefore, orthogonal arrays are just highly fractionated factorial designs. The convention for naming fractional factorial orthogonal arrays is [72]:

$$La(b^c)$$

where

$$a = \text{the number of experimental runs}$$

$$b = \text{the number of levels for each factor}$$

$$c = \text{the number of columns in each array}$$

Two-Level Orthogonal Arrays. The notation $L4(2^3)$ means that we take four observations and at most three factors each at two levels. All cases use the orthogonal array design of Table 2.6, where -1 represents the low level of a factor and $+1$ represents the high level [69].

Table 2.6: $L4(2^3)$ Orthogonal Array Design [72]

Run	1	2	3
1	−1	−1	−1
2	−1	+1	+1
3	+1	−1	+1
4	+1	+1	−1

Note that column 3 is the negative of the products of columns 1 and 2. If A is assigned to column 1 and B to column 2, then column 3 is $-AB$ or the interaction. The first two columns of the $L4$ are the 2^2 full factorial [69, 72].

The $L8(2^7)$ design requires only eight observations to examine up to seven factors. If seven factors are to be studied, one must assume all interactions are non-existent. Examining seven main effects with only eight observations results in a one-sixteenth replication of a 2^7 factorial ($2^7/16 = 8$) [69]. Table 2.7 shows the $L8$, where the first, second, and fourth columns are the 2^3 full factorial [72].

Table 2.7: $L8(2^7)$ Orthogonal Array Design [72]

Run	1	2	3	4	5	6	7
1	−1	−1	−1	−1	−1	−1	−1
2	−1	−1	−1	+1	+1	+1	+1
3	−1	+1	+1	−1	−1	+1	+1
4	−1	+1	+1	+1	+1	−1	−1
5	+1	−1	+1	−1	+1	−1	+1
6	+1	−1	+1	+1	−1	+1	−1
7	+1	+1	−1	−1	+1	+1	−1
8	+1	+1	−1	+1	−1	−1	+1

Three-Level Orthogonal Arrays. Three-level orthogonal arrays allow us to investigate three factor levels. The $L9(3^4)$ design examines four factors with only nine experiments and less than four factors if some interactions are examined. Here each factor has two degrees of freedom [69, 72], and the interactions are of the form AB and AB^2. For example, four factors, say A,B,C, and D, each at three levels would require $3^4 = 81$ experiments for a

full factorial. To do this with nine experiments is a one-ninth replicate of a 3^4 factorial. No linear graphs are available for three-level orthogonal arrays because the effects can be quadratic [69]. Table 2.8 shows the $L9$, where the first two columns make up the 3^2 full factorial [72]. Note that -1, 0 and $+1$ represents the low, intermediate and high level of a factor respectively.

Table 2.8: $L9(3^4)$ Orthogonal Array Design [72]

Run	1	2	3	4
1	-1	-1	-1	-1
2	-1	0	0	0
3	-1	$+1$	$+1$	$+1$
4	0	-1	0	$+1$
5	0	0	$+1$	-1
6	0	$+1$	-1	0
7	$+1$	-1	$+1$	0
8	$+1$	0	-1	$+1$
9	$+1$	$+1$	0	-1

To summarise, several observations can be made concerning the use of Taguchi's experimental designs [69].

1. They present a procedure for examining many factors in an experiment using a very small number of observations.

2. In using such procedures one must usually assume that no interactions are present or, at least, be able to identify before the experiment some interactions and include them in the design.

3. Taguchi's orthogonal arrays are essentially fractional factorial experiments.

4. All main effects are independent of other main effects but are confounded with two-way or higher interactions when Taguchi's arrays are used on the maximum number of factors.

Chapter 3

Longitudinal Motion Parafoil Algorithm

In order to predict the behaviour of the parafoil-payload system, a rudimentary 4-DOF (2 components of translation, 1 pitching rotation and 1 component of relative parafoil-payload motion) model was developed to simulate the longitudinal motion of the system. The model allows for the capability of varying the trim settings of the system and investigating the effects this has on the glide slope. The forces acting on the parafoil canopy and the forces acting on the payload are coupled at the hinge point, denoted by H in Fig. 3.1 and 3.6. The wind and turbulence models discussed in Section 2.1.5 are incorporated into the dynamic simulation in an attempt to predict the response of the parafoil-payload system. The longitudinal motion parafoil algorithm developed was based on the following assumptions:

1. Only the longitudinal motion is considered, and it is independent of the lateral and directional motion.
2. The canopy has no mass.
3. The canopy and payload are assumed to be rigid bodies with one degree of freedom relative motion allowed between them. Any distortion of the canopy or suspension lines will not be accounted for.
4. The aerodynamic coefficients are constant.
5. The lines generate no lift force, however contribute to the drag of the system.
6. The drag force acting on the suspension lines may be approximated by n times that acting on a line corresponding to the plumb line, where n is the number of lines. Refer to Fig. 3.3 and 3.4.

3.1 Kinematics of Canopy and Lines

The kinematics of the canopy and lines is based on the plane kinematics of rigid bodies, assuming the changes in shape of the canopy and lines are very small compared with the movements of the body as a whole (*Rigid-body assumption*). Similarly, the displacements due to the vibrations of an aircraft wing, for instance, do not affect the description of the flight path of the aircraft as a whole, and thus the rigid-body assumption is clearly acceptable [79].

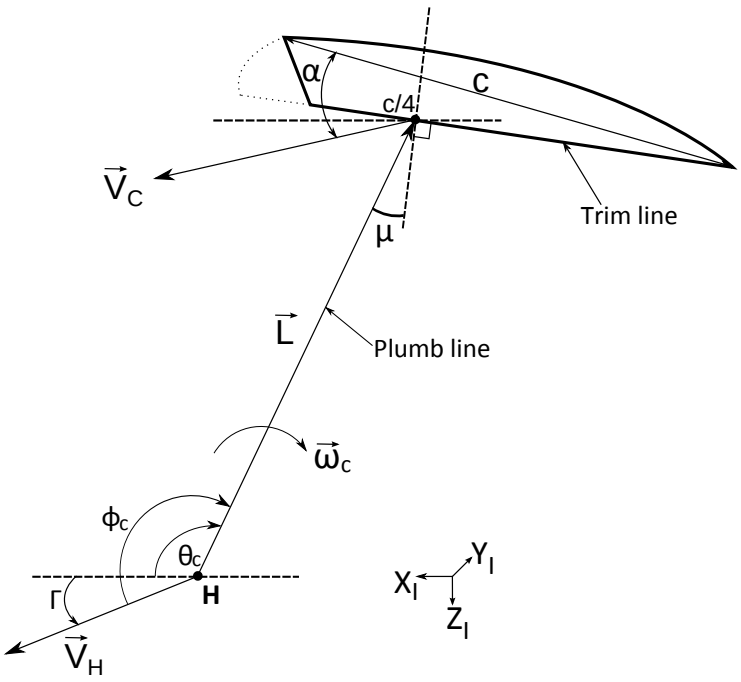

Figure 3.1: Kinematics of Canopy and Lines

Figure 3.1 is a schematic illustrating the kinematics of the canopy and lines. Using the absolute velocity due to rotation, the velocity of the canopy which is needed for the canopy aerodynamics, V_C, can be expressed as follows:

$$\vec{V}_C = \vec{V}_H + \vec{\omega}_C \times \vec{L} \tag{3.1}$$

Similarly,

$$\vec{V}_{L1} = \vec{V}_H + \vec{\omega}_C \times \frac{\vec{L}}{2} \tag{3.2}$$

$$\vec{V}_{L2} = \vec{V}_H + \vec{\omega}_C \times \frac{2}{3}\vec{L} \tag{3.3}$$

which is needed for the line drag (Refer to Fig. 3.3 and 3.4).

3.2 Aerodynamics of Canopy and Lines

Canopy

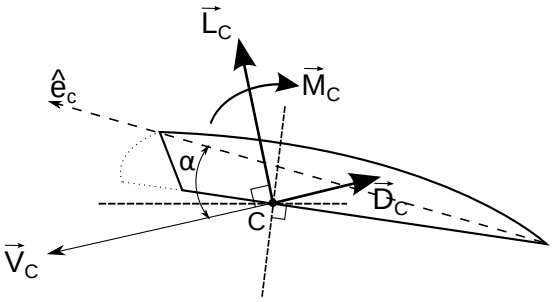

Figure 3.2: Aerodynamics of Canopy

Continuing from the previous section, the lift, drag and pitching moment acting on the canopy can be defined as follows:

$$\vec{L_C} = \frac{1}{2}\rho {V_{CW}}^2 S C_L(\hat{j} \times \vec{V}_{CW})/V_{CW} \tag{3.4}$$

$$\vec{D_C} = -\frac{1}{2}\rho {V_{CW}}^2 S C_D \vec{V}_{CW}/V_{CW} \tag{3.5}$$

$$\vec{M_C} = \frac{1}{2}\rho {V_{CW}}^2 S c C_m \hat{j} \tag{3.6}$$

Where:

$$C_L = C_{L0} + C_{L\alpha} \times \alpha$$
$$C_D = C_{D0} + \frac{{C_L}^2}{\pi \mathcal{R}_c}$$
$$C_m = C_{m0} + C_{m\alpha} \times \alpha$$
$$\sin\alpha = \frac{|\vec{V}_{CW} \times \hat{e}_C|}{|\vec{V}_{CW}||\hat{e}_C|}$$
$$\vec{V}_{CW} = \vec{V}_C - \vec{V}_w - \vec{V}_g \tag{3.7}$$

$\hat{e}_C$ is the unit vector in the direction of the chord line (a function of μ) and $\hat{j}$ is into the page. $\vec{V}_w$ and $\vec{V}_g$ are the mean wind and turbulent gust vectors respectively, that contribute to the relative canopy velocity, $\vec{V}_{CW}$.

$$\vec{V}_w = \left\{ \begin{array}{c} u_w \\ 0 \\ w_w \end{array} \right\} \; and \; \vec{V}_g = \left\{ \begin{array}{c} u_g \\ 0 \\ w_g \end{array} \right\}$$

u_w is the mean wind component described by Equation 2.9 and w_w is assumed to be zero. u_g and w_g are the gust velocities discussed in Section 2.1.5.

Lines

The lines of the parafoil contribute only to the drag on the entire system. However, there are two types of line drag, i.e. steady drag and "rotational drag". Steady line drag is defined when the pitch angle rate ($\dot{\theta}_c$ or $\vec{\omega}_C$) is equal to zero. At this instance, $\vec{V}_{L1} = \vec{V}_H$ and it is assumed that the steady line drag acts at half way up the line, i.e. at $\frac{L}{2}$. Refer to Fig. 3.3.

$$\hat{e}_{L1} = \vec{L} \times \hat{j}/L \tag{3.8}$$

$$V_{L1\perp} = \vec{V}_{L1} \cdot \hat{e}_{L1} \tag{3.9}$$

$$\vec{D}_{LS} = -\frac{1}{2}\rho(V_{L1\perp} - V_w - V_g)^2 ndLC_{DL}\hat{e}_{L1} \tag{3.10}$$

Steady drag ($\dot{\theta}_c = 0$)

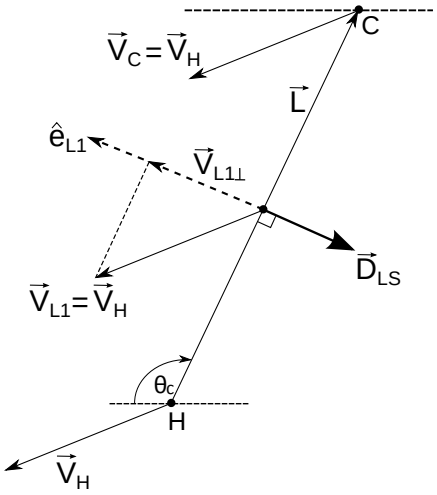

Figure 3.3: Aerodynamics of Lines (Steady Drag)

"Rotational" drag is defined when the pitch angle rate ($\dot{\theta}_c$ or $\vec{\omega}_C$) is *not* equal to zero. In this case, it is assumed that the line drag caused by the rotation acts at two thirds the way up the line, i.e. at $\frac{L}{3}$ from point C. This is

where the average velocity vector $\vec{V}_{L2\perp}$ acts due to the linear velocity profile. Refer to Fig. 3.4.

$$\vec{V}_{L2\perp} = \vec{\omega}_C \times \frac{2}{3}\vec{L} \tag{3.11}$$

$$\vec{D}_{LR} = -\frac{1}{2}\rho(V_{L2\perp} - V_w - V_g)^2 ndLC_{DL}\hat{e}_{L1} \tag{3.12}$$

"Rotational" drag ($\dot{\theta}_c \neq 0$)

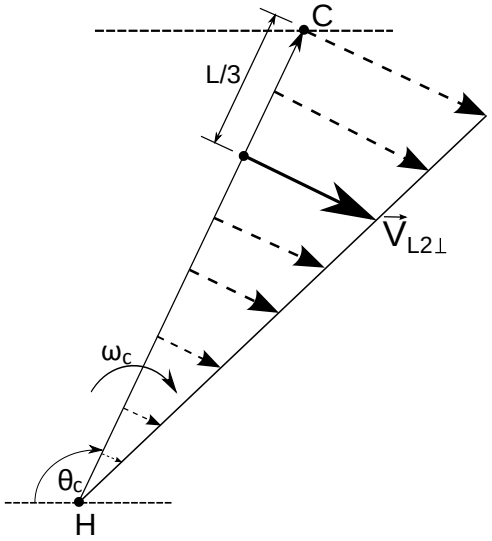

Figure 3.4: Aerodynamics of Lines (Rotational Drag)

3.3 Resultant Loads and Moment Balance

Now superimposing all the aerodynamic loads at C (Refer to Fig. 3.5):

$$\vec{L}_P = \vec{L}_C \tag{3.13}$$

$$\vec{D}_P = \vec{D}_C + \vec{D}_{LS} + \vec{D}_{LR} \tag{3.14}$$

$$\vec{M}_P = \vec{M}_C - \frac{\vec{L}}{2} \times \vec{D}_{LS} - \frac{\vec{L}}{3} \times \vec{D}_{LR} \tag{3.15}$$

$$\vec{F}_P = \vec{L}_P + \vec{D}_P \tag{3.16}$$

$$X_{para} = F_{P_x} \tag{3.17}$$

$$Z_{para} = F_{P_z} \tag{3.18}$$

Taking the moment balance at the hinge point:

$$\begin{aligned} \vec{M}_H = 0 &= \vec{M}_P + \vec{L} \times \vec{F}_P \\ &= \vec{M}_P - F_P l \hat{j} \end{aligned} \tag{3.19}$$

Where:

$$l = \frac{M_P}{F_P}$$

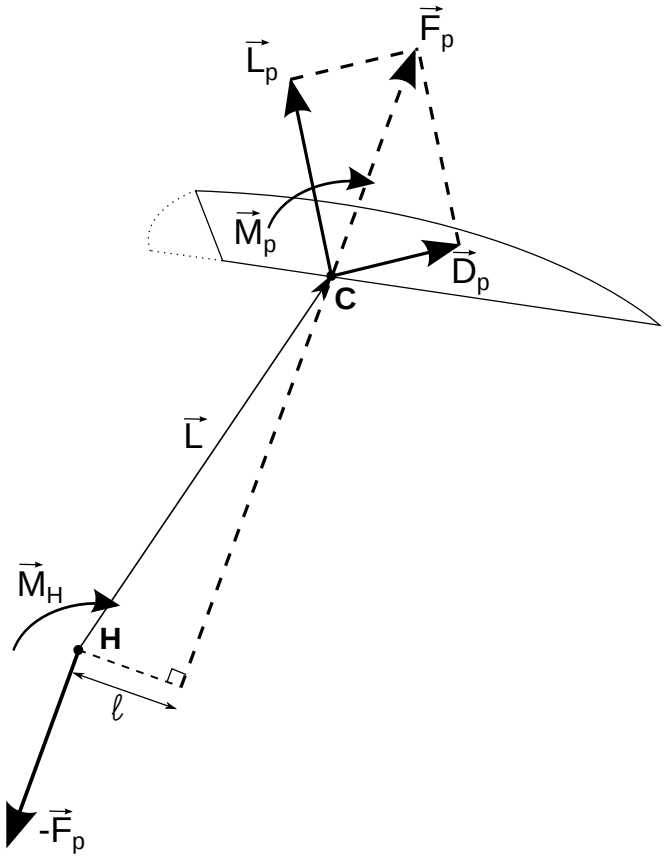

Figure 3.5: Resultant Loads

Figure 3.5 illustrates the resultant loads and moment balance acting on the canopy. The force $-\vec{F}_P$ will be added to the forces acting on the payload.

3.4 Expansion of the Aerodynamic Loads

For simplicity purposes, the expansion of the aerodynamic forces and moments in this section is done assuming still conditions, hence omitting the wind and gust components mentioned above. However, in the MATLAB environment, these components are included in the calculations.

From Equation 3.1:

$$\vec{V}_C = \vec{V}_H + \vec{\omega}_C \times \vec{L} = \vec{V}_H - \dot{\theta}_c L \hat{e}_{L1} \tag{3.20}$$

Now,

$$\hat{e}_{L1} = \begin{Bmatrix} \sin\theta_c \\ 0 \\ \cos\theta_c \end{Bmatrix} \tag{3.21}$$

$$\therefore \vec{V}_C = \begin{Bmatrix} V_{Hx} \\ 0 \\ V_{Hz} \end{Bmatrix} - \dot{\theta}_c L \begin{Bmatrix} \sin\theta_c \\ 0 \\ \cos\theta_c \end{Bmatrix} = \begin{Bmatrix} V_{Cx} \\ 0 \\ V_{Cz} \end{Bmatrix} \tag{3.22}$$

$$\begin{aligned} {V_C}^2 &= \vec{V}_C \cdot \vec{V}_C = V_{Cx}^2 + V_{Cz}^2 \\ &= (V_{Hx} - \dot{\theta}_c L \sin\theta_c)^2 + (V_{Hz} - \dot{\theta}_c L \cos\theta_c)^2 \\ &= {V_H}^2 - 2\dot{\theta}_c L(V_{Hx}\sin\theta_c + V_{Hz}\cos\theta_c) + {\dot{\theta}_c}^2 L^2 \end{aligned} \tag{3.23}$$

Also,

$$\hat{j} \times \vec{V}_C = \begin{Bmatrix} 0 \\ 1 \\ 0 \end{Bmatrix} \times \begin{Bmatrix} V_{Cx} \\ 0 \\ V_{Cz} \end{Bmatrix} = \begin{Bmatrix} V_{Cz} \\ 0 \\ -V_{Cx} \end{Bmatrix} \tag{3.24}$$

Now substituting the above into Equation 3.4 (with $\vec{V}_{CW} = \vec{V}_C$), the expanded expression for the resultant lift on the canopy is:

$$\begin{aligned} \therefore \vec{L}_C = \vec{L}_P = \frac{1}{2}\rho S C_L \{{V_H}^2 - 2\dot{\theta}_c L(V_{Hx}\sin\theta_c + V_{Hz}\cos\theta_c) + {\dot{\theta}_c}^2 L^2\}^{\frac{1}{2}} \\ \times \begin{Bmatrix} V_{Hz} - \dot{\theta}_c L\cos\theta_c \\ 0 \\ -V_{Hx} + \dot{\theta}_c L\sin\theta_c \end{Bmatrix} \end{aligned} \tag{3.25}$$

Similarly, Equations 3.5 and 3.6 can be expanded to the following expressions:

$$\begin{aligned} \vec{D}_C = -\frac{1}{2}\rho S C_D \{{V_H}^2 - 2\dot{\theta}_c L(V_{Hx}\sin\theta_c + V_{Hz}\cos\theta_c) + {\dot{\theta}_c}^2 L^2\}^{\frac{1}{2}} \\ \times \begin{Bmatrix} V_{Hx} - \dot{\theta}_c L\sin\theta_c \\ 0 \\ V_{Hz} - \dot{\theta}_c L\cos\theta_c \end{Bmatrix} \end{aligned} \tag{3.26}$$

$$\vec{M}_C = \frac{1}{2}\rho S c C_m \{{V_H}^2 - 2\dot{\theta_c} L(V_{Hx}\sin\theta_c + V_{Hz}\cos\theta_c) + {\dot{\theta_c}}^2 L^2\} \times \hat{j} \quad (3.27)$$

Again, ignoring V_w and V_g, Equations 3.10 and 3.12 can also be expanded to the following expressions:

$$\vec{D}_{LS} = -\frac{1}{2}\rho n d L C_{DL}(V_{Hx}\sin\theta_c + V_{Hz}\cos\theta_c)^2 \times \begin{Bmatrix} \sin\theta_c \\ 0 \\ \cos\theta_c \end{Bmatrix} \quad (3.28)$$

$$\vec{D}_{LR} = -\frac{1}{2}\rho n d L C_{DL}(\frac{4}{9}{\dot{\theta_c}}^2 L^2) \times \begin{Bmatrix} \sin\theta_c \\ 0 \\ \cos\theta_c \end{Bmatrix} \quad (3.29)$$

These expanded terms can then be substituted into Equation 3.19 in order to solve for $\dot{\theta_c}$. In doing so, the following expression can be obtained:

$$\begin{aligned} &|\vec{M}_H| = 0 \\ &= A + B\dot{\theta_c} + C{\dot{\theta_c}}^2 + D\sqrt{E + F\dot{\theta_c} + G{\dot{\theta_c}}^2} + H(I + J\dot{\theta_c})\sqrt{K + M\dot{\theta_c} + N{\dot{\theta_c}}^2} \end{aligned} \quad (3.30)$$

Where:

$$A = \frac{1}{2}\rho S c C_m {V_H}^2 + \frac{1}{4}\rho n d L^2 C_{DL}(V_{Hx}\sin\theta_c + V_{Hz}\cos\theta_c)^2$$

$$B = -\rho S c C_m L(V_{Hx}\sin\theta_c + V_{Hz}\cos\theta_c)$$

$$C = \frac{1}{2}\rho S c C_m L^2 + \frac{4}{27}\rho n d L^4 C_{DL}$$

$$D = -\frac{1}{2}\rho S C_L L(-V_{Hx}\cos\theta_c + V_{Hz}\sin\theta_c)$$

$$E = {V_H}^2 = K$$

$$F = -2L(V_{Hx}\sin\theta_c + V_{Hz}\cos\theta_c) = M$$

$$G = L^2 = N$$

$$H = \frac{1}{2}\rho S C_D$$

$$I = L(V_{Hz}\cos\theta_c + V_{Hx}\sin\theta_c)$$

$$J = -G$$

Despite Equation 3.30 being written in this "simplified" form, it is clear to see the complexity in trying to solve for $\dot{\theta_c}$ for a given θ_c. A root-finding technique, such as the *Bisection Method*, will need to be implemented in order to solve this expression.

3.5 Aerodynamics of Payload

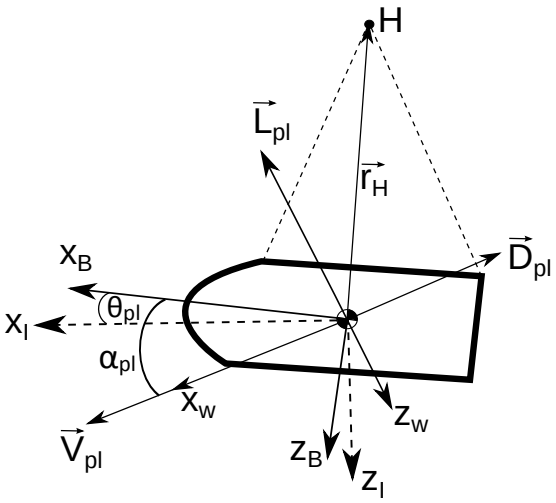

Figure 3.6: Aerodynamics of Payload

$$\textit{In body axes:} \quad \vec{V}_{pl} = \left\{ \begin{array}{c} U_{pl} \\ 0 \\ W_{pl} \end{array} \right\} \tag{3.31}$$

$$\alpha_{pl} = \tan^{-1} \frac{(W_{pl} - w_w - w_g)}{(U_{pl} - u_w - u_g)} \tag{3.32}$$

$$q_{pl} = \frac{1}{2}\rho(V_{pl} - V_w - V_g)^2 \tag{3.33}$$

$$L_{pl} = q_{pl} \times S_{refpl} \times C_{Lpl} \tag{3.34}$$

$$D_{pl} = q_{pl} \times S_{refpl} \times C_{Dpl} \tag{3.35}$$

$$M_{pl} = q_{pl} \times S_{refpl} \times X_{refpl} \times C_{mpl} \tag{3.36}$$

Where:

$$C_{Lpl} = C_{Lpl\alpha} \times \alpha_{pl}$$

$$C_{Dpl} = C_{D0pl} + \frac{{C_{Lpl}}^2}{\pi \mathcal{R}_{pl}}$$

$$C_{mpl} = C_{mpl\alpha} \times \alpha_{pl}$$

$$\begin{Bmatrix} X_{pay_B} \\ 0 \\ Z_{pay_B} \end{Bmatrix} = [T]^{BW} \begin{Bmatrix} -D_{pl} \\ 0 \\ -L_{pl} \end{Bmatrix} \tag{3.37}$$

Where $[T]^{BW}$ is the rotational matrix from wind axis to payload body axis (Refer to Fig. 3.6),

$$[T]^{BW} = \begin{bmatrix} \cos\alpha_{pl} & 0 & -\sin\alpha_{pl} \\ 0 & 1 & 0 \\ \sin\alpha_{pl} & 0 & \cos\alpha_{pl} \end{bmatrix} \tag{3.38}$$

The resultant parafoil force $\vec{F}_P$ acting at the hinge, as depicted in Fig. 3.5 causes a moment about the payload mass centre. As the parafoil and payload move, $\vec{F}_P$'s line of action might sometimes pass ahead of the payload mass centre, sometimes behind it and sometimes through it. So the moment caused by $\vec{F}_P$ will fluctuate between positive and negative values. The magnitude of this moment is determined as follows:

$$\vec{M}_R = \vec{r}_H \times \vec{F}_P \tag{3.39}$$

Where $\vec{r}_H$ is the vector from the payload mass centre to the hinge, as depicted in Fig. 3.6.

3.6 Parafoil Model for Longitudinal Motion

3.6.1 The State Vector

To simulate the longitudinal motion of the parafoil system, the following choice of state vector, SV, was made,

$$SV = [\theta_c, \phi_c, x_{pl}, z_{pl}, \theta_{pl}, U_{pl}, W_{pl}, \omega_{pl}, u_g, w_g]$$

Where:

θ_c = suspension line pitch angle (radians)
ϕ_c = suspension line angle of attack (radians)
x_{pl} = x position of payload (m)
z_{pl} = z position of payload (m)
θ_{pl} = payload pitch angle (radians)
U_{pl} = velocity component of payload along X_B (m/s)
W_{pl} = velocity component of payload along Z_B (m/s)
ω_{pl} = payload pitch angle rate (rad/s)

u_g = longitudinal turbulence velocity (m/s)
w_g = vertical turbulence velocity (m/s)

The parafoil and payload are said to be a *system of state ten*, because its state vector has 10 dimensions [22].

3.6.2 Calculation of the State Vector Derivatives

The longitudinal motion of the parafoil system was simulated by the calculation of the state derivatives, $\dot{SV}$. The estimation of these state derivatives will therefore be considered by solving the following 10 differential equations:

$$\textbf{1)}\ \dot{\theta_c} = \text{Solution of Equation 3.30} \tag{3.40}$$

$$\textbf{2)}\ \dot{\phi_c} = \dot{\theta_c} + \dot{\Gamma} \tag{3.41}$$

Where $\dot{\Gamma}$ is calculated as follows:

$$\vec{V}_H = \vec{V}_{pl} + \vec{\omega}_{pl} \times \vec{r}_H$$

$$\dot{\vec{V}}_H = \dot{\vec{V}}_{pl} + \dot{\vec{\omega}}_{pl} \times \vec{r}_H + \vec{\omega}_{pl} \times \dot{\vec{r}}_H$$

$$\Gamma = \tan^{-1} \frac{V_{Hz}}{V_{Hx}}$$

Γ is illustrated in Fig. 3.1. Now using the rules of differentiation,

$$\dot{\Gamma} = \frac{1}{1 + (\frac{V_{Hz}}{V_{Hx}})^2} \left(\frac{\dot{V_{Hz}} V_{Hx} - V_{Hz} \dot{V_{Hx}}}{V_{Hx}^2} \right)$$

$$\begin{Bmatrix} \dot{x_{pl}} \\ 0 \\ \dot{z_{pl}} \end{Bmatrix} = [T]^{IB} \begin{Bmatrix} U_{pl} \\ 0 \\ W_{pl} \end{Bmatrix}$$

Where $[T]^{IB}$ is the rotational matrix required to go to and from payload body axis and inertial axis (Refer to Fig. 3.6).

$$[T]^{IB} = \begin{bmatrix} \cos\theta_{pl} & 0 & \sin\theta_{pl} \\ 0 & 1 & 0 \\ -\sin\theta_{pl} & 0 & \cos\theta_{pl} \end{bmatrix}$$

$$\textbf{3)}\ \dot{x_{pl}} = U_{pl}\cos\theta_{pl} + W_{pl}\sin\theta_{pl} \tag{3.42}$$

$$\textbf{4)}\ \dot{z_{pl}} = -U_{pl}\sin\theta_{pl} + W_{pl}\cos\theta_{pl} \tag{3.43}$$

$$\textbf{5)}\ \dot{\theta_{pl}} = \omega_{pl} \tag{3.44}$$

$$\textbf{6)}\ \dot{U_{pl}} = \frac{X_B}{m_{pl}} - g\sin\theta_{pl} - \omega_{pl}W_{pl} \tag{3.45}$$

$$\textbf{7)}\ \dot{W_{pl}} = \frac{Z_B}{m_{pl}} + g\cos\theta_{pl} + \omega_{pl}U_{pl} \tag{3.46}$$

$$\textbf{8)}\ \dot{\omega_{pl}} = \frac{M_B}{I_{yy}} \tag{3.47}$$

$$\textbf{9)}\ \dot{u_g} = -\frac{U_{pl}}{L_u}u_g + \sigma_u\sqrt{\frac{2U_{pl}}{TL_u}}\eta_1 \tag{3.48}$$

$$\textbf{10)}\ \dot{w_g} = -\frac{W_{pl}}{L_w}w_g + \sigma_w\sqrt{\frac{2W_{pl}}{TL_w}}\eta_2 \tag{3.49}$$

Equations 3.48 and 3.49 are the differential equations for the continuous implementation of the Dryden turbulence model (See Section 2.1.5). Equations 3.45 - 3.47 are the equations of motion rearranged, as derived by Ashley [22]. These equations are valid in a body axis system, hence the X_B and Z_B force components act along the X_B and Z_B body axes, respectively, and:

$$X_B = X_{para_B} + X_{pay_B} \tag{3.50}$$

$$Z_B = Z_{para_B} + Z_{pay_B} \tag{3.51}$$

$$M_B = M_R + M_{pl} \tag{3.52}$$

It should be noted that the resultant X and Z forces acting on the parafoil required to go through the rotation from inertial axis to payload body axis $[T]^{BI}$ in order for Equations 3.45 - 3.47 to be valid.

$$[T]^{BI} = ([T]^{IB})^T$$

3.6.3 Matlab Implementation

A MATLAB model was developed based on the above formulation and the structure is shown in Fig. 3.7. Table 3.1 provides a brief description of the parafoil-payload model for longitudinal motion subroutines. Subroutine `ode45` is MATLAB's standard solver for ordinary differential equations (ODE's). This function implements an explicit *Runge-Kutta* method with a variable time step for efficient computation, to solve the differential equations numerically. `ode45` provides 4^{th} order, medium accuracy.

`fzero` is MATLAB's built-in root solver that finds the root of a non-linear function. It tries to find the point where the function equals zero and it was implemented in the model to solve for Equation 3.30.

Refer to Appendix A for the model parameters.

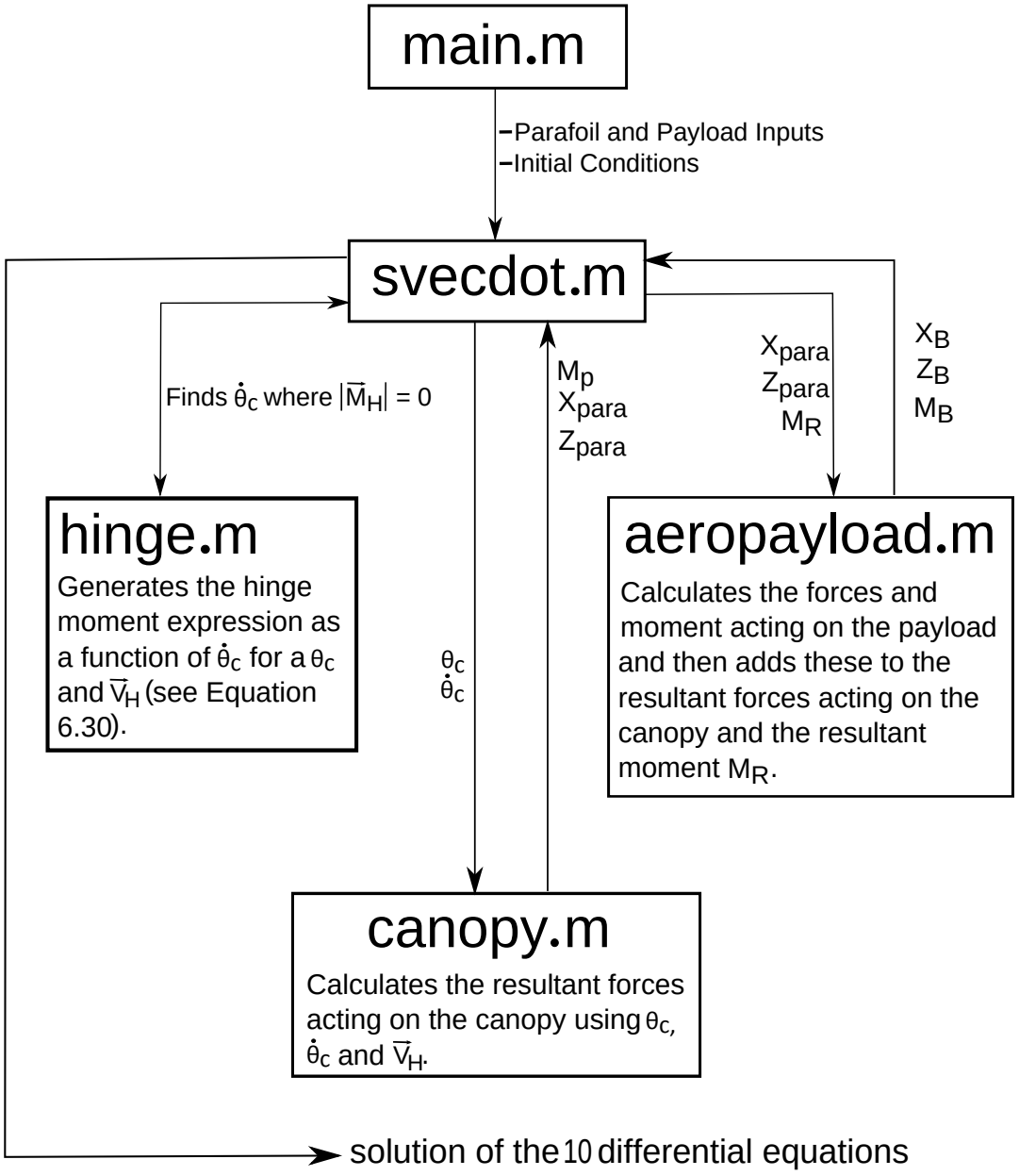

Figure 3.7: Structure of Model

Table 3.1: Description of Longitudinal Motion Parafoil Model Subroutines

No	Subroutine	Description
1	main.m	Specifies the parafoil and payload inputs. It also sets up the initial conditions for the state vector. Uses MATLAB's variable time step solver, `ode45`, to solve <`svecdot.m`>. It then plots the solutions of the differential equations.
2	svecdot.m	Sets up the components of the state vector. Calls <`hinge.m`> and uses MATLAB's built-in <`fzero.m`> function to find $\dot{\theta}_c$ where $\lvert\vec{M}_H\rvert = 0$ for a specific θ_c and $\vec{V}_H$. <`fzero.m`> is a root solver that combines bisection, secant and inverse quadratic interpolation. Then calls <`canopy.m`> to calculate the resultant X and Z forces acting on the canopy; and then calculates resultant moment ($\vec{M}_R$) due to the canopy force ($\vec{F}_P$). It also calls <`aeropayload.m`> to calculate the forces and moment acting on the payload, and then adds these to the resultant forces acting on the canopy and the resultant moment ($\vec{M}_R$). <`svecdot.m`> sets up the differential equations that need to be solved and outputs the derivatives of the state vector.
3	hinge.m	Generates the expression for the hinge moment, $\lvert\vec{M}_H\rvert$, as a function of $\dot{\theta}_c$ for a specific θ_c and $\vec{V}_H$ (See Equation 3.30).
4	canopy.m	Calculates the resultant forces acting on the parafoil using the $\dot{\theta}_c$ that <`fzero.m`> found in <`svecdot.m`>, for a specific θ_c and $\vec{V}_H$.
5	aeropayload.m	Calculates the forces and moment acting on the payload, and then combines the resultant forces acting on the canopy and the resultant moment due to the canopy forces to get the total forces and the total pitching moment needed for the differential equations 3.45 - 3.47.

Chapter 4

Experimental Details and Methodology

4.1 Setting Up the Testing Matrix

It was decided that only two control factors be adjusted in order to determine the optimum glide slope and trim setting for the parafoil. The two factors that will contribute most significantly to glide slope are trim angle and plumb line length. Each control factor will have three levels, a low level, an intermediate level and a high level. The control factors used and their levels are given in Table 4.1, where the parafoil canopy span (b) is 3.950 metres.

Table 4.1: Control Factors and Levels

Control Factor	**Low Level (-1)**	**Intermediate Level (0)**	**High Level (+1)**
A:Trim Angle (°)	9	11	13
B:Plumb Line Length (m)	3.555 (0.9×b)	3.950 (1×b)	4.345 (1.1×b)

Since two factors at three levels each are to be investigated, a three-level orthogonal array will be implemented. The $L9(3^4)$ design described in Chapter 4 will be used, but since only two factors are being considered and not four, only the first two columns of the orthogonal array are needed. See Table 4.2.

Table 4.2: $L9(3^2)$ Orthogonal Array Design

Run	1	2	3	4
1	−1	−1	−1	−1
2	−1	0	0	0
3	−1	+1	+1	+1
4	0	−1	0	+1
5	0	0	+1	−1
6	0	+1	−1	0
7	+1	−1	+1	0
8	+1	0	−1	+1
9	+1	+1	0	−1

The proposed testing matrix is therefore given by Table 4.3. In total nine experimental runs will need to be conducted, with space for *replication*. The measured response for these nine combinations is the glide slope or glide angle in steady flight. The nine runs are to be conducted in random order for the purpose of *randomisation*. The order of experimentation is randomised to average out the effects of variables that cannot be controlled, such as wind speed and wind direction in this case.

Table 4.3: Proposed Testing Matrix with 3 Replicates

	Factor		**Response (Glide Slope)**		
Run	**A**	**B**	**Replicate 1**	**Replicate 2**	**Replicate 3**
1	−1	−1			
2	−1	0			
3	−1	+1			
4	0	−1			
5	0	0			
6	0	+1			
7	+1	−1			
8	+1	0			
9	+1	+1			

4.2 Testing Rig and Apparatus

The unique catapult for launching parafoils, as depicted in Fig. 4.1, is designed to launch parafoils from a hilltop or cliff. The launcher comprises of the trailer, the linear track, the arm structure, the linear accelerator and the carriage. Refer to Chapter 5. There is also a speed trap on the linear track to measure the launch speed.

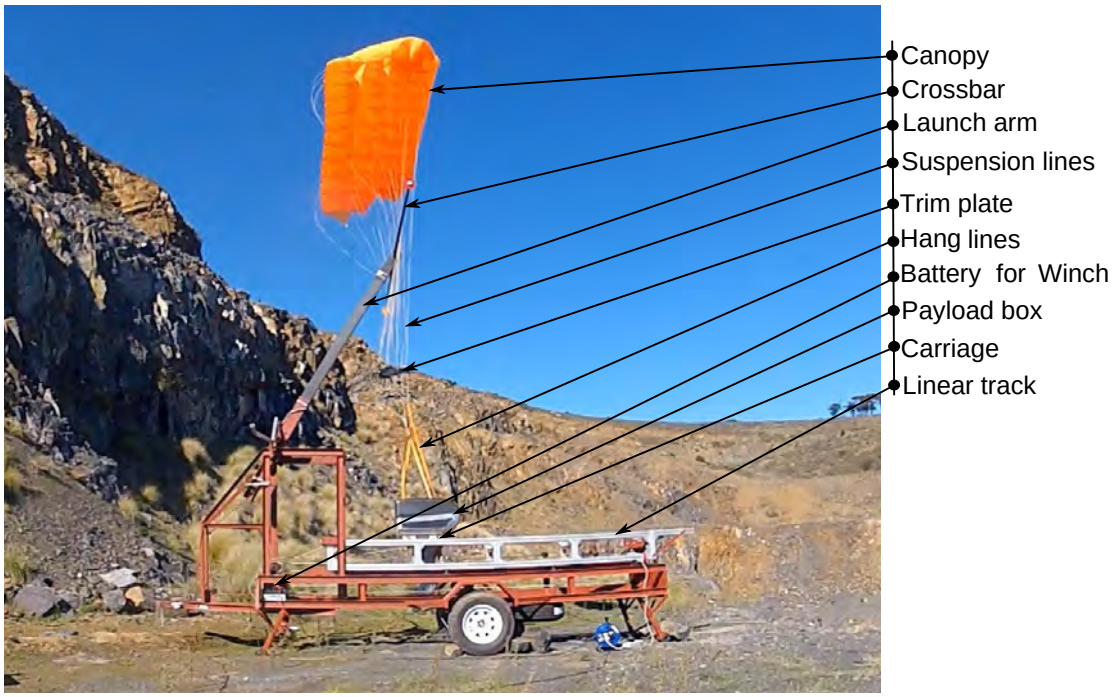

Figure 4.1: Parafoil Launcher

The parafoil used for testing, as depicted in Fig. 4.2, has the following dimensions:

- Aspect Ratio ($\mathcal{R}_c$) = 2.6
- Canopy chord length (c) = 1.53 m
- Canopy span length (b) = 3.95 m
- Canopy planform area (S) = 6.03 m^2

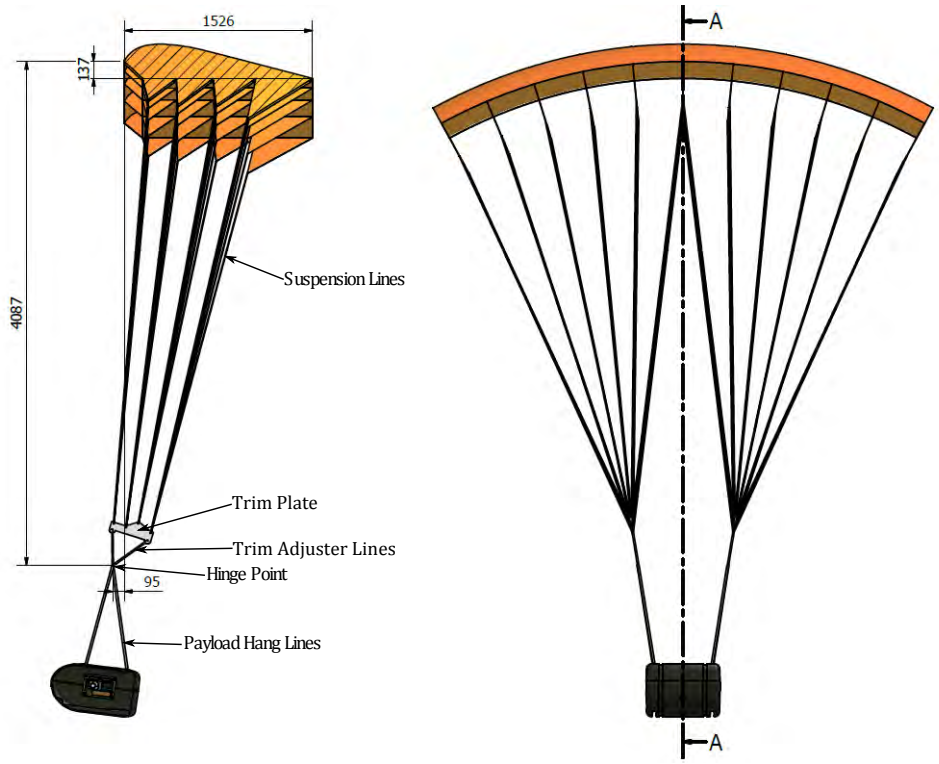

Figure 4.2: Parafoil

The plumb line length and the trim angle are the two parameters that will be varied during the flight tests, as discussed in the previous section. The trim plates have been designed to easily permit for variation of these settings. Figure 4.3 illustrates the two symmetric trim plates that are made from aluminium alloy, because of its high strength-to-weight ratio. The unique shape of the trim plates allows the suspension lines to be conveniently grouped and attached to the trim plate at the top four holes via shackles. The bottom two holes allow for shackles with "trim adjuster lines" to be attached which extend to the hinge point, and the payload is suspended by hang lines from this point (Refer to Fig. 4.2 and 4.3). The concept of a trim plate for the variation of lines and trim angle is not a novel one. In 1989, Brown [13] constructed a trim bar consisting of a bar with attached turn-buckles capable of conveniently adjusting either trim angle or any line group separately. Brown's adjustable trim bar is illustrated in Fig. 4.4.

Figure 4.3: Trim Plates

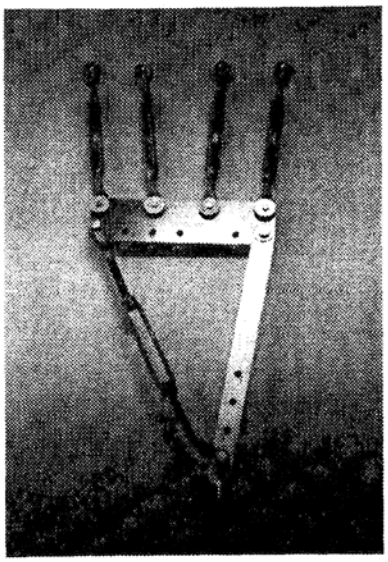

Figure 4.4: Brown's Adjustable Trim Bar [13]

The trim plates thus ensure that the length of the suspension lines do not need to be varied. This is particularly useful as there are 48 suspension lines in total. Having to vary the length of each suspension line would prove to be quite a tedious task, and therefore the turn around time between flight tests would be long. The plumb line length is then approximately equivalent to the suspension line length plus the trim adjuster line length. By altering the length of the adjuster lines, the required two factors, plumb line length and trim angle, can be changed accordingly to the testing matrix. In Fig. 4.2, the plumb line length is equal to the span, i.e. 1×b (4087 - 137 = 3950 mm).

The payload box, depicted in Fig. 4.5, was designed to enclose the electronic steering unit described in Chapter 5. For the purpose of testing for the optimum glide slope and trim setting, brake deflections will not be necessary. Therefore, the steering unit will be replaced with dummy masses. The payload box is manufactured from composite materials (glass fibre, carbon fibre, kevlar and closed-cell sandwich-structured foam) for its lightweight and durability properties. Inside the payload box there is polyethylene foam that snugly accommodates the steering unit or dummy masses. The foam acts like a shock absorber for the payload box upon making impact with the ground. The payload box can also accommodate two GoPro cameras, one forward facing and one upward facing. Refer to Fig. 2.26 to see the layout inside the payload box.

Figure 4.5: Payload Box

Apart from enclosing the dummy masses, the payload box also needs to include the most integral component of the testing apparatus, the inertial measurement unit (IMU) and estimator. The IMU is an electronic device that measures and reports on the payload's velocity, orientation, and gravitational forces, using a combination of accelerometers and gyroscopes, sometimes also magnetometers. In conjunction with the IMU, there is an on-board global positioning system (GPS). These on-board electronics are powered by a single 12 volt direct current, 2 ampere hours battery. There is also a secondary IMU attached to the parafoil's canopy and connected to the payload box via a ribbon cable. Figure 4.6, courtesy of Gideon van der Kolf, illustrates the extended Kalman filter implemented for the state estimation, and Table 4.4 summarises the parameters measured by the payload and canopy unit.

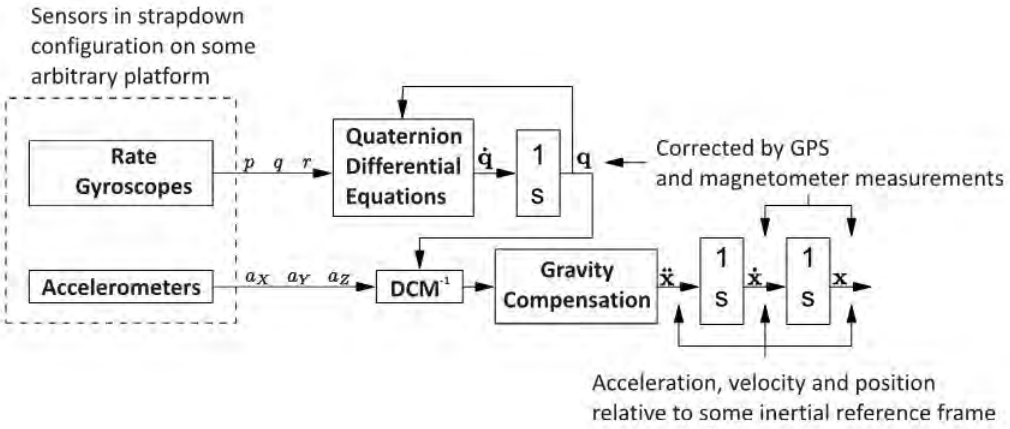

Figure 4.6: Estimator Schematic

Table 4.4: Parameters Measured

Parameter	**Unit**
Payload Gyroscope X, Y, Z	$^\circ/s$
Payload Accelerometer X, Y, Z	m/s^2
Canopy Gyroscope X, Y, Z	$^\circ/s$
Canopy Accelerometer X, Y, Z	m/s^2
Magnetometer X, Y, Z	$Gauss$
GPS Latitude	$^\circ$
GPS Longitude	$^\circ$
GPS Altitude	m
GPS Heading	$^\circ$
GPS North, East, Down Velocity	m/s
Estimator North, East, Down Displacement	m
Estimator North, East, Down Velocity	m/s
Estimator Roll, Pitch, Yaw Angle	$^\circ$

The raw IMU and estimator data (see Table 4.4) are relayed from the parafoil and payload system to the ground through a 2.4 GHz radio link to the launch station computer/laptop. This data is received by the Stellenbosch University "FLIGHT Ground station" software that displays and manages the incoming data flow. Refer to Appendix B for information about the parafoil avionics ground station software, and instructions for using this

software. The data can be logged on a micro SD card and saved to the laptop for later analysis. During flight, the ground station and payload communicate via two radio modems, one radio modem at the the ground station and one radio modem placed inside the payload box. The radio modem inside the payload box is also powered by a single 12 V battery and the ground station's radio modem is powered by a 12 V power supply. Each radio modem has a dipole antenna, and the system is capable of achieving long range line-of-sight communications up to 1km.

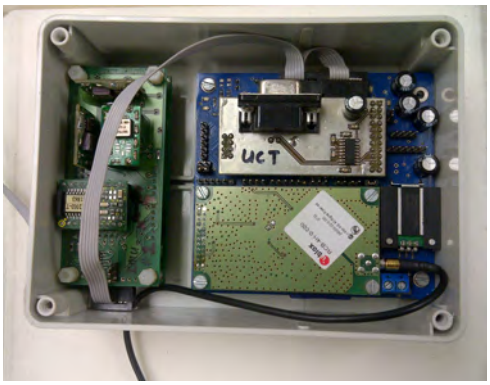

Figure 4.7: IMU, Estimator and GPS

Figure 4.8: 12 V DC Battery

Figure 4.9: 2.4 GHz Radio Modem

It is essential that the mass of the components inside the payload box is evenly distributed, to ensure that the CG of the payload box remains in the middle. Any offset in the payload's CG can cause unwanted lateral and

longitudinal disturbances during flight. A quick test to check the payload box's centre of gravity was conducted. This entailed suspending the payload box from a bar using two spring balances to measure its weight. Figure 4.10 illustrates the set-up for this test.

Figure 4.10: Checking Payload Box's Centre of Gravity

Some additional equipment required for flight testing include: a generator, a weather station, beacons and cameras. The generator is used to power the ground station laptop and the power supply, as testing can go on for several hours provided the weather is good. In order to monitor the weather during the flight tests, a weather station measures the wind speed, wind direction, temperature and air pressure. The beacons are used to mark the landing points after each flight test, so that differential GPS measurements can be taken by a surveyor. Apart from the on-board GoPro cameras, external cameras record video footage of the flight tests.

4.3 Preparation Before a Flight Test

The success of inferring parafoil glide slope by extending unsettled trajectory measurements via simulation relies substantially on obtaining accurate data. For this reason, the parafoil data acquisition system, comprising of two IMU's, an estimator and a GPS, required testing. Although not one of the primary objectives of this research, as fellow research colleague Gideon van der Kolf from the University of Stellenbosch had already demonstrated that the avionics equipment worked. Tests were conducted on UCT's rugby fields to verify that data was being sent from the avionics to Stellenbosch University's "FLIGHT Ground station" application residing on the laptop (see Fig. 4.11). The tests demonstrated that data could be received and logged

over 3 rugby fields (a range of approximately 300 m) and it was deemed that the data acquisition system was adequate for further flight testing, provided line of sight between the antennas was not obscured. The intended use of the data acquisition system was to provide relatively accurate trajectory measurements (mainly velocities and positions) so that glide slope could be inferred.

Figure 4.11: Rugby Field Tests

In preparation before any flight testing, the following steps must be completed:

- All batteries must be charged before departure to the testing site. The 12V, 2Ah batteries must be trickle charged using a power supply. Refer to Appendix C for the procedure to trickle charge the batteries. Camera and laptop batteries must be charged before departure. There should be sufficient batteries for the operation of the weather station. The winch battery on the parafoil launcher must be checked and charged if necessary.

- All avionics must be checked and tested prior to testing. This entails checking that all components are in working order. These components include: the IMU's, the estimator, the GPS, the radio modems and the antennas.

- The pulley and spring system of the parafoil launcher should be inspected on a regular basis, and maintenance of this system should be conducted if necessary.

- Manufacture the trim adjuster lines for the different experimental combinations and have them marked accordingly.

- Inspect the trim plates for any defects or cracks.

- Verify that there is no fraying of the suspension lines and payload hang lines. If any lines are frayed or damaged, replace them.

- Check for any tears on the parafoil canopy. The tears will need to be repaired before any flight tests can be conducted.

- Quick-release shackles and lines must all be tested at the beginning of a flight testing session. If any faulty shackles are discovered, they must be replaced immediately.

- The ground station software requires that the data files (.cfg) that are used by the ground station application be in the C:\ drive. Ensure that this is the case on the ground station laptop. This directory is also where the ground station will log session data.

4.4 Flight Test Procedure

The flight test procedure can be summarised as follows:

1. On arrival at the testing site, set up the weather station. Ensure that the thermometer is placed in the shade, and that the wind vane and anemometer stand is pointing in the northerly direction.

2. Set up the ground station and connect the ground station antenna to power and the laptop. Ensure that the ground station antenna will have line of sight of the payload box antenna during flight.

Figure 4.12: Set Up of the Parafoil Launcher

3. Set up the parafoil launcher on top of a hill or cliff, pointing in the desired direction of launch and ensuring the trailer is level. If necessary, adjust support legs of the trailer. See Fig. 4.12 and Fig. 4.13.

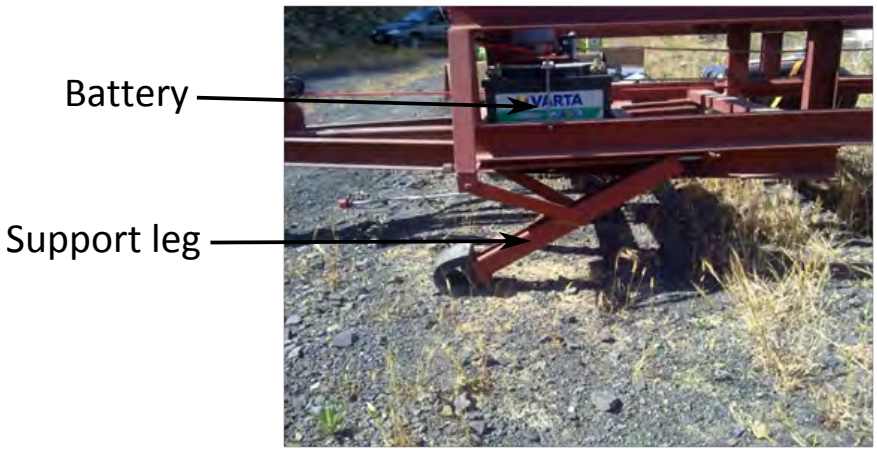

Figure 4.13: Support Legs of Trailer

4. Plug in speed trap and connect battery to winch.

Figure 4.14: Speed Trap

Figure 4.15: Winch

5. Unwind the winch while pulling the carriage backwards until the carriage is in the backward position. Make sure the carriage is running smoothly on the track (as illustrated in Fig. 4.16) and that the brake arrestor is set to the correct length.

Figure 4.16: Carriage Running Smoothly on Track

6. Now that the carriage is in the backward position, engage its release shackle that will be triggered by the arm. Refer to Fig. 4.17.

7. Check that the centre arm rotates smoothly and store the brake arrestor rope below quick-release shackle and clear from all other ropes. Refer to Fig. 4.17.

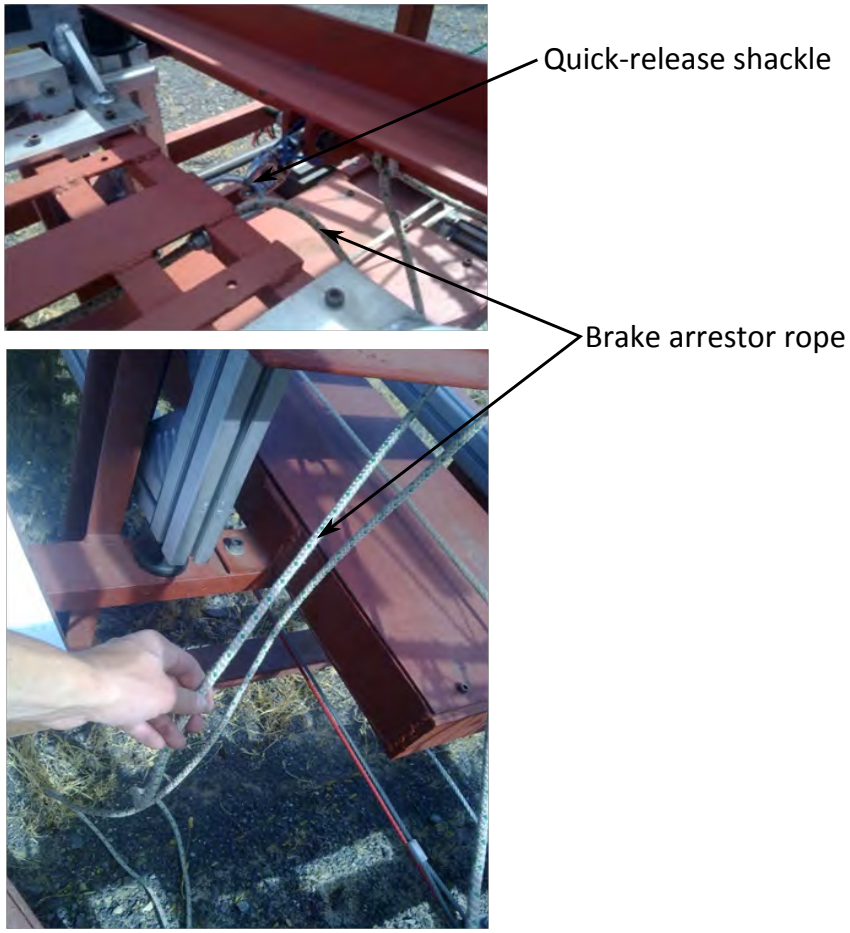

Figure 4.17: Brake Arrestor Rope

8. Lock the catapult/centre arm to its quick release shackle and ensure that the catapult arm quick-release line easily releases arm before launch. Also ensure that unintended release does not occur.

Figure 4.18: Catapult Arm Quick-release Shackle

9. Remove slack from the spring system, if necessary, but do not add any tension.

10. Position and bolt spreader bar in place as illustrated in Fig. 4.19.

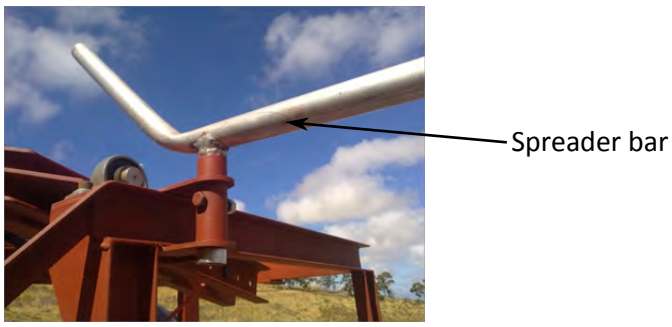

Figure 4.19: Spreader Bar

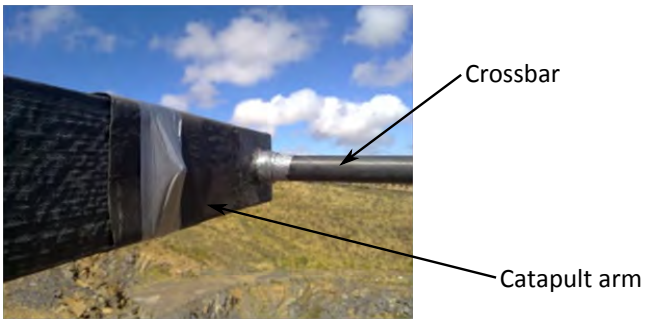

Figure 4.20: Crossbar

11. Insert crossbar into arm, ensuring no tacky tape or edges can snag the suspension lines. Refer to Fig. 4.20.

12. Apply slight tension to the system and check all quick-release shackles are secure.

13. Place the payload box on the carriage and verify that it is properly seated in the slots. Check that the hooks are free to release, not bent or too tight a fit in the slots. See Fig. 4.21.

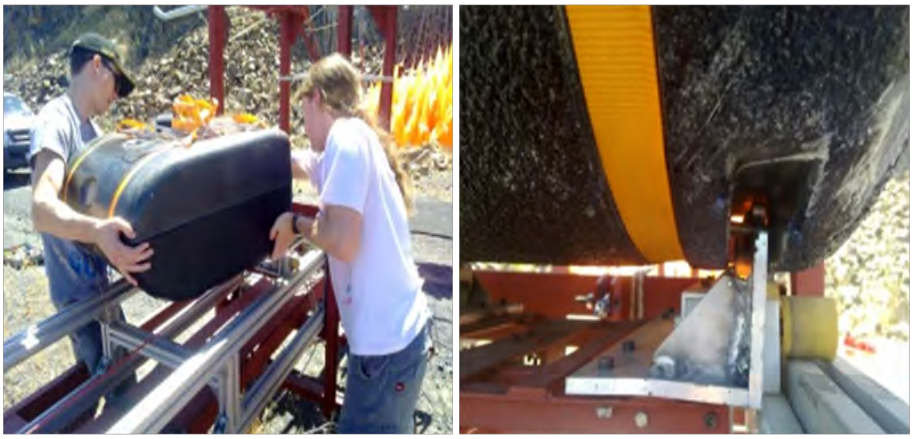

Figure 4.21: Payload Box Seated on Carriage

14. Ensure that the suspension lines are already grouped and attached to the trim plates at the top four holes via shackles.

15. Attach the "trim adjuster lines", for a specific trim setting, to the bottom two holes of the trim plate. Check that the front and back "trim adjuster lines" are correct on either side.

16. Drape the parafoil's canopy and lines over the spreader bar and crossbar, and connect the parafoil to the payload box hang lines at the hinge point. Verify that the hang lines are safely positioned around the turret. See Fig. 4.22.

17. Attach IMU2 (the canopy's IMU) to the parafoil's canopy and the payload box, ensuring that the ribbon cable goes over the turret, spreader bar and crossbar. Refer to Fig. 4.23.

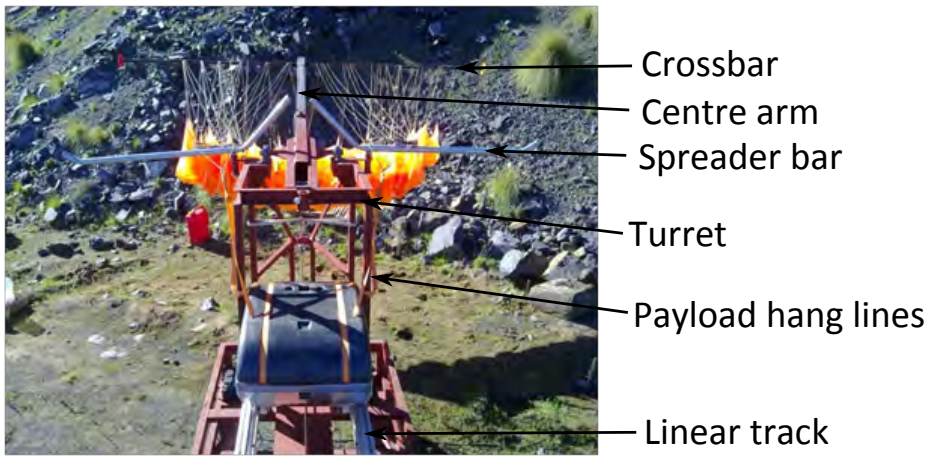

Figure 4.22: Draping of the Parafoil's Canopy

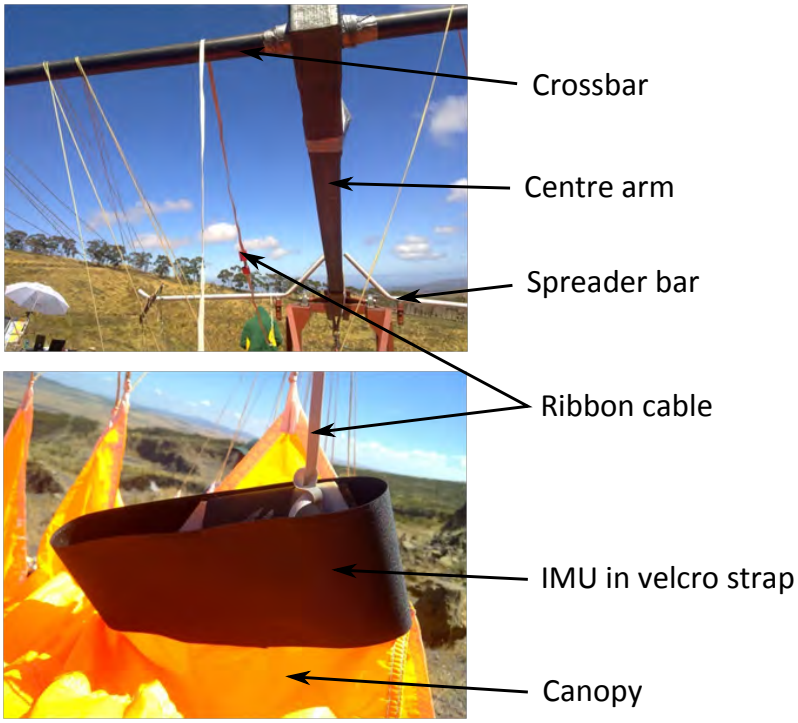

Figure 4.23: Attaching the Canopy's IMU

18. Separate suspension lines away from the centre arm and group lines by flare rows. See Fig. 4.24.

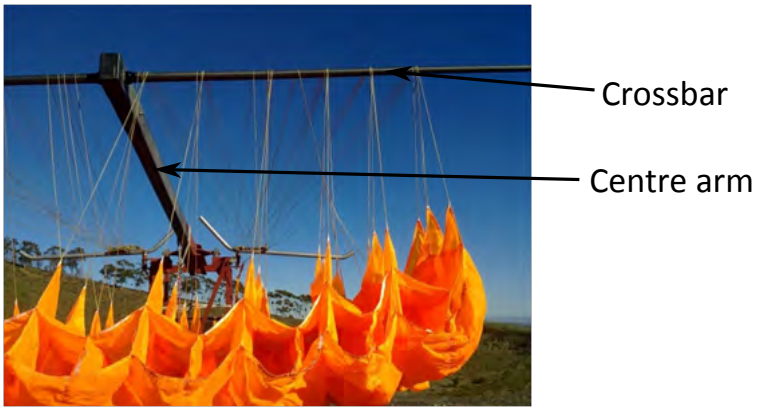

Figure 4.24: Separation of Suspension Lines

19. Position the trim plates with the thin section pointed away from the trailer, ensuring that lines are free from snagging and are free to lift off the spreader bar during launch, as illustrated in Fig. 4.25.

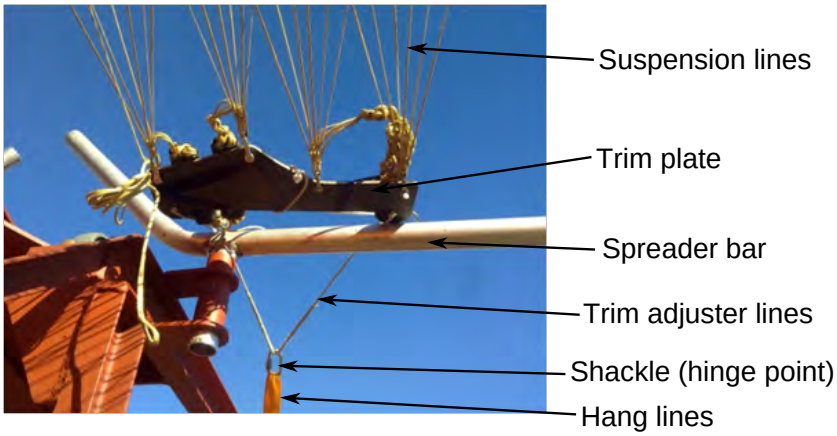

Figure 4.25: Positioning of Trim Plates

20. Position catapult elastic trigger line just above high tension system line. See Fig. 4.26.

21. Ensure the payload trigger line is securely attached to the elastic trigger line and carriage quick-release shackle, and that there is no slack. See Fig. 4.26.

22. Ensure that the carriage's brake arrestor rope is free from snagging.

23. Attach a trigger cord to the catapult arm quick-release line. See Fig.4.26.

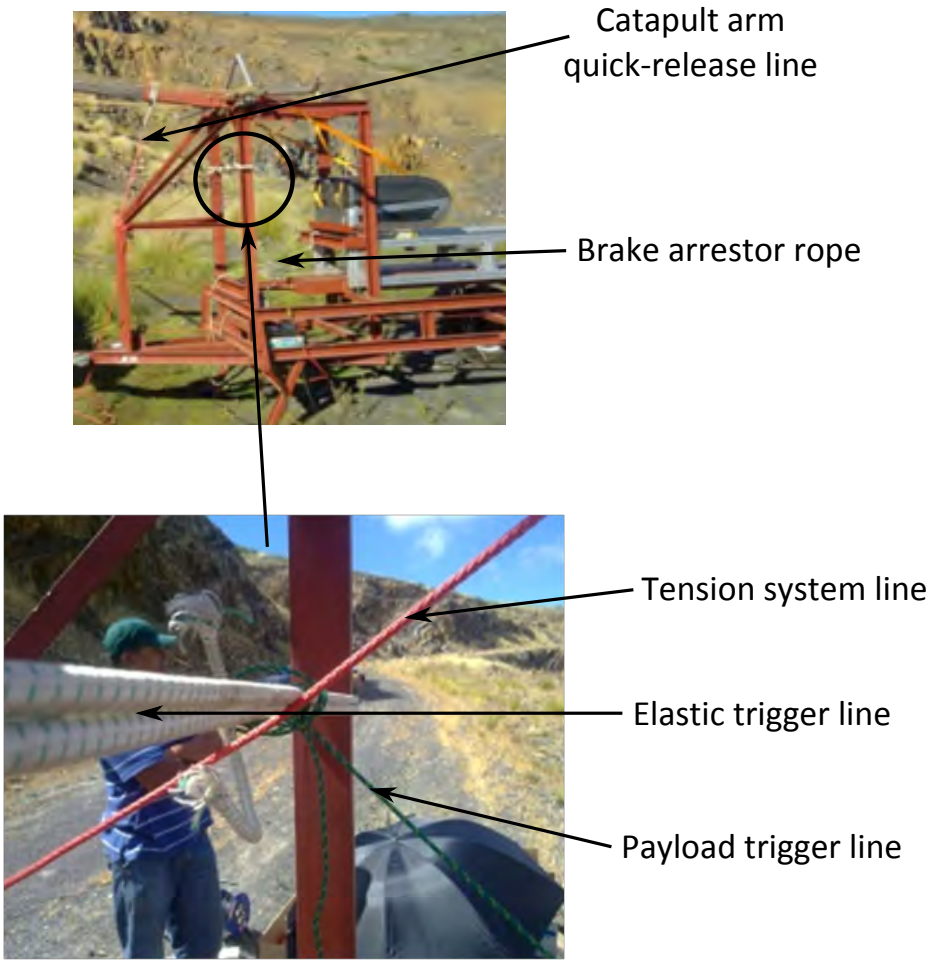

Figure 4.26: Trigger Lines and Quick-Release Lines

24. Switch on the avionics and any on-board cameras. Run the ground station application and verify that the ground station is communicating to both IMU's by selecting the correct COM port that the radio frequency (RF) modem is connected to (IMU data should be streaming to the ground station). Check that there are no SD card errors. Format the SD card if necessary. Wait a few minutes after power-on, before launch, for GPS lock. Initialise and start the estimator.

25. Tension the spring and pulling system by winding up the winch. Ensure all individuals present are wearing the necessary personal protective equipment (PPE) when tensioning the system.

26. Signal any external camera operators to start recording and start logging data using the ground station application. Record the log file number along with the ground station session number (displayed in the titlebar of the application) somewhere with the current flight test number, for future reference.

27. Await still wind conditions before launching.

28. Trigger person counts down and launches the parafoil-payload system by releasing the trigger cord on the catapult arm.

29. Immediately after touchdown, record the time of launch, temperature, wind speed, wind direction, air pressure and launch speed; somewhere with the current flight test number, for future reference.

30. After the system has landed, switch off the IMU and any on-board cameras, and mark the landing site with a beacon.

31. Recover the system and return to the launching site. Here the IMU data stored on the SD card can be collected and saved onto a laptop.

32. Repeat steps 11–30 with new "trim adjuster lines" (see step 13), corresponding to the trim setting combinations in the testing matrix.

Figure 4.27: Completed Set Up of the Parafoil Launcher

Chapter 5

Results and Discussion

5.1 Preliminary Test Results

Flight tests were conducted in July 2013, however due some technical issues, IMU data was only logged for a single flight corresponding to a trim angle of 9° and a plumb line length of $1 \times b$. For all the tests conducted, a surveyor accurately measured the landing coordinates after each flight. During those flight tests, it was discovered that a trim angle setting of 7° was not going to work, because the system did not clear the ledge below the launching point. This led to the levels of trim angle being changed for future flight tests. This section documents the preliminary flight tests and a brief analysis on those tests is presented.

Table 5.1 illustrates the control factors and levels used in the preliminary flight tests. The testing matrix adopted was the same as Table 4.3, but due to the lack of IMU data, the measured response was taken to be the horizontal distance travelled by the parafoil-payload system and not glide slope. Table 5.2 represents the data collected by the surveyor.

Table 5.1: Control Factors and Levels for Preliminary Tests

Control Factor	**Low Level (-1)**	**Intermediate Level (0)**	**High Level (+1)**
A:Trim Angle (°)	7	9	11
B:Plumb Line Length (m)	3.555 (0.9×b)	3.950 (1×b)	4.345 (1.1×b)

Table 5.2: Coordinates Recorded During Preliminary Testing

	Run #	**y(easting) (m)**	**x(northing) (m)**	**z (m)**
S1		35373.95	3739605.35	314.34
S2		35373.95	3739605.36	314.33
S3		35373.95	3739605.35	314.34
Savg		**35373.95**	**3739605.36**	**314.34**
L1	5	35511.06	3739604.93	260.62
L2	2	35401.58	3739614.07	291.55
L3	6	35485.95	3739597.81	260.75
L4	7	35523.07	3739583.86	260.38
L5	8	35494.77	3739540.41	260.81
L6	4	35502.42	3739540.95	260.81
L7	9	35483.54	3739622.23	260.75
L8	7	crash	crash	crash
L9	7	35496.00	3739539.22	260.85
L10	7	35435.19	3739488.85	260.59
L11	7	35496.19	3739533.66	260.95
L12	3	35399.22	3739598.20	291.04

Where:

S = Starting point

L = Launch landing point

Figure 5.1 is an aerial shot of the quarry indicating the approximate landing points after each flight test. It is evident that the parafoil-payload system did not always travel in a straight path, as cross-winds most likely caused the system to drift left or right after launch. L2 and L12 correspond to run numbers 2 and 3 respectively, that both had a trim angle setting of 7°. These two flight tests landed on the ledge below the launching point and it was deduced that this trim angle setting needed to be changed for future flights. L8, indicated in red on Fig. 5.1, is an approximate crash landing point. This resulted from incorrectly rigging the parafoil, where the front and back trim adjuster lines were accidentally swapped around.

As mentioned before, IMU data was only logged for a single flight test, that was for L1 corresponding to Run 5. Therefore, the measured response for

these preliminary flight tests was horizontal distance instead of glide slope, using the accurate coordinates recorded by the surveyor.

Figure 5.1: View of Quarry Indicating the Landing Points
Image courtesy of Google Earth

Calculating the Horizontal Distance for each Flight

The y, x and z-distances were calculated by subtracting the average start points (S_{avg}) from each landing points. For example for L1:

$$\text{y-distance} = 35511.06 - 35373.95 = 137.11\ m$$

$$\text{x-distance} = 3739604.93 - 3739605.36 = -0.43\ m$$

$$\text{z-distance} = 260.62 - 314.34 = -53.72\ m$$

The total horizontal distance for each flight is calculated by using simple Pythagoras. For L1:

$$\begin{aligned} d &= \sqrt{x^2 + y^2} \\ &= \sqrt{(-0.43)^2 + (137.11)^2} = 137.11\ m \end{aligned}$$

The same calculations were done for each of the flights and the results were tabulated in Table 5.3 below. All distances are in metres.

Table 5.3: Calculated Horizontal Distances

Launch	**Run #**	**y-distance**	**x-distance**	**z-distance**	**Horizontal dist.**
L1	5	137.11	-0.43	-53.72	137.11
L2	2	27.63	8.72	-22.79	28.97 (68.12*)
L3	6	111.99	-7.55	-53.59	112.25
L4	7	149.12	-21.49	-53.96	150.66
L5	8	120.82	-64.95	-53.53	137.17
L6	4	128.47	-64.41	-53.53	143.71
L7	9	109.59	16.87	-53.59	110.88
L8	7	crash	crash	crash	crash
L9	7	122.05	-66.13	-53.48	138.82
L10	7	61.24	-116.50	-53.75	131.62
L11	7	122.24	-71.69	-53.38	141.71
L12	3	25.27	-7.16	-23.30	26.27 (60.43*)

For L2 and L12 (trim angle setting of 7°) which landed on the ledge below, the measured landing point was extrapolated to a "predicted" impact point lying on the same horizontal level as the others. The values for the horizontal distances of L2 and L12 are denoted with an * in Table 5.3.

Table 5.4 illustrates the "predicted" impact points for L2 and L12. The mean z-coordinate for the other flights (z*) was used as the reference point for the linear extrapolation of x and y. The equation used for the linear extrapolation was:

$$y^* = y_{k-1} + \frac{z^* - z_{k-1}}{z_k - z_{k-1}}(y_k - y_{k-1}) \tag{5.1}$$

Where the data points nearest z* to be extrapolated are (z_{k-1}, y_{k-1}) and (z_k, y_k). For example, for L2, Run 2:

$$\begin{aligned} y^* &= 35373.95 + \frac{(260.74 - 314.34)}{(291.55 - 314.34)}(35401.58 - 35373.95) \\ &= 35438.91\ m \end{aligned}$$

Similarly done for x* and for L12, Run 3. The results are tabulated in Table 5.4.

Table 5.4: Predicted Impact Points

Launch	y*	x*	z*	y-dist*	x-dist*	z-dist*
L2	35438.91	3739625.85	260.74	64.96	20.50	-53.60
L12	35432.10	3739588.89	260.74	58.15	-16.46	-53.60

Design of Experiments Analysis

Referring back to Table 4.3 and changing the measured response to horizontal distance for the data collected, the testing matrix can be illustrated as follows:

Table 5.5: Testing Matrix for the Preliminary Tests

	Factor		Response (Horizontal Distance(m))			
Run	**A**	**B**	**1**	**2**	**3**	**4**
1	7(−1)	3.555(−1)	75.80**			
2	7(−1)	3.950(0)	68.12*			
3	7(−1)	4.345(+1)	60.43*			
4	9(0)	3.555(−1)	143.71			
5	9(0)	3.950(0)	137.11			
6	9(0)	4.345(+1)	112.25			
7	11(+1)	3.555(−1)	150.66	138.82	141.71	131.62
8	11(+1)	3.950(0)	137.17			
9	11(+1)	4.345(+1)	110.88			

As Run 1 (trim angle = 7° and plumb line length = $0.9 \times b$) was never conducted, the horizontal distance was estimated to be 75.80 m and hence the ** in Table 5.5. In order to get that value from the other two predicted points for trim angle 7°, a straight line with the same gradient was projected (See Fig. 5.2), in an attempt to follow the trend of the other two settings of 9° and 11°, so that the L9 array could be completed.

For the repeats of Run 7 (highlighted in green):

Mean = 140.70 m

Standard deviation = 7.88 m

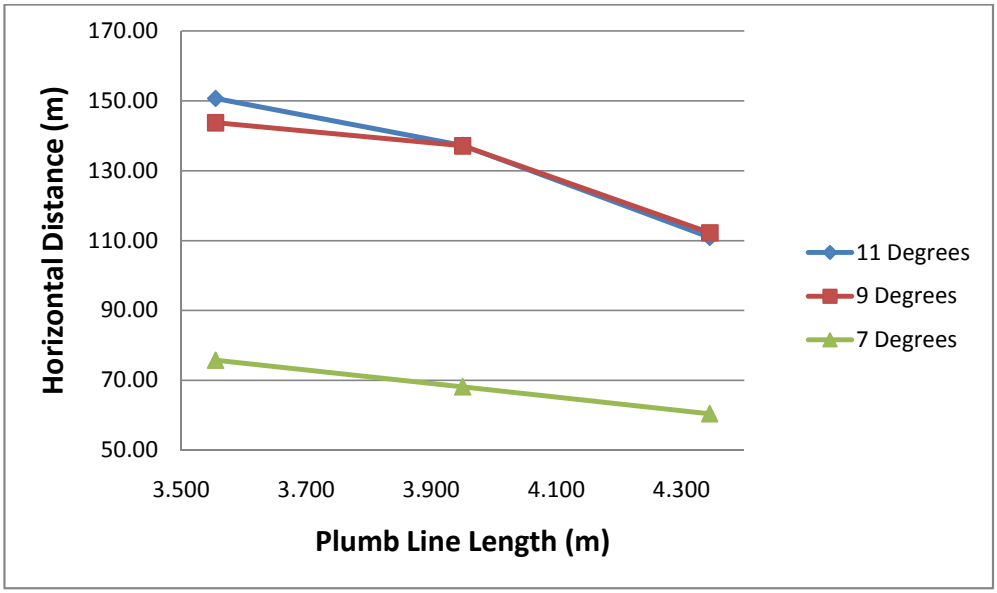

Figure 5.2: Horizontal Distance vs. Plumb Line Length

Table 5.6: Factor and Interaction Effects on Horizontal Distance

Factor	**Level**	**Average Distance (m)**
A (Trim Angle)	-1	64.27
	0	131.02
	$+1$	132.90
B (Line Length)	-1	147.19
	0	114.13
	$+1$	94.52
A $\times$ B	-1	105.55
	$+1$	93.34

The highlighted yellow block in Table 5.6 is the average horizontal distance travelled for the flights with the intermediate level trim angle of 9° (Also see Table 5.5). The other average distances were determined similarly, according to the factor and level. The blue and red highlighted blocks are the average distances for the interaction of factor A and B. Refer to Table 5.5 where it can be seen if A $\times$ B $= -1$ or $+1$.

Now, to investigate the contribution the factor effects have on the measured response (horizontal distance), the following calculations were required:

Main effect of Trim Angle (A) on Horizontal Distance Travelled:

The average distance was calculated when A is "−1" and when A is "+1" (refer to Table 5.6), and the average distance variation from the low to high level of trim angle was determined as follows:

$$\frac{132.90 - 64.27}{1 - (-1)} = 34.31\ m$$

Main effect of Plumb Line Length (B) on Horizontal Distance Travelled:

The average distance of B (-1) was 147.19 m and of B (+1) was 94.52 m (refer to Table 5.6). Therefore, the distance variation was:

$$\frac{94.52 - 147.19}{1 - (-1)} = -26.33\ m$$

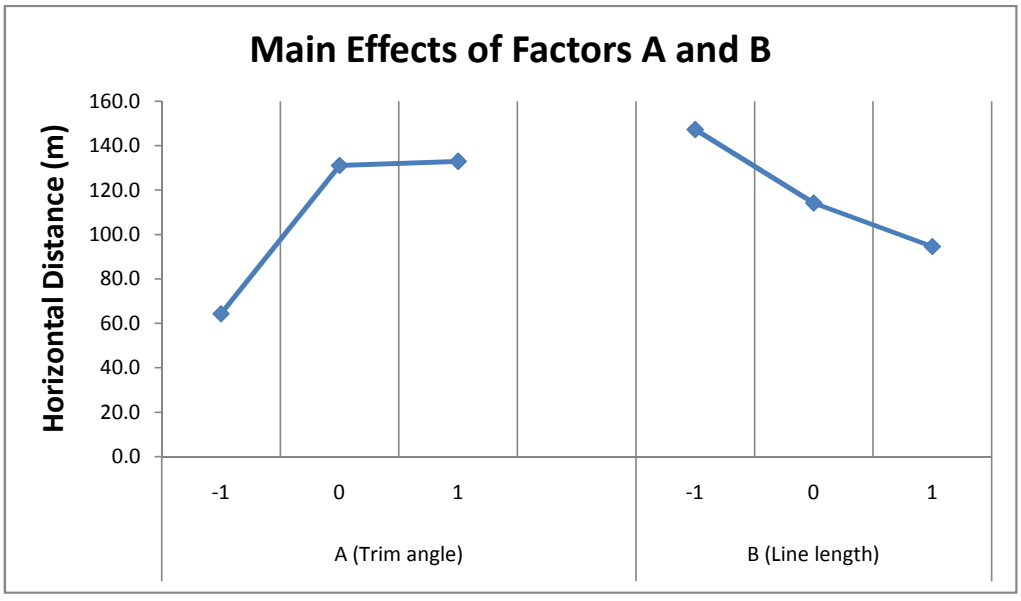

Figure 5.3: Main Effects of Trim Angle and Plumb Line Length on Horizontal Distance

The Interaction of Factor A and B on Horizontal Distance Travelled:

Similarly, using the blue and red blocks in Table 5.6, the distance variation was:

$$\frac{93.34 - 105.55}{1 - (-1)} = -6.10\ m$$

These results are tabulated in Table 5.7, where the magnitude of the slopes calculated is of importance. These values are required for the Pareto Chart in Fig. 5.5.

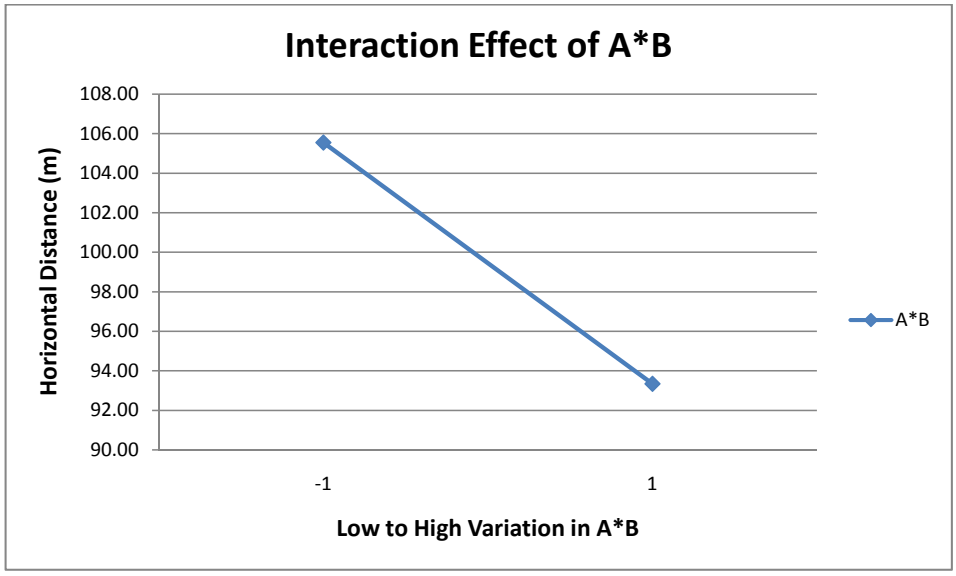

Figure 5.4: Interaction Effect of Trim Angle and Plumb Line Length on Horizontal Distance

Table 5.7: Contribution of All Effects on Horizontal Distance Travelled

Term	Norm of Slope
A	34.31
B	26.33
A × B	6.10

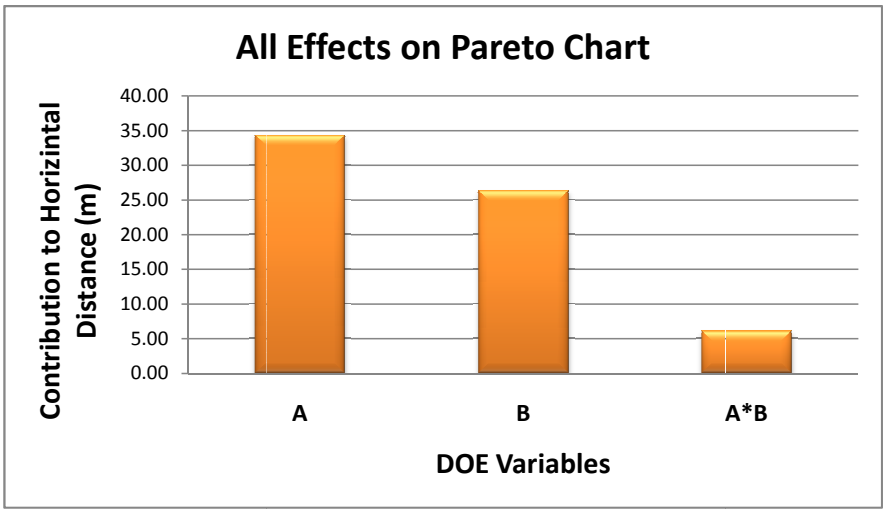

Figure 5.5: Pareto Chart of All Effects

Pareto Charts are very useful in DOE. The above results can be plotted on a Pareto type chart in order to make it much easier to visualize the main and interaction effects of all components on the horizontal distance travelled. It is very clear from the results above that Factor A (Trim Angle) has the most contribution to the horizontal distance variability and sensitivity. The main effects plot (shown in Fig. 5.3) for the trim angle indicate this steeper gradient of 34.31 m. The interaction effect of Factor A and B is relatively small compared to the other two main effects.

IMU Data

Due to some unfortunate events as mentioned before, data was only logged on the SD card for the very first flight test conducted. This was L1, Run 5. Trim angle was set at 9° and plumb line length set at $1 \times b$ (3.950 m). However, some useful information from this data was extracted.

The resultant velocity graph (Fig. 5.6) indicates that the start and end time of the flight was about 1690 s and 1702 s respectively. This was a flight time of approximately 12 seconds which coincides with the video footage from launch to landing. This graph also illustrates a phugoid period of about 6 seconds. The 3 green stars mark the positions at time = 1693, 1694, 1695 respectively, and the 3 red circles mark the positions at time = 1699, 1700, 1701 respectively. These points were used for the analysis of the IMU data for this flight test, and can be seen in Fig. 5.7 and 5.8 too.

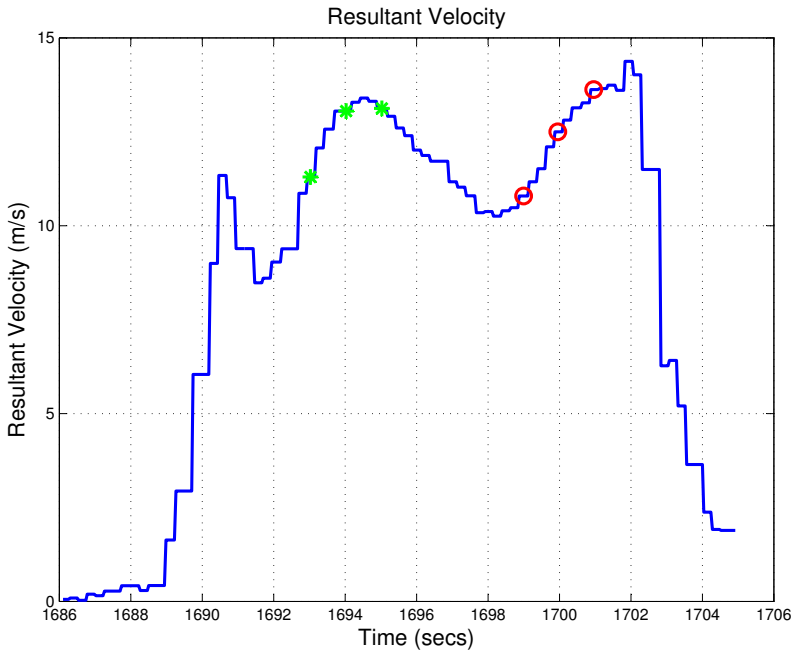

Figure 5.6: Resultant Velocity vs. Time

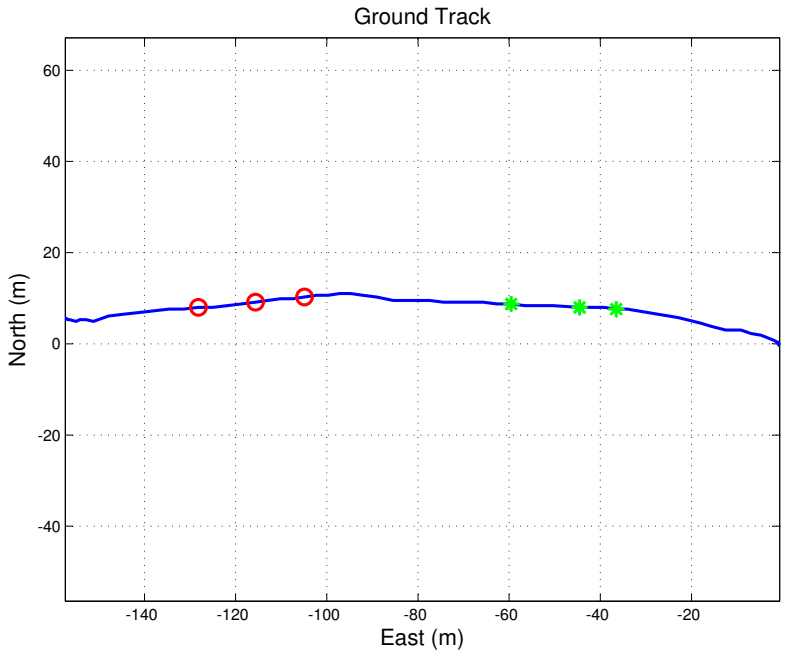

Figure 5.7: Ground Track of Flight Path

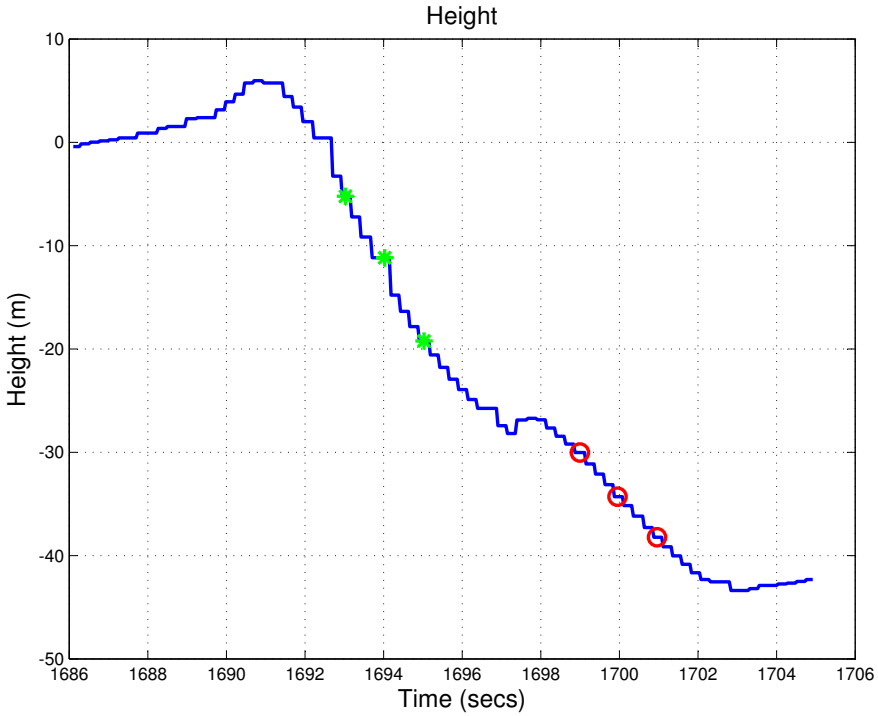

Figure 5.8: Elevation vs. Time

The decision to analyse the IMU data at two different time intervals was solely because of the lack of IMU data to begin with, as only one flight test logged data correctly. These points can be summarised as follows (see Table 5.8), and will be used in the subsequent calculations:

Table 5.8: Data Points from IMU

	Time (s)	**Velocity (m/s)**	**Height (m)**	**Path (m)**	
				East	**North**
	1693	11.30	-5.22	-36.50	7.60
Green	1694	13.05	-11.17	-44.55	7.98
	1695	13.12	-19.23	-59.56	8.74
	Average	**12.49**			
	1699	10.79	-30.04	-104.90	10.26
Red	1700	12.50	-34.30	-115.70	9.12
	1701	13.62	-38.23	-128.10	7.98
	Average	**12.30**			

Glide Slope Calculations:

Firstly, the horizontal distance was calculated as before, this time using the East and North data points for the path travelled from time 1693 s to 1695 s (i.e. the green stars).

$$\begin{aligned} d &= \sqrt{x^2 + y^2} \\ &= \sqrt{[-59.56 - (-36.50)]^2 + [8.74 - 7.60]^2} = 23.09\ m \end{aligned}$$

The vertical distance is just the difference in height.

$$h = -19.23 - (-5.22) = -14.01\ m$$

The negative sign just indicates downwards, therefore glide ratio (forward/down) was calculated as follows:

$$\frac{L}{D} = \frac{d}{h} = \frac{23.09}{14.01} = 1.65$$

And the glide angle was:

$$\gamma = \tan^{-1}\frac{h}{d} = \tan^{-1}\frac{14.01}{23.09} = 31.23^\circ$$

The same procedure was followed for the red circles and it was determined that,

$$\frac{L}{D} = 2.85$$

And

$$\gamma = 19.36^\circ$$

The glide angle as a function of time is illustrated in Fig. 5.9. The flight time was between 1690 and 1702 seconds and the difference in glide angle at the two time intervals is clearly shown. This graph also illustrates that the system did not have enough time to settle into its glide slope before landing. Figure 5.10 illustrates the simulated glide angle as a function of time for Run 5. It can be seen from this simulation that the system needs about 25 seconds to settle into its glide slope.

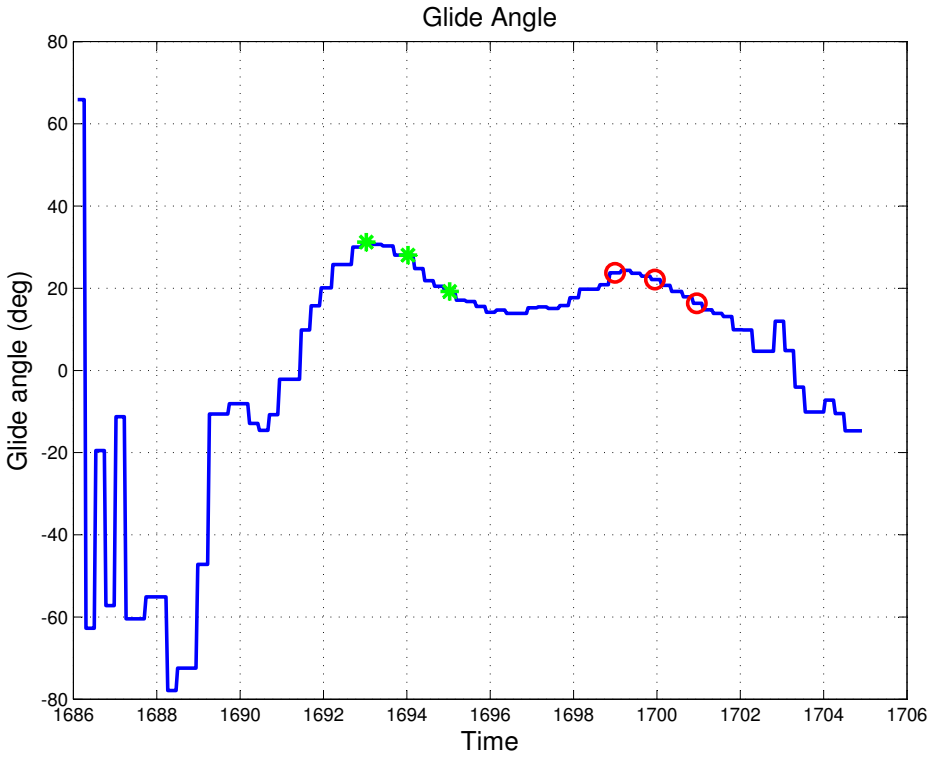

Figure 5.9: Glide Angle vs. Time for L1, Run 5

Frequency and Damping of the Phugoid Mode:

Using the notes and equations in Chapters 6 and 7 of Holt Ashley [22], the frequency and damping of the Long-Period Oscillation or phugoid mode was determined as follows:

$$\omega_n \cong \frac{C_{L0}}{\sqrt{2}\mu_s} \tag{5.2}$$

$$\mu_s = \frac{m}{\rho_\infty S \frac{c}{2}} \tag{5.3}$$

$$C_{L0} = \frac{mg}{\frac{1}{2}\rho_\infty V^2 S} \tag{5.4}$$

Substituting Equations 5.3 and 5.4 into 5.2, the frequency (dimensionless) can be expressed as:

$$\omega_n \cong \frac{cg}{\sqrt{2}V^2} \tag{5.5}$$

The damping ratio is:

$$\zeta \cong -\frac{C_{xu}}{2\sqrt{2}C_{L0}} \cong \frac{1}{\sqrt{2}\frac{L}{D}} \tag{5.6}$$

Now using the data collected from the IMU, for the green stars:

$$\omega_n \cong \frac{cg}{\sqrt{2}V^2} = \frac{1.53(9.81)}{\sqrt{2}(12.49)^2} = 0.068$$

$$\zeta \cong \frac{1}{\sqrt{2}\frac{L}{D}} = \frac{1}{\sqrt{2}(1.65)} = 0.43$$

Similarly for the red circles:

$$\omega_n = 0.070 \qquad \text{and} \qquad \zeta = 0.25$$

The phugoid period was determined using the equation below:

$$T = \frac{2\pi}{\omega_n}\left(\frac{c}{2V}\right) \tag{5.7}$$

The results from the IMU data analysis are tabulated in Table 5.9.

Table 5.9: Results from IMU Analysis of L1, Run 5

	L/D	**γ(°)**	**ω_n**	**ζ**	**T (s)**
Green stars	1.65	31.23	0.068	0.43	5.66
Red circles	2.85	19.36	0.070	0.25	5.57

Comparing the IMU data for this one flight with preliminary simulated results (see Table 5.10), it can be seen that for the part of the flight denoted by the red circles, the calculated glide angle and the settled simulated glide angle agree well. It should be noted that the glide angle calculated from the IMU data is probably slightly overestimated due to the cross-winds not being accounted for, however Fig. 5.7 illustrating the ground track for that particular flight test shows that the parafoil-payload system flew a relatively straight path. An even better comparison between the simulated glide angle and the experimental glide angle is illustrated in Fig. 5.11. The simulation was run for only 12 seconds, to coincide with the flight time of the preliminary test. However, it was unfortunate that data was logged for only one flight on the SD card of the IMU; therefore this comparison could have been a coincidence.

Table 5.10: Preliminary Simulated Results from MATLAB Model

	Factor		Response
Run	**A**	**B**	**Glide Angle (°)**
1	7	3.555	17.74
2	7	3.950	17.98
3	7	4.345	18.21
4	9	3.555	19.28
5	9	3.950	19.53
6	9	4.345	19.76
7	11	3.555	20.89
8	11	3.950	21.14
9	11	4.345	21.39

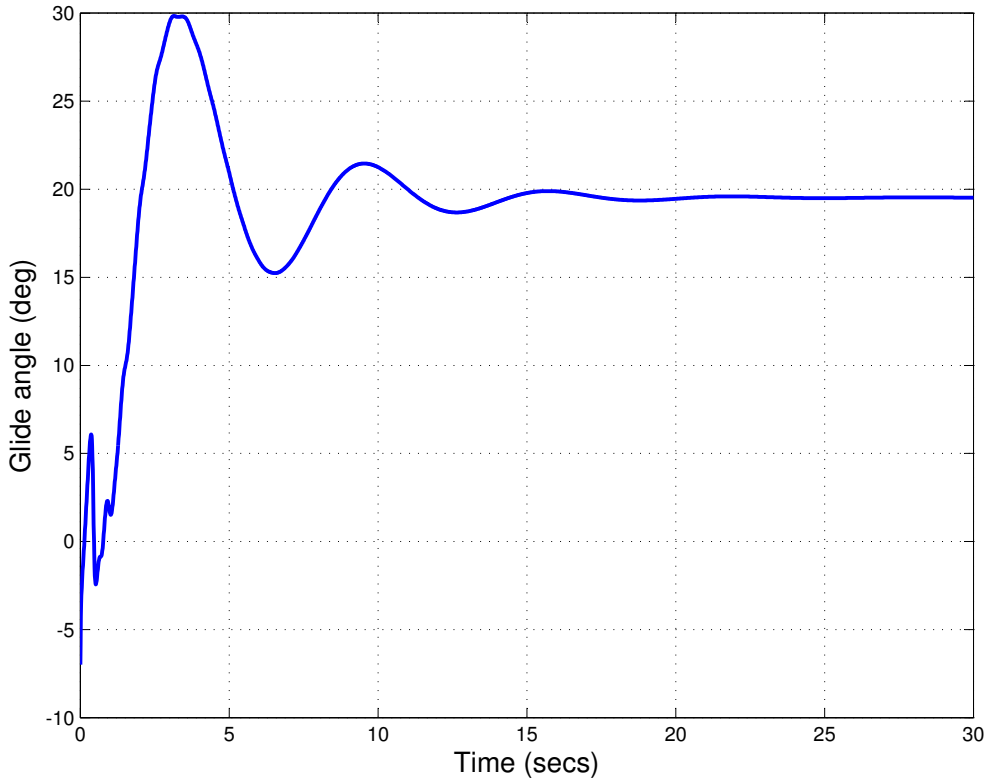

Figure 5.10: Simulated Glide Angle vs. Time for L1, Run 5

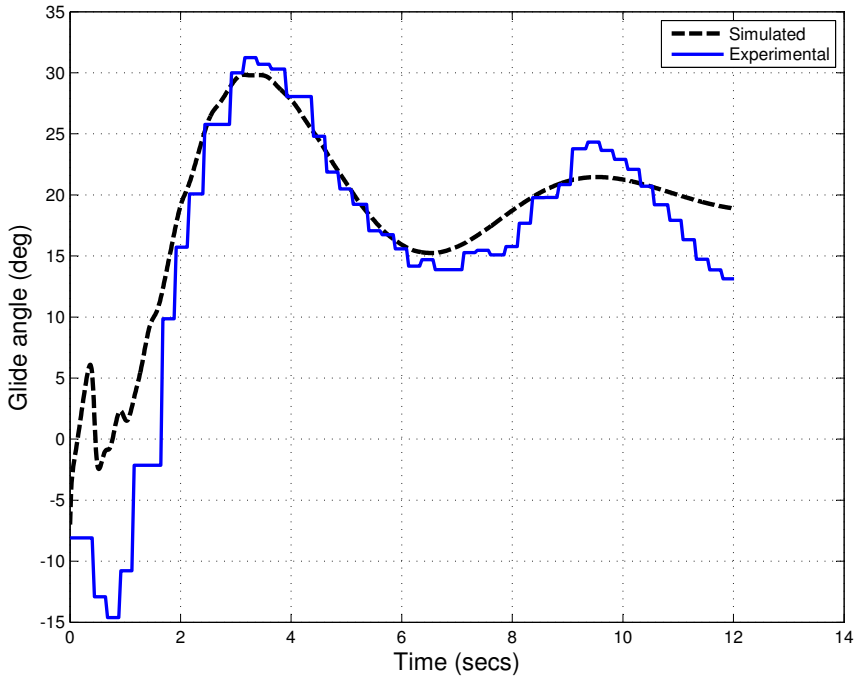

Figure 5.11: Comparison of Glide Angle vs. Time for L1, Run 5

5.2 Experimental Results from Flight Tests

Further flight tests were conducted on the 14^{th} and 24^{th} of January 2014. Due to the strong summer south-easterly winds, notorious to Cape Town, only two tests were conducted on the 14^{th} and three tests on the 24th, totalling five tests in January. The strong winds wreaked havoc with the flight testing throughout the summer months. Relatively calm days to conduct tests were few and far between, and sometimes testing would be cancelled as the strong winds made it very difficult to set up the parafoil launcher for a successful launch. Often, when the wind was a bit gusty, the parafoil canopy would accidentally shift along the crossbar, or "fold" on itself. As the launch arm rotated around, the canopy would not inflate properly.

On occasions, as with most experimental tests, damages to the testing equipment occurred. Noticeable damages during the flight tests were: parafoil canopy rips and tears, payload box damages due to hard landings (especially in crashes), and suspension line breaks to name a few. To make matters worse, after analysing the logged data, it was discovered that the IMU had been damaged following the tests conducted in January. The dis-

covery was made while analysing the Euler angles. Visual observation of a flight test showed a significant heading change, however, the IMU data indicated an unrealistic yaw angle (See Fig. 5.12). A significant change in heading was noticeable to the naked eye in all the flights, however a change in yaw angle of about 120° in only 12 seconds would have been very obvious; and this was definitely not the case from visual observation. Subsequent to this discovery, it was decided that the avionics system (IMU, estimator and GPS) required recalibration. In addition, the secondary IMU placed on the parafoil canopy seldomly worked, because the ribbon cable connecting the IMU to the payload box often disconnected or broke.

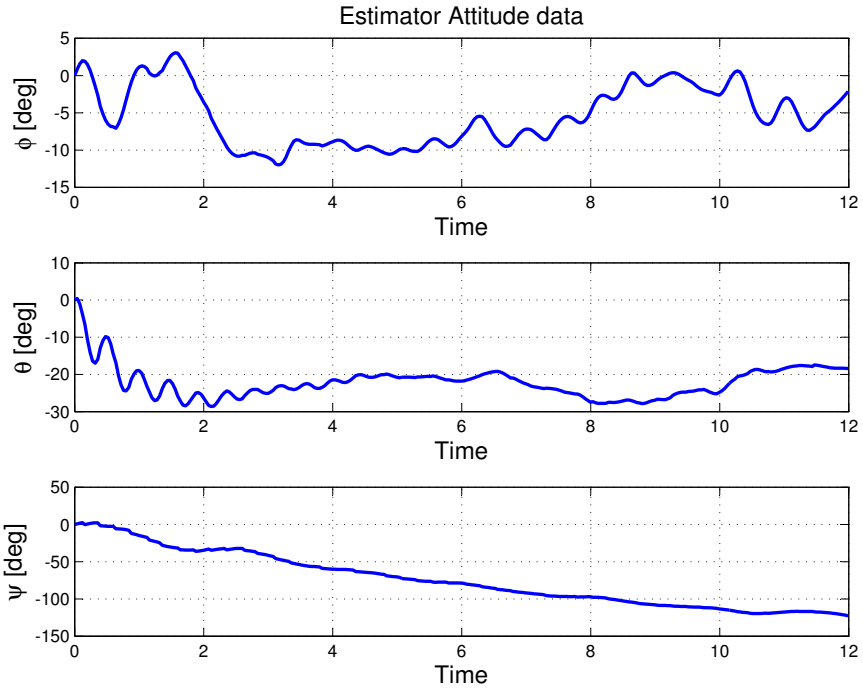

Figure 5.12: Estimator Attitude Data

With the risk of unrepairable damage occurring if testing continued for the duration of the strong windy summer months, and with the avionics sent away for recalibration, a decision was made to stop the experimental flight testing. As the time to complete this investigation became more limited, a revised plan had to be devised. This new plan entailed simulating the flight tests with a more "realistic" theoretical model in an attempt to mimic the experiments, shifting the focus of the investigation to the simulated results rather than the experimental results. Refer to Section 5.3, where this will be discussed in greater detail. Nevertheless, for completeness, the results gathered from the experimental flight tests in January are documented below.

Table 5.11: January 2014 Flight Tests

#	**Date**	**Time**	**A (deg)**	**B (m)**	**Temp.** ($^{\circ}C$)	**Wind (m/s)**	**Air Pressure (mb)**
1	14/01/2014	9:55	9	3.950	29.8	0.7 NW	981
2	14/01/2014	11:15	9	3.950	32.3	1.3 N	985
3	24/01/2014	10:07	9	3.950	21.9	2.9 SW	984
4	24/01/2014	10:40	11	4.345	22.5	3.6 SW	985
5	24/01/2014	11.14	10	3.555	22.7	2.9 NW	985

Data was logged for each of the five tests except for Test 4, because that particular log file became corrupt. Graphs of the ground track, elevation, resultant velocity and glide angle for each flight can be found in Appendix D. The glide angle was calculated by taking the gradient of the change in horizontal and vertical distance. In an attempt to try and quantify these tests, the steady glide angle was approximated by taking the mean of the glide angle for the last 6-8 seconds of the flight data. These results are tabulated in Table 5.12. This crude method of approximating the glide angle is obviously flawed for three reasons: 1. For such a short flight duration, the parafoil-payload system has not had enough time to settle into a steady glide angle before it hits the ground. 2. Cross-winds result in the flight path being significantly longer than that obtained by taking the gradient of the change in horizontal and vertical distance (see ground track figures in Appendix D). 3. The integrity of the IMU data was questionable, as seen by the errors in the Euler angles mentioned above; and by what has not yet been mentioned, inaccuracies in GPS measurements. However, for completeness, these results are presented here.

Table 5.12: Results from January 2014 Flight Tests

Flight #	**Glide Angle (°)**
1	$\approx$ 24.29
2	$\approx$ 18.86
3	$\approx$ 18.51
4	/
5	$\approx$ 36.34

Despite the flight tests being rather disappointing and yielding unsatisfactory results, some useful information was however still observed. For instance, it was noticed that launching the parafoil-payload system at 12 m/s, resulted in a large upward pitching motion right after launch. This meant

that the parafoil's phugoid mode was prominent. Therefore, the launch speed was lowered to 10 m/s in future flights and a noticeable change in phugoid mode was observed as the parafoil-payload system settled into its glide slope quicker than before. Another useful observation, already noted in Section 5.1, is that the trim angle setting of 7° was inadequate. Lastly, the effect of wind disturbances could not be ignored, as it was evident that the parafoil-payload system was susceptible to even relatively small changes in wind.

5.3 Simulated Results using MATLAB Model

Following from the discussion in the previous section, simulations were run based on the algorithm described in Chapter 3. The useful information highlighted from the failed flight tests aided in the fulfilment of the simulations of flight. For example, the initial conditions for the differential equations described in Section 3.6 were adjusted to best simulate the real life scenario, and hence the discovery of lowering the launch speed was a significant one. In addition, simulations were run without the inadequate trim angle setting of 7°. Instead the trim angle setting ranged from 9 to 13 degrees, as depicted in Table 5.13. DOE was applied to investigate the factor effects and their interaction, to determine important system trends. More significantly though, the effect of wind disturbances, in conjunction with the trim settings, on glide slope was investigated.

Table 5.13: Control Factors and Levels for Simulation Tests

Control Factor	**Low Level (-1)**	**Intermediate Level (0)**	**High Level (+1)**
A:Trim Angle (°)	9	11	13
B:Plumb Line Length (m)	3.555 (0.9×b)	3.950 (1×b)	4.345 (1.1×b)

The simulations were isolated into two sections, the mean wind simulations described by Section 5.3.1 and the turbulence simulations described by Section 5.3.2. In both cases, the effect of the trim settings, in conjunction with these wind disturbances, on the glide angle was investigated. Glide angle was determined from the simulations in two ways, and has been denoted as *absolute* glide angle and *relative* glide angle, or *abs/A* and *rel/R* respectively. The absolute glide angle is essentially just the slope of an altitude versus distance graph, whereas the relative glide angle is the slope of

altitude versus distance covered with respect to the prevailing wind. In each case, a glide angle response similar to that of Fig. 5.13 was replicated for each of the trim settings.

Absolute Glide Angle

$$\text{Absolute Glide Angle} = \tan^{-1}\left(\frac{\delta z_{pl}}{\delta x_{pl}}\right) \tag{5.8}$$

Relative Glide Angle

$$\text{Relative Glide Angle} = \tan^{-1}\left(\frac{W_{pl} + w_w + w_g}{U_{pl} + u_w + u_g}\right) \tag{5.9}$$

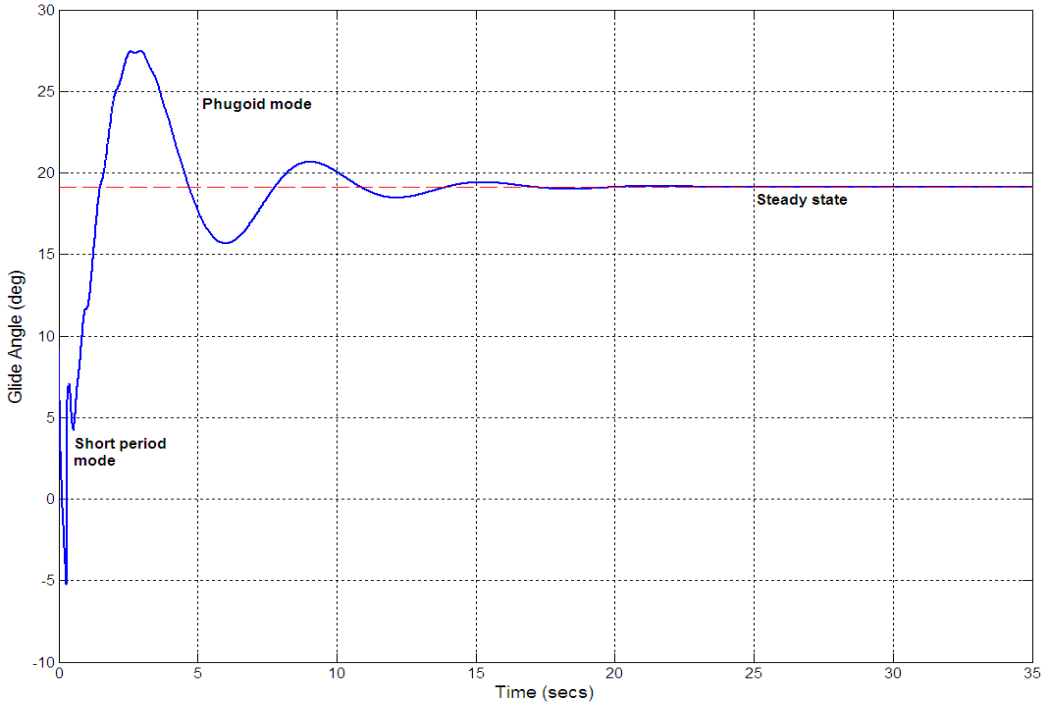

Figure 5.13: Glide Angle Response in Still Conditions

5.3.1 The Mean Wind Case

To illustrate the effect of mean wind, simulations were run with a headwind and tailwind of 1 m/s. Immediately, it should be evident that if the parafoil-payload system is flying directly into a headwind, the distance it travels for a

given altitude should be less than that of a no wind case. Conversely, flying with a tailwind directly behind the system, the distance it travels should be greater. This is illustrated in Fig. 5.14, where the gradient of altitude versus distance is steeper in the headwind case than that of the tailwind case. A steeper gradient translates to a larger "absolute" glide angle, as depicted in Fig. 5.15.

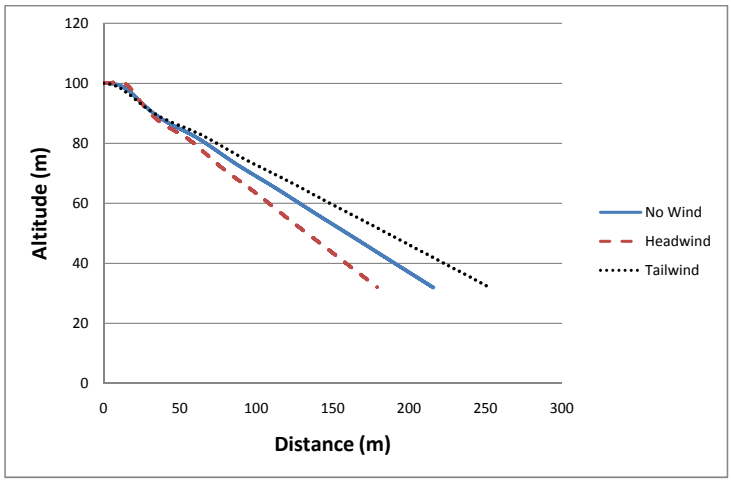

Figure 5.14: Effect of Mean Wind on Altitude and Distance for Run 1

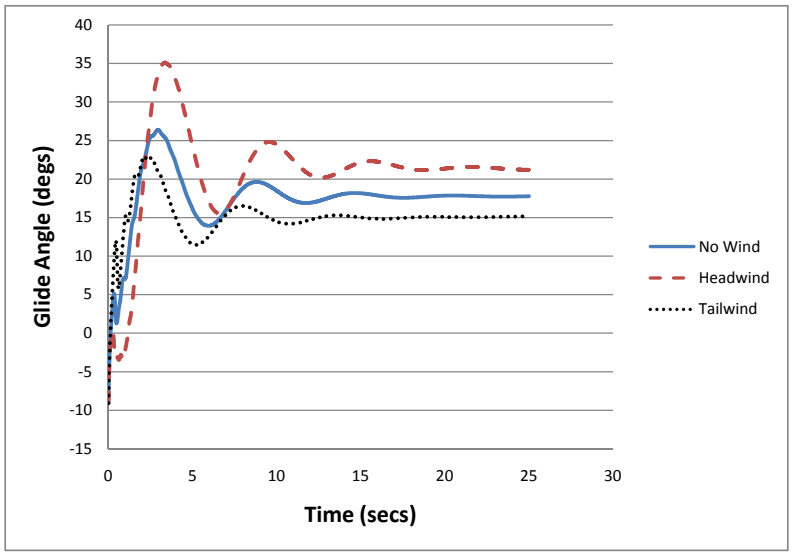

Figure 5.15: Effect of Mean Wind on Absolute Glide Angle for Run 1

However, the calculation of "relative" glide angle takes into account the wind velocity components, thus the settled glide angle value should be the same as the no wind case. Figure 5.16 illustrates how the glide angle in all three cases (no wind, headwind and tailwind) converge to a settled glide angle after some time.

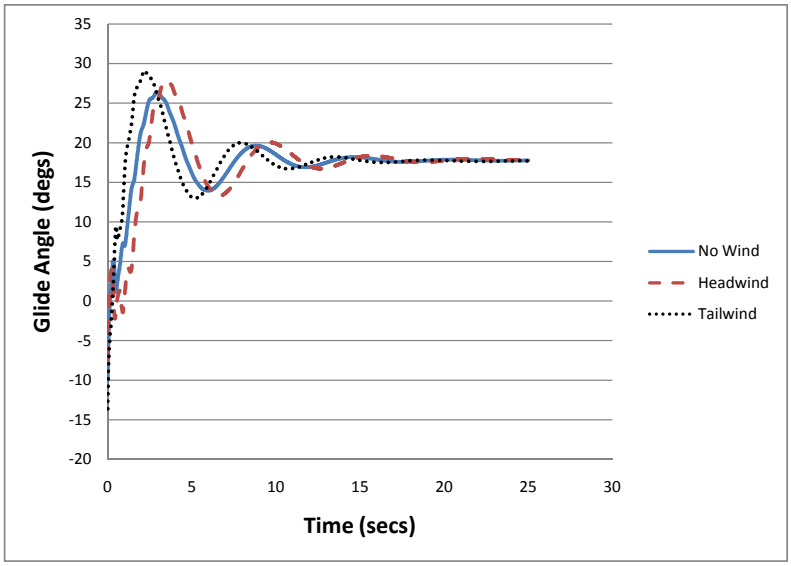

Figure 5.16: Effect of Mean Wind on Relative Glide Angle for Run 1

Table 5.14: Simulated Results with Mean Wind from MATLAB Model

	Factor		Response (Glide Angle (°))				
Run	**A**	**B**	**No Wind**	**Head abs**	**Head rel**	**Tail abs**	**Tail rel**
1	9	3.555	17.77	21.52	17.89	15.02	17.67
2	9	3.950	18.15	21.94	18.27	15.35	18.04
3	9	4.345	18.51	22.34	18.63	15.67	18.39
4	11	3.555	18.71	22.25	18.85	16.02	18.58
5	11	3.950	19.15	22.72	19.29	16.43	19.02
6	11	4.345	19.57	23.16	19.70	16.81	19.43
7	13	3.555	19.88	23.23	20.05	17.25	19.71
8	13	3.950	20.39	23.76	20.57	17.73	20.20
9	13	4.345	20.86	24.26	21.05	18.17	20.66
Average			19.22	22.80	19.37	16.49	19.08

All simulations were run for a duration of 25 seconds and the graphs of the results for the other 8 runs are illustrated in Figs. E.1 - E.3 in Appendix E.

The average absolute and relative glide angle over the last 10 seconds of flight was determined for each run, under each of the three conditions, and these results are tabulated in Table 5.14. Figures 5.17 and 5.18 illustrate the effect plumb line length and trim angle have on absolute glide angle respectively. 'HW' and 'TW' denote headwind and tailwind respectively. The relative values are omitted in these two graphs, because the relative glide angle is very similar to that of the no wind case.

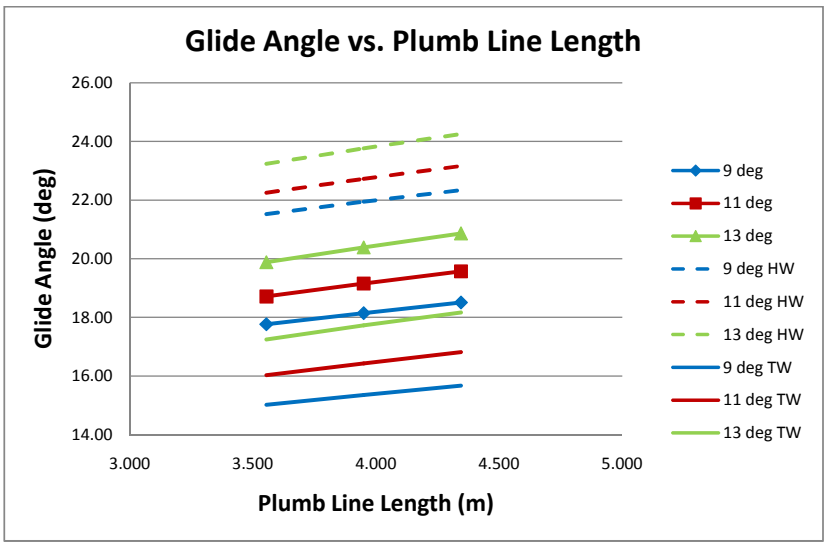

Figure 5.17: Glide Angle vs. Plumb Line Length in Mean Wind

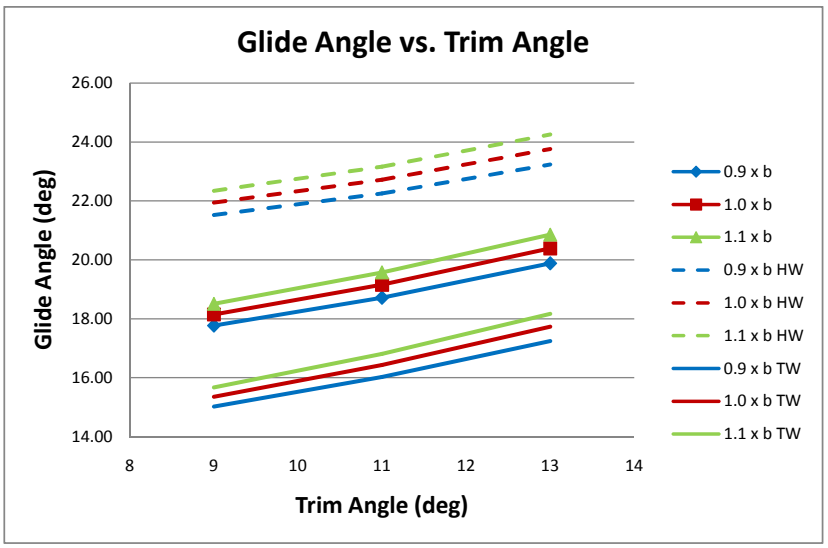

Figure 5.18: Glide Angle vs. Trim Angle in Mean Wind

DOE Analysis

Similar to the Design of Experiments analysis conducted in Section 5.1, the settled glide angle values from the simulations were investigated. The glide angle is first averaged according to the factor and level. For example, referring back to Table 5.14, the average glide angle for the low level of trim angle in no wind is determined as follows:

$$\frac{17.77 + 18.15 + 18.51}{3} = 18.14^\circ$$

The same calculation was performed on the absolute and relative glide angles, under both a headwind and tailwind condition, and these results are tabulated in Table 5.15. The orange and green highlighted rows correspond to the highlighted rows in Table 5.14, representing the low and high interaction effects respectively.

Table 5.15: Factor and Interaction Effects on Glide Angle in Mean Wind

Factor	**Level**	**Average Glide Angle (°)**				
		No Wind	*Head A*	*Head R*	*Tail A*	*Tail R*
A (Trim Angle)	−1	18.14	21.94	18.27	15.35	18.03
	0	19.14	22.71	19.28	16.42	19.01
	+1	20.37	23.75	20.55	17.71	20.19
B (Line Length)	−1	18.79	22.34	18.93	16.10	18.65
	0	19.23	22.81	19.38	16.50	19.09
	+1	19.64	23.25	19.79	16.88	19.49
A × B	−1	19.19	22.79	19.34	16.46	19.05
	+1	19.31	22.89	19.47	16.59	19.17

Now, to investigate the contribution the factor effects have on the absolute glide angle in mean wind, the following calculations were required:

Main effect of Trim Angle (A) on Absolute Glide Angle:

Focusing on the headwind case, the average absolute glide angle was calculated when A is "−1" and when A is "+1" (refer to Table 5.15), and the average absolute glide angle variation from the low to high level of trim angle was determined as follows:

$$\frac{23.75 - 21.94}{1 - (-1)} = 0.91^\circ$$

The same procedure was followed for the no wind and tailwind cases. Data from Table 5.15 is illustrated in Figs. 5.19 - 5.21.

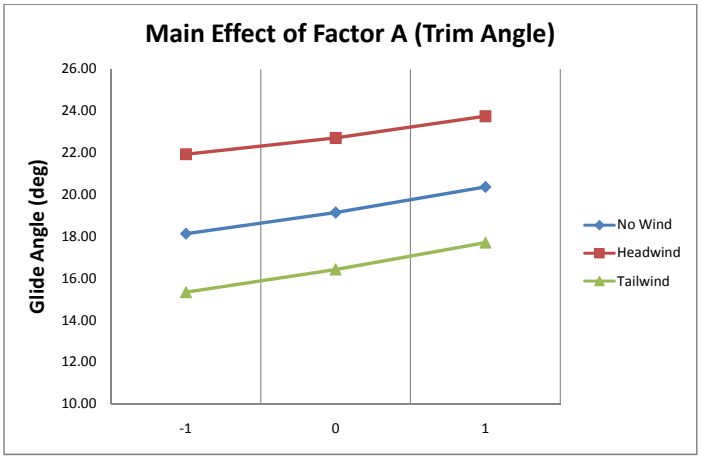

Figure 5.19: Main Effect of Trim Angle on Glide Angle in Mean Wind

Main effect of Plumb Line Length (B) on Absolute Glide Angle:

The average absolute glide angle of B (-1) in the headwind case was 22.34 and of B (+1) was 23.25 (refer to Table 5.15). Therefore, the absolute glide angle variation was:

$$\frac{23.25 - 22.34}{1 - (-1)} = 0.46^{\circ}$$

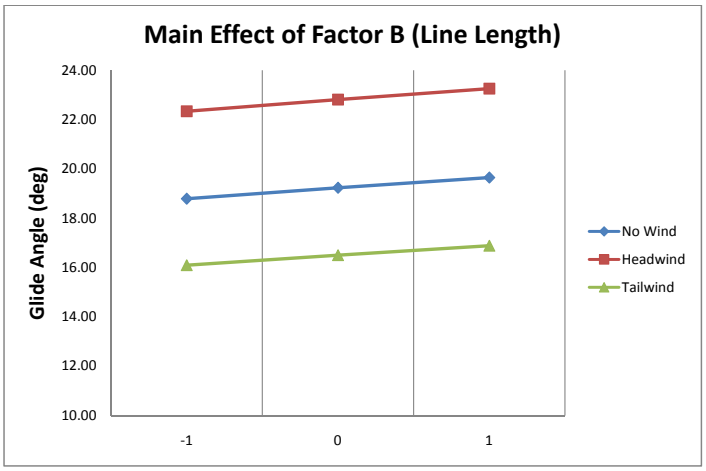

Figure 5.20: Main Effect of Plumb Line Length on Glide Angle in Mean Wind

The Interaction of Factor A and B on Absolute Glide Angle:

Similarly, using the orange and green rows in Table 5.15, the absolute glide angle variation in the headwind case was:

$$\frac{22.89 - 22.79}{1 - (-1)} = 0.05^{\circ}$$

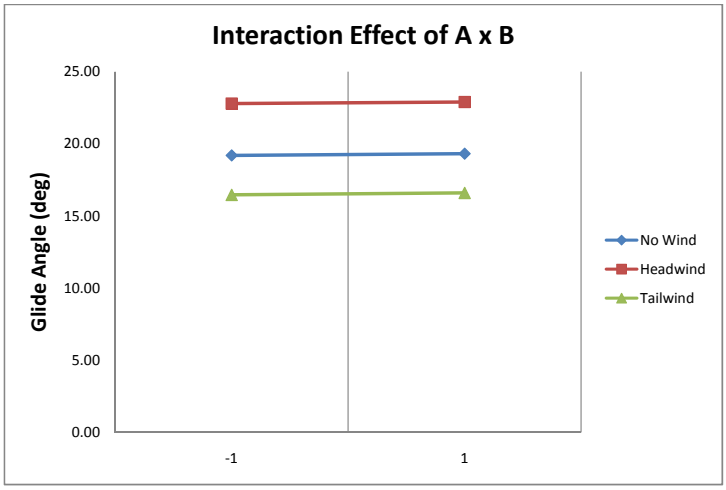

Figure 5.21: Interaction Effect of Trim Angle and Plumb Line Length on Glide Angle in Mean Wind

The above results are tabulated in Table 5.16, where the magnitude of the slopes calculated is of importance. These values are required for the Pareto Chart in Fig. 5.22. Note that throughout this DOE analysis, the relative values were omitted, because as stated before, the relative glide angle is very similar to that of the no wind case. Hence, the main and interaction effects on glide angle are essentially the same as the no wind case. From the Pareto Chart, it is evident that Factor A (Trim Angle) contributes the most to the glide angle variability and sensitivity in all three conditions. The interaction effect is relatively small compared to the other two main effects. In tailwind conditions, trim angle has a slightly greater effect on the glide angle compared to the no wind condition; and when compared to the headwind condition, an even bigger effect. The converse is true for plumb line length.

Table 5.16: Contribution of All Effects on Glide Angle in Mean Wind

Term	**Norm of Slope**				
	No Wind	*Head A*	*Head R*	*Tail A*	*Tail R*
A	1.12	0.91	1.14	1.18	1.08
B	0.43	0.46	0.43	0.39	0.42
A × B	0.06	0.05	0.07	0.07	0.06

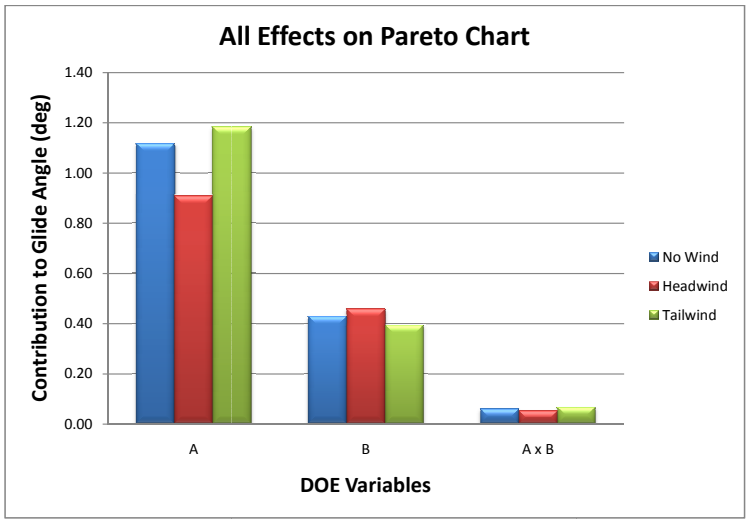

Figure 5.22: Pareto Chart of All Effects in Mean Wind

5.3.2 The Atmospheric Turbulence Case

For the atmospheric turbulence case, the simulations were run in a slightly different manner. First a "pseudo" simulation was run, that mimics an experimental flight test, meaning that the simulated flight stops when the parafoil-payload system hits the ground. Then an "extended" simulation was run using the end conditions from the pseudo simulation as the initial conditions for this extended simulation in the same atmospheric state. The initial conditions for the extended simulations are inherently randomly generated, because the atmospheric turbulence was modelled using non-repeating Gaussian white noise sources. The concept behind this procedure was to predict what happens after the parafoil-payload system makes contact with the ground, since it was discovered from actual experimental flight tests that

when the system hits the ground, the system had not yet reached a settled glide angle; the reason being that the experimental flight tests were limited by the height of the quarry where the launches were conducted.

In addition, in an attempt to quantify the feasibility of this method, and because turbulence is a stochastic process, a "long" simulation (longer in duration and with no height restriction) was run to determine the error between the "long" and "extended" simulations. The research question that is being addressed in this section is: How accurate an estimate of the glide slope could be obtained by conducting a quarry flight test, measuring the landing point and the prevailing atmospheric conditions, followed by extending the trajectory to a steady state by means of a trajectory ("extended") simulation in similar atmospheric conditions.

Figure 5.23 briefly illustrates this method. The blue solid line indicates the pseudo simulation of Run 1 in light turbulence. When the altitude reached 0 metres, an event function was triggered and the pseudo simulation stopped (indicated by the vertical black line). The extended simulation then starts at this point and is denoted by the red solid line. The black dashed line indicates the long simulation and correlates well with the pseudo simulation. However, after the vertical line, a deviation between the long and extended simulation is noticeable. It is this discrepancy that will be used to determine the error. Similar graphs for the other 8 runs are illustrated by Fig. E.4 in Appendix E.

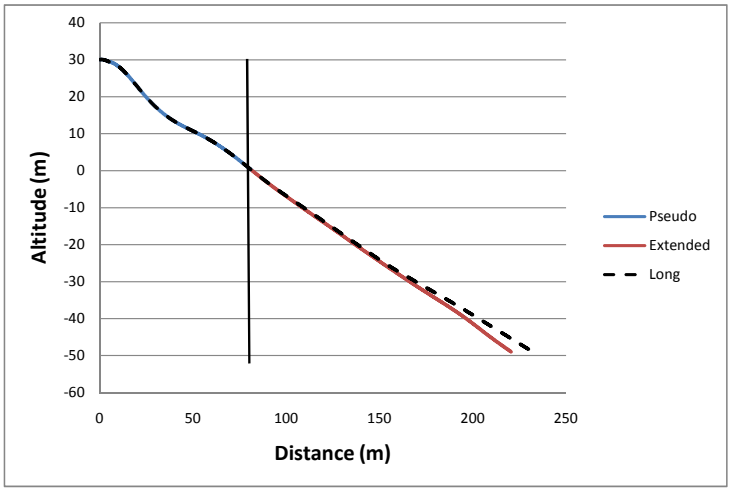

Figure 5.23: Error Effect of Light Turbulence on Altitude and Distance for Run 1

Figures 5.24 and 5.25 illustrate the absolute and relative glide angle for Run 1 in light turbulence respectively. The error between the extended and long simulation is more evident now, especially in the calculation of absolute glide angle. Similar to the mean wind case, the relative glide angle now takes into account the turbulent gust velocity components. The settled relative glide angle value should be the same as the no turbulence or still condition. However, this is not necessarily the case, because turbulence is a random process. Similar graphs for the other 8 runs are illustrated by Figs. E.5 and E.6 in Appendix E.

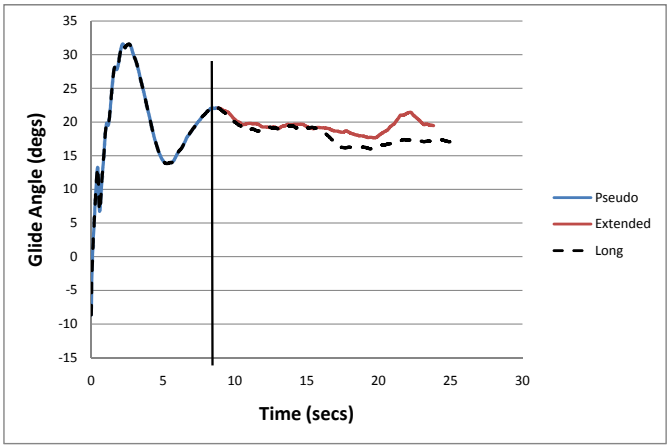

Figure 5.24: Error Effect of Light Turbulence on Absolute Glide Angle for Run 1

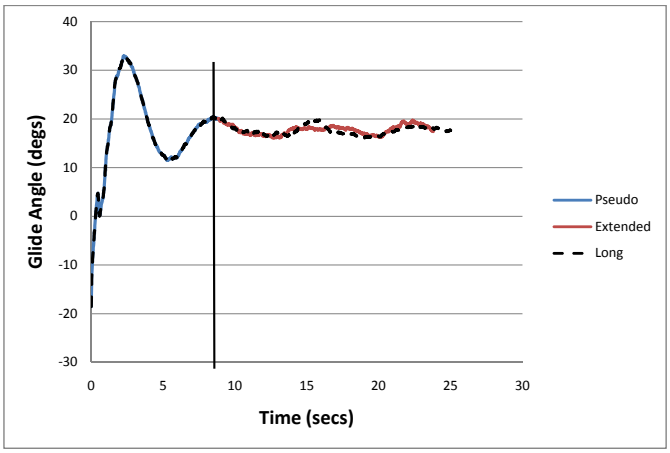

Figure 5.25: Error Effect of Light Turbulence on Relative Glide Angle for Run 1

The same approach was followed for the moderate and severe turbulence levels. Figures 5.26 and 5.27 illustrate the absolute and relative glide angle for Run 1 in moderate turbulence respectively. Notice that the error between the extended and long simulation is more prominent now in moderate turbulence conditions. The other 8 runs are illustrated by Figs. E.7 and E.8, and are presented in Appendix E.

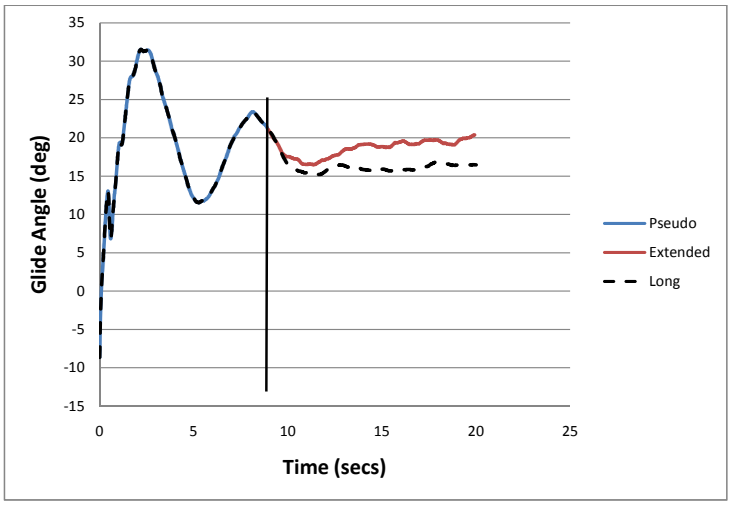

Figure 5.26: Error Effect of Moderate Turbulence on Absolute Glide Angle for Run 1

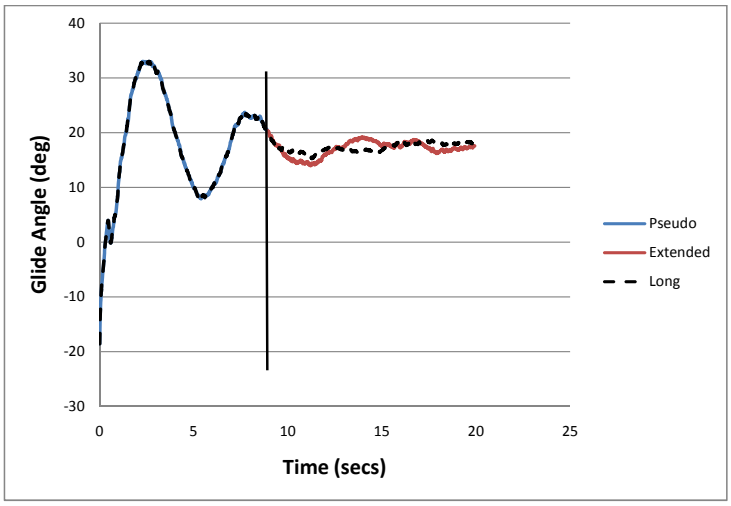

Figure 5.27: Error Effect of Moderate Turbulence on Relative Glide Angle for Run 1

Figures 5.28 and 5.29 illustrate the absolute and relative glide angle for Run 1 in severe turbulence respectively. The other 8 runs are illustrated by Figs. E.9 and E.10, and are presented in Appendix E.

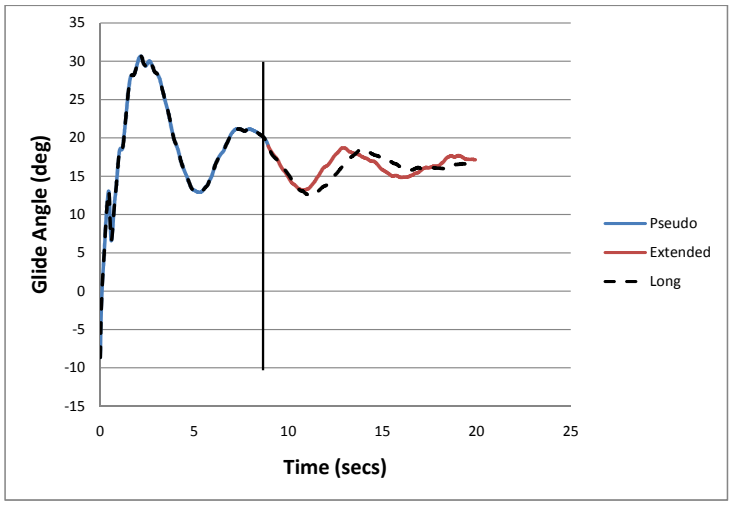

Figure 5.28: Error Effect of Severe Turbulence on Absolute Glide Angle for Run 1

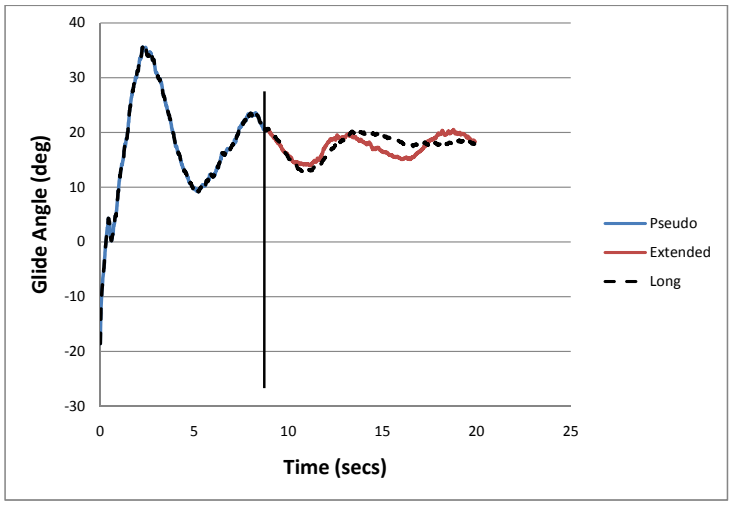

Figure 5.29: Error Effect of Severe Turbulence on Relative Glide Angle for Run 1

Figures 5.30 and 5.31 illustrate the effect turbulence has on absolute and relative glide angle for Run 1 respectively. The long simulations for the three turbulence levels are plotted in these graphs, and in addition, the still

condition already determined in the mean wind case is plotted too. The other 8 runs are illustrated by Figs. E.11 and E.12, and are presented in Appendix E.

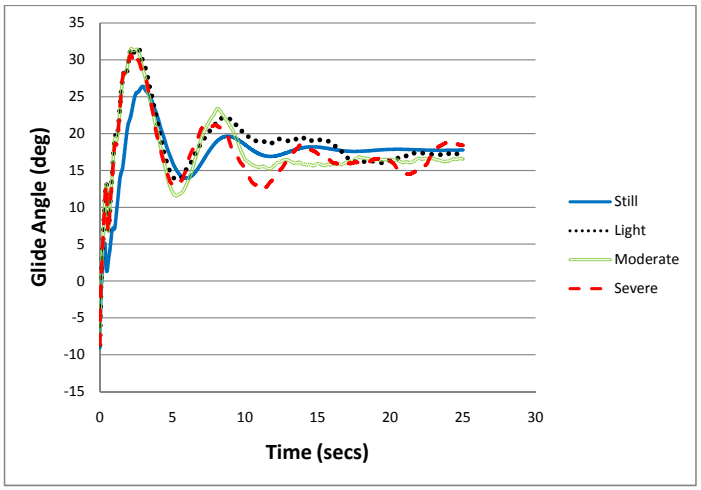

Figure 5.30: Effect of Turbulence on Absolute Glide Angle for Run 1

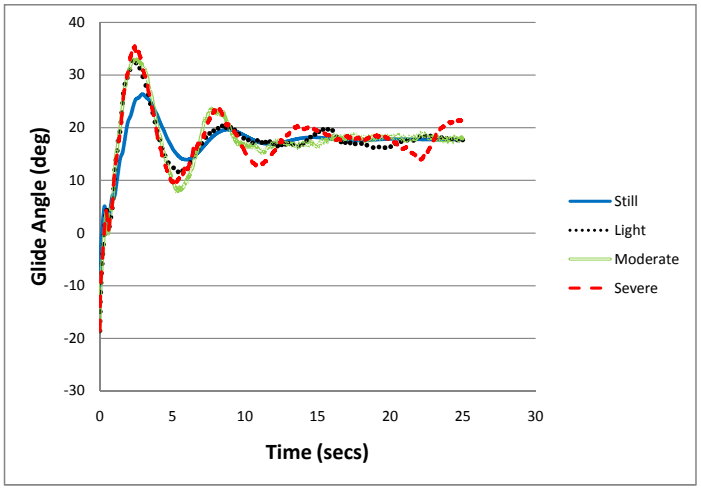

Figure 5.31: Effect of Turbulence on Relative Glide Angle for Run 1

All 9 possible trim setting combinations were investigated under the 3 turbulence levels described in Section 2.1.5. An example of the turbulent gust profiles generated by the MATLAB model is illustrated in Fig. 5.32. Again, the glide angle was determined in the same two ways as described above for the extended and long simulations. The average absolute and relative

glide angle for the duration of the extended simulation was determined for each run. However, for the long simulations, the average glide angle was determined over the second part of the flight equivalent to the duration of the extended simulations. The duration of the extended simulations usually ranged between 10 and 15 seconds. The results from these calculations are tabulated in Tables 5.17 and 5.18.

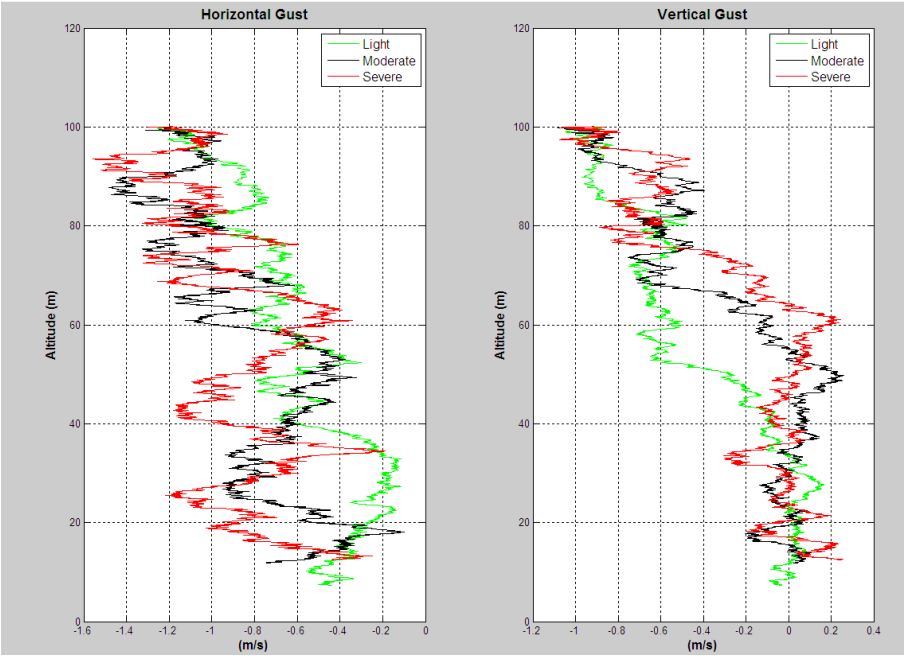

Figure 5.32: Example of the Turbulent Gust Profiles Generated

Table 5.17: Extended Simulation Results with Turbulence from MATLAB Model

	Factor		Response (Glide Angle (°))						
Run	**A**	**B**	**No Turb**	**Light A**	**Light R**	**Mod A**	**Mod R**	**Sev A**	**Sev R**
1	9	3.555	17.77	19.44	17.79	18.69	17.10	16.26	17.42
2	9	3.950	18.15	15.63	18.00	14.47	17.98	12.72	17.63
3	9	4.345	18.51	20.72	18.66	22.16	18.82	22.83	18.71
4	11	3.555	18.71	20.84	18.98	20.79	19.07	22.39	19.07
5	11	3.950	19.15	16.16	19.06	15.42	18.96	15.36	19.00
6	11	4.345	19.57	15.17	19.50	15.35	19.61	15.64	19.48
7	13	3.555	19.88	15.56	19.89	15.40	20.05	14.86	20.02
8	13	3.950	20.39	25.31	20.28	27.68	20.48	27.65	20.45
9	13	4.345	20.86	19.33	20.74	19.46	20.62	19.53	20.76

Table 5.18: Long Simulation Results with Turbulence from MATLAB Model

	Factor		Response (Glide Angle (°))					
Run	**A**	**B**	**Light A**	**Light R**	**Mod A**	**Mod R**	**Sev A**	**Sev R**
1	9	3.555	17.78	17.50	16.28	17.34	15.97	17.60
2	9	3.950	14.64	18.08	12.53	18.60	8.59	18.49
3	9	4.345	20.69	18.55	20.42	18.88	19.78	19.08
4	11	3.555	20.35	19.03	20.39	18.75	20.36	18.28
5	11	3.950	15.07	18.76	14.83	18.66	16.44	19.00
6	11	4.345	14.91	19.36	14.88	20.02	11.48	19.14
7	13	3.555	15.53	19.76	14.39	19.82	14.76	20.17
8	13	3.950	24.78	20.53	24.66	20.55	24.22	20.52
9	13	4.345	18.30	21.04	18.05	20.91	18.32	20.90

The difference between the long and extended simulation indicates how successful this method was in determining the settled glide angle. Referring to Tables 5.17 and 5.18, the error in absolute glide angle for Run 1 under light turbulence was calculated as follows:

$$\begin{aligned} error(\%) &= \frac{|\gamma_{long} - \gamma_{extended}|}{\gamma_{long}} \times \frac{100}{1} \\ &= \frac{|17.78 - 19.44|}{17.78} \times \frac{100}{1} \\ &= 9.38 \end{aligned}$$

Therefore, for Run 1 under light turbulence, there is an error of 9.38% in this method of determining the glide angle. The same calculation was performed to determine the error in absolute and relative glide angle for all 9 runs under the three turbulence levels. These results are tabulated in Table 5.19. The validity of this method needs to be accounted for, because in future, if an actual experimental flight test is conducted until the system hits the ground; and the end conditions of the flight known from say IMU data, then an extended simulation could be run to predict what the settled glide angle value would be after more time has elapsed.

Table 5.19: Error in Absolute and Relative Glide Angle in Turbulence

	Error (%)					
Run	**Light A**	**Light R**	**Mod A**	**Mod R**	**Sev A**	**Sev R**
1	9.38	1.66	14.78	1.37	1.82	1.00
2	6.78	0.43	15.45	3.32	47.97	4.67
3	0.14	0.63	8.52	0.32	15.41	1.91
4	2.42	0.29	1.95	1.75	9.95	4.29
5	7.25	1.64	3.95	1.60	6.59	0.01
6	1.74	0.70	3.12	2.02	36.31	1.75
7	0.19	0.66	7.04	1.17	0.69	0.78
8	2.13	1.24	12.22	0.36	14.17	0.35
9	5.64	1.44	7.79	1.42	6.58	0.66

Figures 5.33 and 5.34 illustrate the effect plumb line length and trim angle have on absolute glide angle in turbulence respectively. 'L', 'M' and 'S' denote light, moderate and severe turbulence respectively. The relative values are omitted in these two graphs to ensure neat presentation of the results from Table 5.17. Note that these graphs were generated using the extended simulation results.

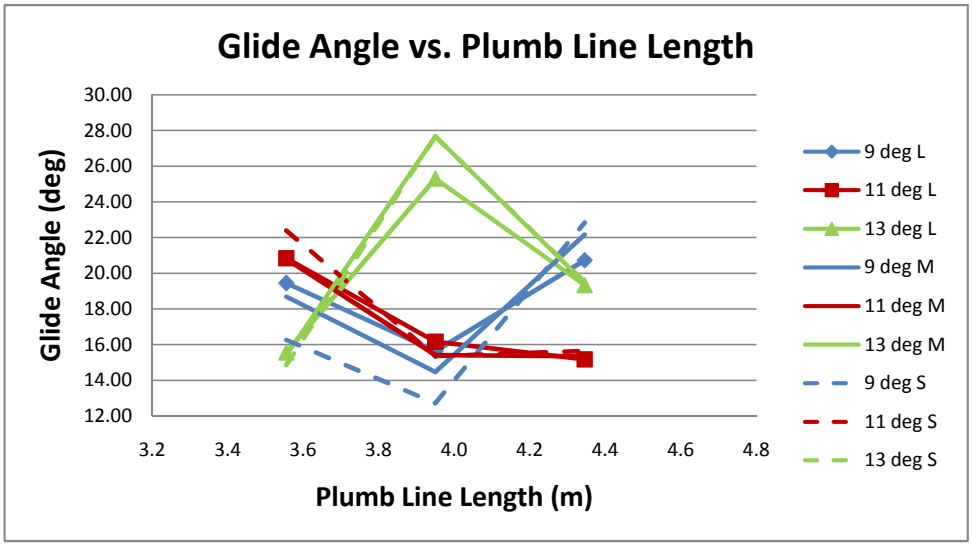

Figure 5.33: Glide Angle vs. Plumb Line Length in Turbulence

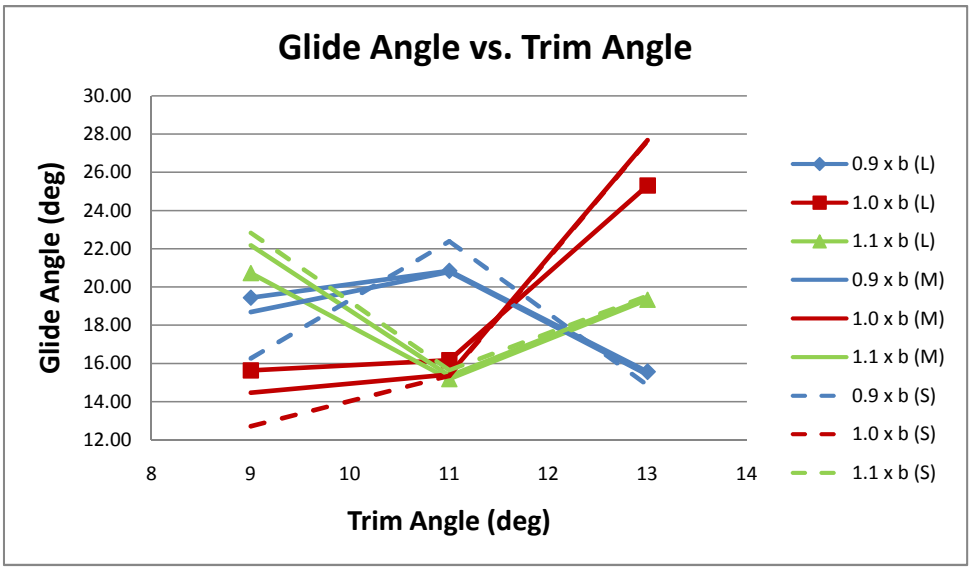

Figure 5.34: Glide Angle vs. Trim Angle in Turbulence

DOE Analysis

As before, the glide angle is first averaged according to the factor and level. For example, referring back to Table 5.17, the average absolute glide angle for the low level of trim angle in light turbulence is determined as follows:

$$\frac{19.44 + 15.63 + 20.72}{3} = 18.60^{\circ}$$

The same calculation was performed on the absolute and relative glide angles, under light, moderate and severe conditions, and these results are tabulated in Table 5.20. The orange and green highlighted rows correspond to the highlighted rows in Table 5.17, representing the low and high interaction effects respectively. Note that the no turbulence results are the same as the no wind case in the previous section.

Table 5.20: Factor and Interaction Effects on Glide Angle in Turbulence

Factor	**Level**	**Average Glide Angle (°)**						
		No Turb	*Light A*	*Light R*	*Mod A*	*Mod R*	*Sev A*	*Sev R*
A (Trim Angle)	−1	18.14	18.60	18.15	18.44	17.96	17.27	17.92
	0	19.14	17.39	19.18	17.19	19.21	17.80	19.18
	+1	20.37	20.07	20.30	20.84	20.38	20.68	20.41
B (Line Length)	−1	18.79	18.61	18.88	18.29	18.74	17.83	18.83
	0	19.23	19.03	19.11	19.19	19.14	18.57	19.02
	+1	19.64	18.41	19.63	18.99	19.68	19.33	19.65
A × B	−1	19.19	18.14	19.27	18.78	19.43	18.84	19.36
	+1	19.31	19.39	19.26	19.07	18.86	17.89	19.09

Now, to investigate the contribution the factor effects have on the absolute glide angle in turbulence, the following calculations were required:

Main effect of Trim Angle (A) on Absolute Glide Angle:

Focusing on the light turbulence condition, the average absolute glide angle was calculated when A is "−1" and when A is "+1" (refer to Table 5.20), and the average absolute glide angle variation from the low to high level of trim angle was determined as follows:

$$\frac{20.07 - 18.60}{1 - (-1)} = 0.73^{\circ}$$

The same procedure was followed for the moderate and severe cases. Data from Table 5.20 is illustrated in Figs. 5.35 - 5.37.

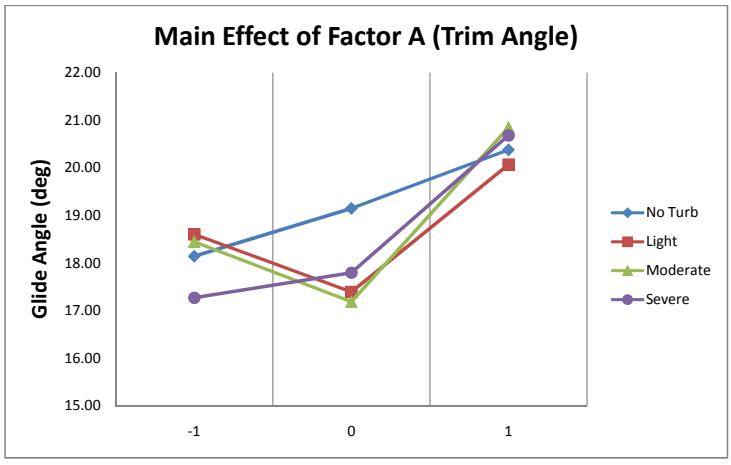

Figure 5.35: Main Effect of Trim Angle on Glide Angle in Turbulence

An interesting observation that should be noted from Fig. 5.35 is that for all four conditions (light, moderate, severe and no turbulence), the glide angle determined for the high level setting of trim angle are somewhat clustered together. The glide angle ranging from 20.07° – 20.84° in this region, whereas the "spreads" in glide angle in the low and intermediate level regions are greater.

Main effect of Plumb Line Length (B) on Absolute Glide Angle:

The average absolute glide angle of B (-1) in the light turbulence case was 18.61 and of B (+1) was 18.41 (refer to Table 5.20). Therefore, the absolute glide angle variation was:

$$\frac{18.41 - 18.61}{1 - (-1)} = -0.10^{\circ}$$

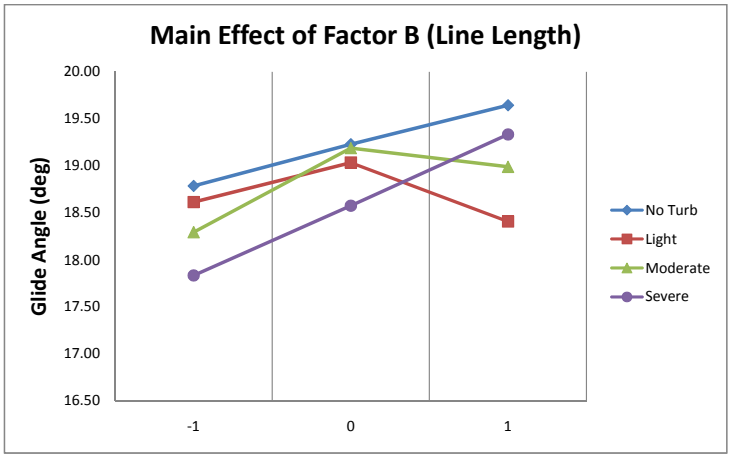

Figure 5.36: Main Effect of Plumb Line Length on Glide Angle in Turbulence

From Fig. 5.36, the spread in glide angle amongst the four conditions is the least in the intermediate level setting of plumb line length.

The Interaction of Factor A and B on Absolute Glide Angle:

Similarly, using the orange and green rows in Table 5.20, the absolute glide angle variation in the light turbulence case was:

$$\frac{19.39 - 18.14}{1 - (-1)} = 0.62^{\circ}$$

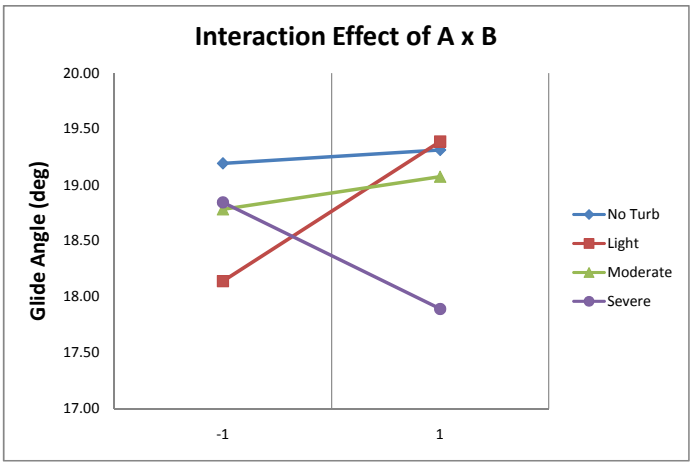

Figure 5.37: Interaction Effect of Trim Angle and Plumb Line Length on Glide Angle in Turbulence

The above results are tabulated in Table 5.21, where the magnitude of the slopes calculated is of importance. These values are required for the Pareto Chart in Fig. 5.38. Note that throughout this DOE analysis, the relative values were omitted and only the absolute glide angle from the extended simulations were analysed. Nevertheless, the next part of this section will focus on the error between the long and extended simulations for both the absolute and relative glide angle. From the Pareto Chart, it is evident that Factor A (Trim Angle) again contributes the most to the glide angle variability and sensitivity in all turbulence levels. The interaction effect in turbulent conditions however is not relatively small compared to the other two main effects, especially not in the light and severe turbulence cases. Also, in general the effects of the factors on glide angle become prominent in severe turbulent conditions.

Table 5.21: Contribution of All Effects on Glide Angle in Turbulence

Term	**Norm of Slope**						
	No Turb	*Light A*	*Light R*	*Mod A*	*Mod R*	*Sev A*	*Sev R*
A	1.12	0.73	1.07	1.20	1.21	1.70	1.24
B	0.43	0.10	0.37	0.35	0.47	0.75	0.41
A × B	0.06	0.62	0.01	0.15	0.29	0.48	0.14

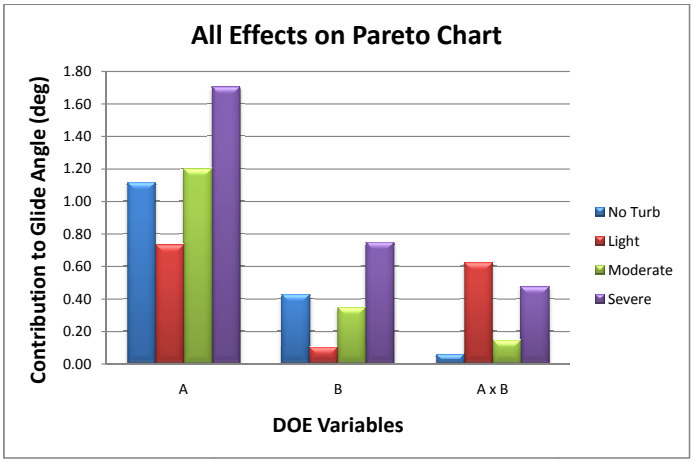

Figure 5.38: Pareto Chart of All Effects in Turbulence

DOE Analysis on Error

Similar to the Design of Experiments analyses conducted above, the errors between the long and extended simulations for both the absolute and relative glide angle were investigated. The error is first averaged according to the factor and level. For example, referring back to Table 5.19, the average error in absolute glide angle for the low level of trim angle in light turbulence is determined as follows:

$$\frac{9.38 + 6.78 + 0.14}{3} = 5.43\%$$

And like before, these results are tabulated in Table 5.22.

Table 5.22: Factor and Interaction Effects on Error in Turbulence

Factor	**Level**	**Average Error (%)**					
		Light A	*Light R*	*Mod A*	*Mod R*	*Sev A*	*Sev R*
A (Trim Angle)	−1	5.43	0.90	12.92	1.67	21.74	2.53
	0	3.80	0.88	3.01	1.79	17.62	2.01
	+1	2.65	1.11	9.02	0.98	7.15	0.60
B (Line Length)	−1	3.99	0.87	7.93	1.43	4.15	2.02
	0	5.39	1.10	10.54	1.76	22.91	1.68
	+1	2.51	0.92	6.48	1.25	19.44	1.44
A × B	−1	0.16	0.64	7.78	0.74	8.05	1.34
	+1	7.51	1.55	11.28	1.39	4.20	0.83

Now, to investigate the contribution the factor effects have on the absolute glide angle error in turbulence, the following calculations were required:

Main effect of Trim Angle (A) on Absolute Glide Angle Error:

Focusing on the light turbulence condition, the average absolute glide angle error was calculated when A is "−1" and when A is "+1" (refer to Table 5.22), and the average absolute glide angle error variation from the low to high level of trim angle was determined as follows:

$$\frac{2.65 - 5.43}{1 - (-1)} = -1.39\%$$

The same procedure was followed for the moderate and severe cases. Data from Table 5.22 is illustrated in Figs. 5.39 - 5.41.

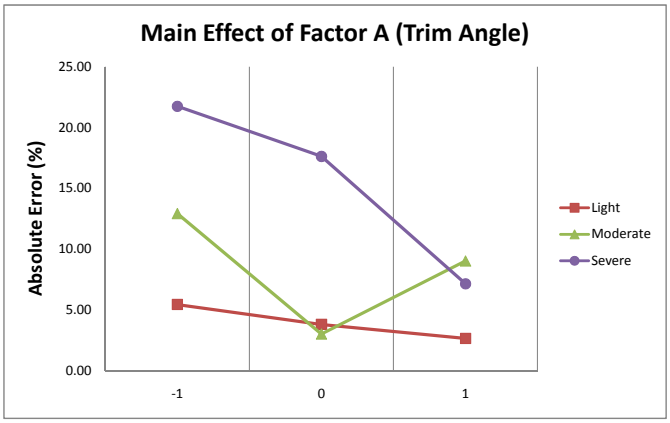

Figure 5.39: Main Effect of Trim Angle on Absolute Error in Turbulence

The spread of the absolute glide angle error between the long and extended simulations amongst the three turbulence levels is the least in the high level setting of trim angle and the most in the low level region, as illustrated in Fig. 5.39.

Main effect of Plumb Line Length (B) on Absolute Glide Angle Error:

The average absolute glide angle error of B (-1) in the light turbulence case was 3.99 and of B (+1) was 2.51 (refer to Table 5.22). Therefore, the absolute glide angle error variation was:

$$\frac{2.51 - 3.99}{1 - (-1)} = -0.74\%$$

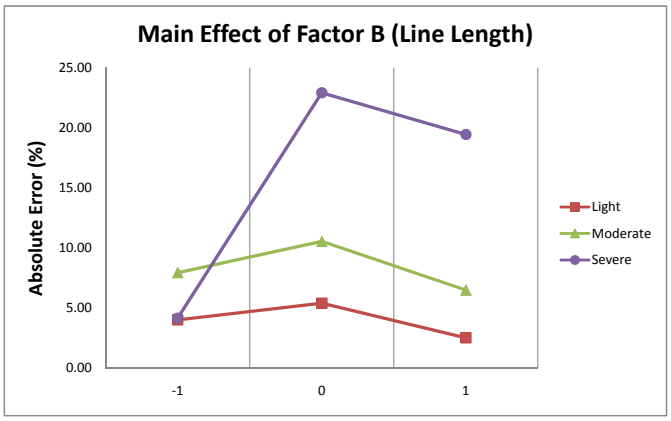

Figure 5.40: Main Effect of Plumb Line Length on Absolute Error in Turbulence

The spread of the absolute glide angle error between the long and extended simulations amongst the three turbulence levels is the least in the low level setting of plumb line length and the most in the intermediate level region, as illustrated in Fig. 5.40.

The Interaction of Factor A and B on Absolute Glide Angle Error:

Similarly, the absolute glide angle error variation in the light turbulence case was:

$$\frac{7.51 - 0.16}{1 - (-1)} = 3.67\%$$

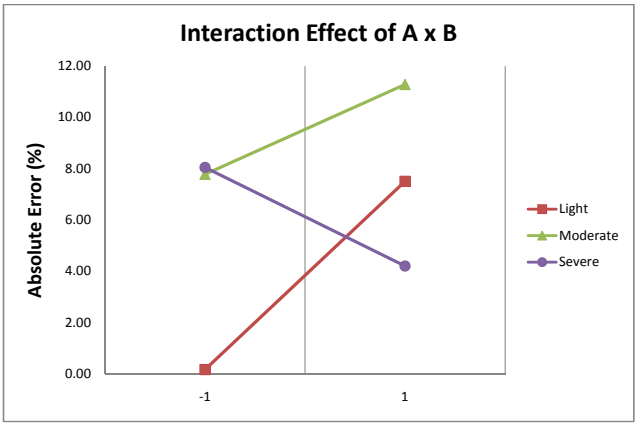

Figure 5.41: Interaction Effect of Trim Angle and Plumb Line Length on Absolute Error in Turbulence

The above results are tabulated in Table 5.23, where the magnitude of the slopes calculated is of importance. These values are required for the Pareto Chart in Fig. 5.42. The Pareto Chart looks slightly different to the Pareto Charts produced before in this section. For instance, the interaction effect of trim angle and plumb line length contributes more than the other two main effects to the absolute glide angle error in turbulence; particularly in light and moderate turbulent conditions. This is an important discovery, because although the interaction effect on absolute glide angle was generally smaller than the main effect of trim angle and the main effect of plumb line length (Refer to Fig. 5.38), the error between the long and extended simulations is higher in some cases (Also see Table 5.24). Recall that the DOE analysis of the previous section only took into account the absolute glide angle from the extended simulations. It is also evident from this chart that the method described at the start of Section 5.3.2 becomes less reliable in severe turbulence conditions, because the error on absolute glide angle increased when Factors A and B were changed.

Table 5.23: Contribution of All Effects on Error in Turbulence

Term	**Norm of Slope**					
	Light A	*Light R*	*Mod A*	*Mod R*	*Sev A*	*Sev R*
A	1.39	0.10	1.95	0.34	7.30	0.96
B	0.74	0.03	0.72	0.09	7.64	0.29
A × B	3.67	0.46	1.75	0.33	1.92	0.26

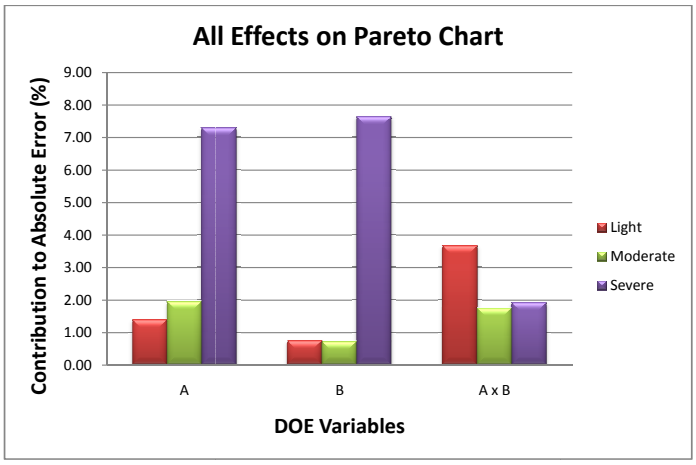

Figure 5.42: Pareto Chart of All Effects on Absolute Error in Turbulence

Now, to investigate the contribution the factor effects have on the relative glide angle error in turbulence, the following calculations were required:

Main effect of Trim Angle (A) on Relative Glide Angle Error:

Focusing on the light turbulence condition, the average relative glide angle error was calculated when A is "−1" and when A is "+1" (refer to Table 5.22), and the average relative glide angle error variation from the low to high level of trim angle was determined as follows:

$$\frac{1.11 - 0.90}{1 - (-1)} = 0.10\%$$

The same procedure was followed for the moderate and severe cases. Data from Table 5.22 is illustrated in Figs. 5.43 - 5.45.

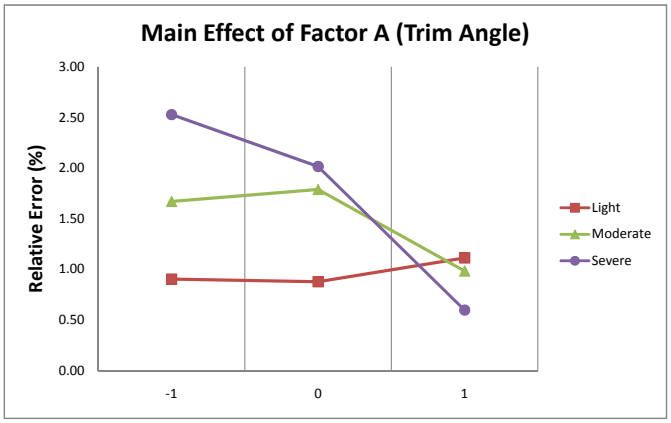

Figure 5.43: Main Effect of Trim Angle on Relative Error in Turbulence

The spread of the relative glide angle error, like the absolute glide angle error, between the long and extended simulations amongst the three turbulence levels is the least in the high level setting of trim angle and the most in the low level region, as illustrated in Fig. 5.43.

Main effect of Plumb Line Length (B) on Relative Glide Angle Error:

The average relative glide angle error of B (-1) in the light turbulence case was 0.87 and of B (+1) was 0.92 (refer to Table 5.22). Therefore, the absolute glide angle error variation was:

$$\frac{0.92 - 0.87}{1 - (-1)} = 0.03\%$$

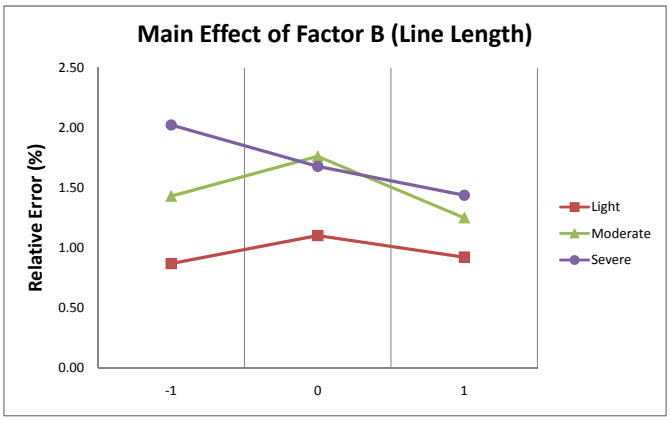

Figure 5.44: Main Effect of Plumb Line Length on Relative Error in Turbulence

Unlike the spread of the absolute glide angle error, the spread of the relative glide angle error between the long and extended simulations amongst the three turbulence levels is the most in the low level setting of plumb line length and the least in the high level region, as illustrated in Fig. 5.44.

The Interaction of Factor A and B on Relative Glide Angle Error:

Similarly, the relative glide angle error variation in the light turbulence case was:

$$\frac{1.55 - 0.64}{1 - (-1)} = 0.46\%$$

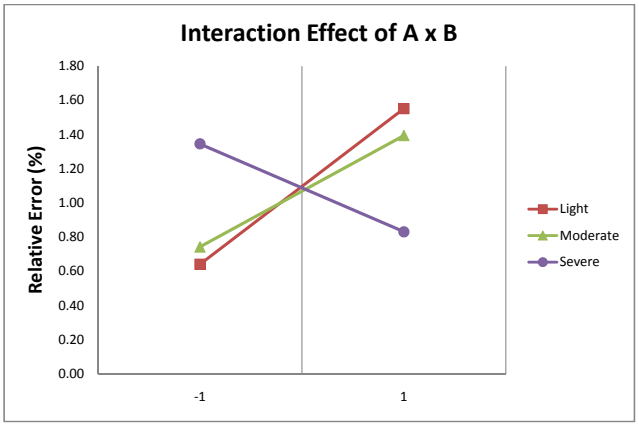

Figure 5.45: Interaction Effect of Trim Angle and Plumb Line Length on Relative Error in Turbulence

The above results are tabulated in Table 5.23, where the magnitude of the slopes calculated is of importance. These values are required for the Pareto Chart in Fig. 5.46. The Pareto Chart looks similar to that of the one presented by Fig. 5.42 and the same information can be deduced from it. However, notice that the magnitude of the contribution to relative error is significantly less than the magnitude of the contribution to absolute error (See Table 5.24).

Table 5.24 is essentially a summary of the results from the DOE analyses in this section. The results can be interpreted as follows: Under light turbulence, a change from the low to high level of trim angle (Factor A) has a 0.73° variability (Table 5.21) on a nominal settled absolute glide angle, with an associated error variability of 1.39% (Table 5.23). The same notion can be extended to the other terms for absolute and relative glide angle under all three turbulence conditions. To conclude, the trim angle effect and plumb line length effect on absolute glide angle is most prominent under severe turbulent conditions. In addition, the error in the method is greatest here. The interaction effect on absolute glide angle is most prominent under light turbulent conditions and the error in the method is greatest here too.

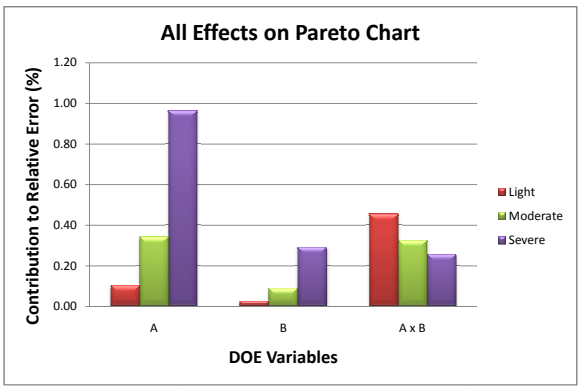

Figure 5.46: Pareto Chart of All Effects on Relative Error in Turbulence

Table 5.24: Summary of Turbulence Results

Term	**Glide Angle (°)**					
	Light A	*Light R*	*Mod A*	*Mod R*	*Sev A*	*Sev R*
A	0.73 (1.39%)	1.07 (0.10%)	1.20 (1.95%)	1.21 (0.34%)	1.70 (7.30%)	1.24 (0.96%)
B	0.10 (0.74%)	0.37 (0.03%)	0.35 (0.72%)	0.47 (0.09%)	0.75 (7.64%)	0.41 (0.29%)
A × B	0.62 (3.67%)	0.01 (0.46%)	0.15 (1.75%)	0.29 (0.33%)	0.48 (1.92%)	0.14 (0.26%)

Chapter 6

Conclusions and Recommendations

6.1 Conclusions

Based on the foregoing results, the following conclusions have been drawn.

6.1.1 Experimental Flight Tests were Unsuccessful

Conducting flight tests seemed to be more challenging than it had initially been expected. The strong south-easterly winds, notorious to Cape Town throughout the summer months, hampered the progress of flight tests. Relatively calm days to conduct tests were few and far between, and sometimes the wind would begin to pick up during testing, forcing the tests to be cancelled. The biggest challenge the wind presented was in setting up the parafoil launcher for a successful launch. When the wind was slightly gusty, the parafoil canopy would accidentally shift along the crossbar, or fold on itself, and hence the canopy would not inflate as intended to as the launch arm rotated around.

As a result of this, the testing matrix proposed could not be completed and not nearly enough IMU data was logged from the flight tests. Therefore, a proper DOE analysis on how the trim settings affect the system's glide angle could not be done. Even during the preliminary flight tests discussed in Section 5.1, IMU data was only logged for a single flight due to some technical issues regarding battery power to the avionics equipment. Although a surveyor accurately measured the launch and landing coordinates after each flight, this was not sufficient in accurately determining a settled glide angle because the parafoil-payload system displayed a prominent phugoid mode

during flight. The IMU data logged from the single flight in the preliminary testing shows good correlation with preliminary simulations, however a larger sample of IMU data would be required to make any reasonable comparisons.

In addition, the experimental flight tests brought about damages to equipment. Most noticeable damages occurred to the parafoil-payload system. Due to the nature of the surroundings where the tests were conducted, the parafoil canopy often ripped and tore on sharp rock edges, and suspension lines broke. The payload box also suffered damages due to hard landings on occasions. These hard landings would eventually take its toll on the delicate avionics equipment inside the payload box, and it was not long before it was discovered that the IMU had been damaged.

Besides the few useful observations from the experimental flight tests that aided with the fulfilment of the simulations, the flight tests were rather disappointing and yielded unsatisfactory results. This meant that the focus of this investigation shifted to simulated results rather than experimental results, and that conducting only experimental flight tests with the current set-up is deemed an unsuccessful method in determining the optimum trim setting of the parafoil-payload system.

6.1.2 Positive Relationship between Plumb Line Length and Glide Angle

Determining a direct relationship between plumb line length and glide angle from the above simulations is not as straight forward as one might assume, especially in turbulent atmospheric conditions. In still and mean wind conditions, an increase in plumb line length results in an increase in glide angle, and the positive relationship between the two is linear (Refer to Figs. 5.17 and 5.20). This relationship is substantiated by the preliminary experimental flight tests results presented in Section 5.1. Referring to Fig. 5.3, it is shown that the horizontal distance the parafoil-payload system covered during flight decreased as the plumb line length varied from the low to high level setting. Hence, from the Pythagorean relationship between glide slope and the ratio of vertical to horizontal distance, if the horizontal distance travelled decreased for the same given height then the glide angle must have increased.

Increasing the plumb line length of the parafoil increases the drag component of the lines and hence the total drag force on the system. This is undoubtedly the reason for the increase in glide angle and decrease in the

horizontal distance travelled during flight. With respect to the atmospheric turbulence case simulated in Section 5.3.2, the relationship between plumb line length and glide angle is not as clear as in the still and mean wind simulations. Referring to Fig. 5.36, it can be seen that this relationship is not as linear as before, particularly under light and moderate turbulence. In these two cases, the glide angle increases as the plumb line length is increased from the low to intermediate level setting, but then decreases when the plumb line length is increased further to the high level setting. However, the general trend is still that of a positive one for the moderate turbulence case, but unfortunately not so for the light turbulence case. This small discrepancy and the non linearity observed in the results is most probably a result of the random nature in which turbulence was modelled.

6.1.3 Positive Relationship between Trim Angle and Glide Angle

It is evident from the above simulations that glide angle is proportional to the trim angle of the parafoil system. By rigging the parafoil-payload system in such a way that the trim angle increases, the resultant glide angle during steady flight will in turn increase. With respect to still and mean wind conditions simulated in Section 5.3.1, this positive linear relationship is shown in Figs. 5.18 and 5.19. Although the relationship between trim angle and glide angle is again not as linear in the atmospheric turbulence case simulations, the general trend is also positive, i.e. the glide angle increases as the trim angle is increased from the low to high level setting (Refer to Fig. 5.35).

This relationship can be explained as follows: An increase in the trim angle results in an increase in the parafoil's canopy angle of attack, which in turn increases the resultant lift. Ignoring the zero lift drag coefficient (C_{D0}), the induced drag will approximately increase quadratically due to this increase in lift, and thus the lift-to-drag ratio decreases. A decrease in the lift-to-drag ratio will therefore increase the glide angle, as illustrated by the results. To conclude, over the trim setting ranges tested, varying the trim angle has a greater influence on glide angle than varying the plumb line length. This is apparent in all conditions (still, mean wind and turbulent conditions) simulated, and is illustrated by the Pareto charts in Figs. 5.22 and 5.38. In fact, on average trim angle has a 2-3 times greater effect on glide angle than plumb line length, because the contribution to glide angle variability and sensitivity is 2-3 times bigger when changing from the low to the high level setting of the two respective factors.

6.1.4 The Effect of Mean Wind

The effect a mean wind has on the parafoil-payload system is as expected, hence flying directly into a headwind decreases the distance travelled for a given height drop. Therefore, the steady state glide angle increases. Compared to still conditions, the velocity component due to a headwind increases the relative velocity of the system. The converse is true when flying with a tailwind directly behind the system, that is, the distance travelled increases for a given height drop and the steady state glide angle decreases. This result is clearly illustrated in Figs. E.1 and E.2, and referring to Table 5.14, a mean headwind of 1 m/s results in an average increase of 3.58° (22.80° − 19.22°) on glide angle. A mean tailwind of 1 m/s results in an average decrease of 2.73° (19.22° − 16.59°) on glide angle.

By considering the parafoil-payload motion as seen by an observer moving with the wind, the glide angle in the observer's frame of reference is independent of wind speed, therefore the settled glide angle is equal to that of the settled glide angle under still conditions. As a check, the calculation of "relative" glide angle in Section 5.3.1 illustrates this point (Also refer to Fig. E.3 and Table 5.14).

6.1.5 The Effect of Atmospheric Turbulence

Isolating the effect of atmospheric turbulence on glide angle is harder than the effect of mean wind. Due to the stochastic nature of turbulence, the turbulent gust velocities can either hinder or assist the parafoil-payload system's flight. Therefore, the glide angle will vary with time, sometimes increasing and sometimes decreasing, depending on the random conditions. This also makes it more difficult to determine a settled glide angle for a given trim setting of plumb line length and trim angle (See Figs. E.11 and E.12).

Observations that can be deduced from the simulated results, but not necessarily conclusive ones because atmospheric turbulence is a random process, is how much the turbulence intensities affect the average glide angle for a given trim setting. Referring to Fig. 5.35, the average glide angle changes very little for the high level setting of trim angle (13°) under light, moderate and severe turbulence. Thus, it can be said that the effects of atmospheric turbulence on average glide angle are less noticeable for the high level setting of trim angle. Similarly, referring to Fig. 5.36, the effects of atmospheric turbulence on average glide angle are less noticeable for the intermediate level setting of plumb line length ($1 \times b$).

6.1.6 The Effectiveness of Extended Trajectory Simulations

The extended trajectory simulations described in the atmospheric turbulence case (Section 5.3.2) indicate how accurate an estimate of glide angle can be obtained by conducting experimental flight tests in the quarry. As mentioned before, the experimental flight tests were relatively unsuccessful and due to the lack of height in the quarry, a reasonably settled glide angle could not be determined. Therefore, by measuring the impact point and prevailing conditions, a simulation is run using the measured conditions as the initial conditions to the simulation in an attempt to extend the trajectory to a steady state. The success of these extended simulations depend on how well they agree with the "longer" simulations under the same atmospheric conditions. The long simulations are assumed to be the flight of the parafoil-payload system during the experimental flight test provided that height was not a limitation.

As expected, the error on glide angle between the long and extended simulations increase as the turbulence intensities increases. Referring to Table 5.19, under light turbulence there is a maximum error of 9.38% in the calculation of absolute glide angle, and 1.66% in the calculation of relative glide angle. Similarly, under moderate turbulence there is a maximum error 15.45% and 3.32% in the calculation of absolute and relative glide angle respectively. Under severe turbulence, the maximum error is even greater at 47.97% and 4.67% in the calculation of absolute and relative glide angle respectively. The DOE analysis on error reiterates this point and with respect to the trim settings, the average error on absolute and relative glide angle is least for the high level setting of trim angle (See Figs. 5.39 and 5.43). The average error on absolute glide angle is least for the low level setting of plumb line length, however the average error on relative glide angle is least for the high level setting of plumb line length (See Figs. 5.40 and 5.44 respectively).

Therefore, to conclude, averaging the error on glide angle between the long and extended simulations according to the trim setting and level shows how accurate an estimate of glide angle can be obtained from this method, assuming that the long simulations are equivalent to the experimental flight tests. Thus, referring to Table 5.22, under light turbulence there is a maximum average error on absolute glide angle of 7.51% corresponding to the high variation of the factor interaction. Under moderate turbulence there is a maximum average error on absolute glide angle of 12.92% corresponding to the low level setting of trim angle, and under severe turbulence there is a

maximum average error on absolute glide angle of 22.91% corresponding to the intermediate level setting of plumb line length. Considering that the average absolute glide angle varies roughly between $17^\circ - 21^\circ$ (see Table 5.20), the average estimate of absolute glide angle from the extended trajectory simulations can be inaccurate by up to $1.6^\circ - 4.8^\circ$ depending on the conditions and the trim settings.

Now one might be tempted to say that the extended trajectory simulations are ineffective in accurately estimating glide angle after conducting a flight test in the quarry because of these large discrepancies. However, keeping in mind that experimental flight tests were limited to days where the wind speeds did not exceed 5 m/s, and that the parafoil-payload system was launched at speeds of 10 m/s. Under light, moderate and severe turbulence, the wind velocity at 20 feet (6 m) above the ground is assumed to be 7.7 m/s, 15.4 m/s and 23.15 m/s respectively. A flight test in the quarry would never be conducted under any of these turbulent conditions, especially not in moderate and severe turbulence, because the wind speeds at 20 feet would even exceed the launch speed. Therefore, the errors mentioned above are not indicative of the actual conditions in which flight tests would be conducted in the quarry. Ideally, the average estimate of absolute glide angle from the extended trajectory simulations would be at most, and in most cases significantly less than 1° ($5/7.7 \times 1.6^\circ$) inaccurate. Thus, the extended trajectory simulations can effectively estimate a settled glide angle for a given trim setting to within 1°.

6.1.7 DOE and Flight Tests were Ineffective in Determining Optimum Glide Performance

Optimum glide performance relates to a minimum glide angle, therefore for a given height drop the furthest distance travelled. From the results of this investigation, it is evident that if the trim angle and the plumb line length is increased, a steeper glide slope is produced (i.e. a bigger glide angle). Conversely, if the trim angle and the plumb line length is decreased then a shallower glide slope is produced. There should exist a trim setting corresponding to this *optimum* but it seems to have fallen outside the range of trim settings selected for the simulations (trim angle of $9^\circ - 13^\circ$ and plumb line length of $0.9 - 1.1 \times b$). The preliminary flight tests (see Section 5.1) suggest that this is the case, as a trim angle setting of 7° resulted in the parafoil stalling, in agreement with Iosilevskii [24] (refer to page 18). Recall that a smaller trim angle results in a more rear CG position.

Although only a few of the aspects regarding Design of Experiments mentioned in Section 2.4 were actually implemented in this investigation, DOE proved to be a useful technique in isolating the main factor and interaction effects. As mentioned before, on average the trim angle has a 2-3 times greater effect on glide angle than plumb line length, and because the interaction effect between these two factors is relatively small, trim angle is the driving factor if a change in glide slope is required. However, despite this point, the DOE approach adopted in this investigation was still inconclusive in determining an optimum glide angle because the range of trim settings selected for the simulations was inadequate.

6.2 Recommendations

On the basis of the above conclusions, the following recommendations are made:

6.2.1 Conduct further Flight Tests and Simulations

Undoubtedly more experimental flight tests need to be conducted in future work because of the relatively unsuccessful flight tests conducted in this investigation. It is recommended though that a better location be chosen for the experimental flights, as the quarry caused numerous issues. A location that allows for greater height drops would be ideal, and in addition a location where the surroundings are less harsh would reduce damage to the payload box and parafoil canopy. It is also recommended that the flight tests be conducted in Cape Town's winter months, because in summer the winds are too strong for successful launches. A launch site with a suitable topography that allows the azimuth to be changed to enable launching directly into the wind would assist greatly in determining glide slope more accurately on windy days, however it is still preferred that flight tests be done in winter when there is less wind.

In conducting further experimental flight tests, it is suggested that a differential GPS of higher accuracy be implemented, hence work would need to be done on the IMU. Conducting further flight tests would result in a much larger data sample being available for reasonable comparisons to be made with the simulations. Hence, DOE techniques could be utilised more in future work. For example, controlled flight tests could be performed, where the electronic steering unit could execute brake deflections in flight. A DOE

analysis could then be run to investigate the effect this extra factor (brake deflection) has on glide slope. Alternatively, instead of increasing the number of factors or levels, it might be worthwhile to reduce the number of levels for each factor from say three to two and rather increase the number of repeated measurements for each run. One run could be repeated numerous times to determine how many measurements are needed for the mean and standard deviation to settle down to within a reasonable accuracy. Perhaps parafoil canopies of different shapes and sizes could be tested too, although this would require some modifications to the current parafoil launcher and much more time.

In addition, the simulations (and flight tests) could be repeated with different factor levels of trim setting in order to pinpoint the optimum glide performance. It may be that the optimum cannot be found, as one might run into a minimum stability limit or into the stall limit as the CG position moves to far forward or to far backward respectively when adjusting the trim settings, as mentioned by Iosilevskii [24] (refer to page 18). It might turn out that a purely experimental approach is impractical and that experimentation should be directed at calibrating the simulation of flight model, and apply the model for predicting optimum values, which can then be verified with experimental flight tests.

6.2.2 Determine Aerodynamic Coefficients from IMU and Photography more Accurately

Ideally, with the aid of more accurate IMU data and more precise photography, the aerodynamic coefficients of the parafoil can be derived to better characterise the system. A better analysis of the drag polar could also be conducted with more accurate data, this would assist in attempting to infer optimum glide slope too. This would be beneficial to both experimental flight tests and simulations, especially the latter, because models and algorithms with greater fidelity could be developed. If the system is in steady state glide, aerodynamic coefficients of the parafoil such as: C_{L0}, C_{D0}, C_{m0}, $C_{L\alpha}$ and $C_{m\alpha}$ can be determined as documented in Appendix F.

6.2.3 Implement Mechanism to Dynamically change Trim Settings

The current experimental set-up only allows for varying the trim settings before a flight test. Therefore, after launch, the combination of trim angle

and plumb line length is fixed throughout the parafoil-payload system's flight. Having the ability to dynamically change the trim settings in flight would have a direct response on the glide performance, and a certain level of control would be gained when attempting to land at a predetermined site; if sudden atmospheric disturbances occurred. Of course, changing the trim settings in flight is outside the scope of this investigation, but future work could include a small design project to develop and implement a mechanism that could adjust the trim angle and plumb line length during flight.

6.2.4 Develop Higher Order Simulation Models

In addition to repeating the simulations, as mentioned above, it is recommended that higher order models be developed where both the longitudinal and lateral dynamics of the parafoil-payload system be explored. The current algorithm only focuses on the longitudinal motion of the system and a relatively rudimentary 4-DOF model was implemented. Although not necessarily a priority, if more time was available, a more comprehensive 6-DOF or 9-DOF model could be developed, increasing the accuracy of the simulations. If desired, some aspects of control could be implemented too, where both asymmetric and symmetric brake deflections could be simulated, and the effects on longitudinal and lateral motion investigated.

References

[1] J. S. Lingard. The Aerodynamics of Gliding Parachutes. In *AIAA Paper 1986-2427, 9th Aerodynamic Decelerator and Balloon Technology Conference*, Albuquerque, October 1986.

[2] D. Toohey. Development of a Small Parafoil Vehicle for Precision Delivery. Master's thesis, Massachusetts Institute of Technology, June 2005.

[3] J. S. Lingard. Ram-air Parachute Design. In *Precision Aerial Delivery Seminar, 13th AIAA Aerodynamic Decelerator Systems Technology Conference*, Clearwater Beach, May 1995.

[4] H. L. Morgan Jr. Performance and Deployment Characteristics of a Twin-Keel Parawing with Various Amounts and Permeabilities of Porous Material in Outer Lobes. Technical report, NASA Langley Research Center, NASA TN D-5793, Washington D.C., 1970.

[5] O. Prakash. Aerodynamics, Longitudinal Stability and Glide Performance of Parafoil/Payload System. Master's thesis, Preliminary Project Report, Department of Aerospace Engineering, Indian Institute of Technology, Bombay, August 2004.

[6] J. D. Nicolaides and M. A. Tragarz. Parafoil Flight Performance. Technical report, DTIC Document, Wright-Patterson Air Force Base, Ohio, June 1971.

[7] H. Altmann. Numerical Simulation of Parafoil Aerodynamics and Dynamic Behaviour. In *20th AIAA Aerodynamic Decelerator Systems Technology Conference and Seminar*, Seattle, Washington, May 2009.

[8] M. C. Butler. Basic Performance, Design and Construction of Ram-Air Inflated Gliding Parachute Wings. Technical report, NAVAL WEAPONS CENTER, China Lake, CA, April 1986.

[9] J. Sobieski. The Aerodynamics and Piloting of High Performance Ram-Air Parachutes. Master's thesis, University of Maryland Institute for Advanced Computer Studies, College Park, MD, United States, May 1994.

[10] G. Guglieri. Parachute-Payload System Flight Dynamics and Trajectory Simulation. *International Journal of Aerospace Engineering*, 2012.

[11] B. J. Rademacher. *In-Flight Trajectory Planning and Guidance for Autonomous Parafoils*. PhD thesis, Iowa State University, Ames, Iowa, 2009.

[12] C Matos, R Mahalingam, G Ottinger, J Klapper, R Funk, and N Komerath. Wind Tunnel Measurements of Parafoil Geometry and Aerodynamics. In *36th AIAA Aerospace Sciences Meeting, AIAA Paper 98-0606*, Reno, NV, January 1998.

[13] G. J. Brown. Tethered Parafoil Test Technique. In *AIAA Aerodynamic Decelerator Systems Technology Conference, 10 th, Cocoa Beach, FL*, pages 110–113, 1989.

[14] N. J. Slegers. Effects of Canopy-Payload Relative Motion on Control of Autonomous Parafoils. *Journal of Guidance, Control, and Dynamics*, Volume 33(1):116, 2010.

[15] M. Ward. *Adaptive Glide Slope Control for Parafoil and Payload Aircraft*. PhD thesis, Georgia Institute of Technology, May 2012.

[16] A. Gavrilovski, M. Ward, and M. Costello. Parafoil Glide Slope Control Using Canopy Spoilers. In *21st AIAA Aerodynamic Decelerator Systems Technology Conference and Seminar*, 2011.

[17] N. Slegers, E. Beyer, and M. Costello. Use of Variable Incidence Angle for Glide Slope Control of Autonomous Parafoils. *Journal of Guidance, Control, and Dynamics*, Volume 31(3):585, 2008.

[18] M. Ward, A. Gavrilovski, and M. Costello. Flight Test Results for Glide Slope Control of Parafoil Canopies of Various Aspect Ratios. In *21st AIAA Aerodynamic Decelerator Systems Technology Conference and Seminar, Dublin, Ireland*, 2011.

[19] D. Wolf. The Dynamic Stability of a Nonrigid Parachute and Payload System. *Journal of Aircraft*, Volume 8(8):603–609, 1970.

[20] N. Slegers and M. Costello. On the Use of Rigging Angle and Canopy Tilt for Control of a Parafoil and Payload System. In *AIAA Atmospheric Flight Mechanics Conference and Exhibit, Austin, Texas*, pages 11–14, 2003.

[21] B. E. Tweddle. Simulation and Control of Guided Ram Air Parafoils. Master's thesis, University of Waterloo, Department of Electrical and Computer Engineering, Waterloo, Ontario, Canada, August 2006.

[22] H. Ashley. *Engineering Analysis of Flight Vehicles*. DoverPublications, 1992.

[23] S. Müller. *Modellierung, Stabilität und Dynamik von Gleitschirmsystemen*. Herbert Utz Verlag, München, 2002.

[24] G. Iosilevski. Centre of Gravity and Minimal Lift Coefficient Limits of a Gliding Parachute. *Journal of Aircraft*, Volume 32(6):1297–1302, 1995.

[25] C. Redelinghuys and S. Rhodes. A Graphic Portrayal of Parafoil Trim and Static Stability. *AIAA Paper*, 2561, 2007.

[26] O. Prakash, A. Daftary, and N. Ananthkrishnan. Trim and Stability Analysis of Parafoil/Payload System using Bifurcation Methods. In *AIAA 18th Aerodynamic Decelerator Systems Technology Conference and Seminar, AIAA*, 2005.

[27] N. Slegers and M. Costello. Model Predictive Control of a Parafoil and Payload System. *Journal of Guidance, Control, and Dynamics*, 28(4):816–820, 2005.

[28] T. F. Goodrick. Theoretical Study of the Longitudinal Stability of High-Performance Gliding Airdrop Systems. In *American Institute of Aeronautics and Astronautics, Aerodynamic Deceleration Systems Conference, 5th, Albuquerque, N. Mex*, November 1975.

[29] C. M. Gorman and N. J. Slegers. Modeling of Parafoil-Payload Relative Yawing Motion on Autonomous Parafoils. In *21st AIAA Aerodynamic Decelerator Systems Technology Conference and Seminar, Dublin, Ireland*, 2011.

[30] C. Toglia and M. Vendittelli. Modeling and Motion Analysis of Autonomous Paragliders. *Department of Computer and System Sciences Antonio Ruberti Technical Reports*, Volume 2(5), 2010.

[31] C. Redelinghuys. A Flight Simulation Algorithm for a Parafoil Suspending an Air Vehicle. *Journal of Guidance, Control, and Dynamics*, Volume 30, 2007.

[32] O. A. Yakimenko. On the Development of a Scalable 8-DoF Model for a Generic Parafoil-Payload Delivery System. In *18th AIAA Aerodynamic Decelerator Systems Technology Conference and Seminar, American Institute of Aeronautics and Astronautics*, 2005.

[33] K-F Doherr and H Schilling. 9 DOF-Simulation of Rotating Parachute Systems. In *AIAA Aerodynamic Decelerator Systems Technology Conference, 11 th, San Diego, CA*, pages 333–343, 1991.

[34] N. Slegers and M. Costello. Aspects of Control for a Parafoil and Payload System. *Journal of Guidance, Control, and Dynamics*, Volume 26(6):898–905, 2003.

[35] O. Prakash and N. Ananthkrishnan. Modeling and Simulation of 9-DOF Parafoil-Payload System Flight Dynamics. In *AIAA Atmospheric Flight Mechanics Conference and Exhibit*. Indian Institute of Technology, Bombay, Mumbai, India, 2006.

[36] B. Etkin. Dynamics of Atmospheric Flight, 1972.

[37] E. Simiu and R. H. Scanlan. *Wind Effects on Structures: An Introduction to Wind Engineering*. John Wiley, 1986.

[38] T. R. Oke. *Boundary Layer Climates*. Methuen and Co. Ltd., 1978.

[39] Flying Qualities of Piloted Airplanes, U.S. Military Handbook MIL-HDBK-1797, 19 December 1997.

[40] Flying Qualities of Piloted Airplanes, U.S. Military Specification MIL-F-8785C, 5 November 1980.

[41] D. Phair. An Investigation into the Influence of Various System Characteristics and Environmental Factors on Autonomous Parafoil Impact Accuracy and Dynamics. Master's thesis, School of Engineering, University of Glasgow, 2014.

[42] S. Gage. Creating a Unified Graphical Wind Turbulence Model from Multiple Specifications. In *American Institute of Aeronautics and Astronautics (AIAA) 2003 Modeling and Simulation Technologies Conference and Exhibit*, 2003.

[43] T. R. Beal. Digital Simulation of Atmospheric Turbulence for Dryden and von Karman Models. *Journal of Guidance, Control, and Dynamics*, 16(1):132–138, 1993.

[44] J. C. Yeager. Implementation and Testing of Turbulence Models for the F18-HARV Simulation. *Lockheed Martin Engineering & Sciences, NASA CR-1998-206937*, 1998.

[45] J. M. Stein, C. M. Madsen, and A. L. Strahan. An Overview of the Guided Parafoil System Derived from X-38 Experience. In *Proceedings of the 18th AIAA Aerodynamic Decelerator Systems Technology Conference and Seminar*, 1999.

[46] P. D. Hattis and R. Benney. Demonstration of Precision Guided Ram-Air Parafoil Airdrop Using GPS/INS Navigation. In *Proceedings of the 52nd Annual Meeting of The Institute of Navigation*, Cambridge, MA, June 1996.

[47] T. Yatoh, Y. Hiroki, I. Shida, S. Sagara, and K. Yonemoto. Navigation, Guidance and Control of Parafoil Recovery System for KIT Experimental Rocket. In *Proceedings of the 2006 KSAS-JSASS Joint International Symposium on Aerospace Engineering, Busan, Korea*, pages 6–11, 2006.

[48] J. E. Murray, A. G. Sim, D. C. Neufeld, P. K. Rennich, S. R. Norris, and W. S. Hughes. *Further Development and Flight Test of an Autonomous Precision Landing System using a Parafoil*. National Aeronautics and Space Administration, Office of Management, Scientific and Technical Information Program, California, 1994.

[49] K. Hiraki and M. Inoue. Development of Autonomous Flight Systems with Small Parafoil. In *20th AIAA Aerodynamic Decelerator Systems Technology Conference and Seminar*, Seattle, Washington, May 2009.

[50] N. J. Slegers and O. A. Yakimenko. Optimal Control for Terminal Guidance of Autonomous Parafoils. In *20th AIAA Aerodynamic Decelerator Systems Technology Conference and Seminar*, Seattle, Washington, May 2009.

[51] G. Hope and C. Kennell. Logistics Enabler for Distributed Forces. Technical report, DTIC Document, 2004.

[52] J. Milgram, J. Strickland, A. Macander, and G. Hunter. Autonomous Glider Systems for Logistics Delivery. In *AUVSI (Associated for Unmanned Vehicle Systems International) 2003 Unmanned Systems Sym-*

posium and Exposition, Baltimore Convention Center, Baltimore, Maryland, 2003.

[53] N. A. Doyle. Design and Development of a UAV Recovery System for use on RAN Patrol Boats. *The UNSW Canberra at ADFA Journal of Undergraduate Engineering Research*, Vol 3, No 2, 2010.

[54] A. S. Puranik. *Dynamic Modeling, Simulation and Control Design of a Parafoil-Payload System for Ship Launched Aerial Delivery System (SLADS)*. PhD thesis, Michigan Technological University, United States – Michigan, 2011.

[55] M. A. Kolodny. Initial Experiment in Using a Powered Parafoil for Employment of Intelligence, Surveillance, and Reconnaissance (ISR) Unattended Ground sensors (UGS). Technical report, DTIC Document, 2004.

[56] D. J. DeTurris, J. C. Ervin, and S. E. Alptekin. Development of an Autonomous Tactical Reconnaissance Platform. *Journal of Aerospace Computing, Information, and Communication*, 4(6):865–881, 2007.

[57] H. J. Liberman. Cannon Launched Reconnaissance Vehicle, 1995. US Patent 5,467,681.

[58] A. J. Grunwald, C. Redelinghuys, S. Rhodes, W. Norton, J. Adams, T. Booysen, and J. Pead. Reconfigurable Flight Testing System for Parafoils - Design Considerations and Phases of Development of a Remotely Controlled Parafoil System. Technical report, University of Cape Town, 2012.

[59] J. D. Anderson Jr. *Fundamentals of Aerodynamics*. McGraw-Hill, 5th edition, 2011.

[60] R. H. Geiger and W. K. Wailes. Advanced Recovery Systems Wind Tunnel Test Report. Technical report, DTIC Document, 1990.

[61] Minitab INC. Minitab user's Guide 2: Design of Experiments, 2003.

[62] S. D. Bolboacă and L. Jäntschi. Design of Experiments: Useful Orthogonal Arrays for Number of Experiments from 4 to 16. *Entropy*, Volume 9(4):198–232, 2007.

[63] L. Ilzarbe, M. J. Álvarez, E. Viles, and M. Tanco. Practical Applications of Design of Experiments in the Field of Engineering: A Bibliographical Review. *Quality and Reliability Engineering International*, Volume 24(4):417–428, February 2008.

[64] R. DeLoach. The Modern Design of Experiments for Configuration Aerodynamics: A Case Study. In *44th AIAA Aerospace Sciences Meeting and Exhibit, Reno, NV, USA*, 2006.

[65] L. L. Bordelon. Design of Experiments Applied to Flight Testing. *Mission Systems Engineering*, Volume 3:1–12 Educational Notes, 2006.

[66] D. Fletcher. An Investigation of Taguchi Methods for Flight Test Optimization. In *AIAA, Biennial Flight Test Conference, 7 th, Colorado Springs, CO*, pages 287–292, 1994.

[67] R. A. Fisher. *The Design of Experiments*. Oliver and Boyd, Edinburgh: Tweeddale Court London: 90 Great Russell Street, W.C., 6th edition, 1951.

[68] D. R. Cox. *Planning of Experiments*. John Wiley & Sons, INC, 1958.

[69] C. R. Hicks. *Fundamental Concepts in the Design of Experiments*. Oxford University Press, INC, New York, 4th edition, 1993.

[70] K. Hinkelmann and O. Kempthorne. *Design and Analysis of Experiments, Introduction to Experimental Design*, volume 1. John Wiley & Sons, INC, New York, 1994.

[71] R. E. Kirk. *Experimental Design*. Wadsworth Pub Co, 1995.

[72] W. Y. Fowlkes and C. M. Creveling. *Engineering Methods for Robust Design: Using Taguchi Methods in Technology and Product Development*. Addison - Wesley Publishing Company, New York, 1995.

[73] G. W. Oehlert. *A First Course in Design and Analysis of Experiments*. WH Freeman New York, 2000.

[74] ReliaSoft. DOE++ User's Guide: Chapter 7 - Two Level Factorial Experiments. `http://www.weibull.com/DOEWeb/two_level_factorial_experiments.htm`. [Accessed Online: 2013, March 18].

[75] B. Kan and B. Yazici. A Study on 3-Level Full Factorial Design with 2 Factors. In *Optimal Design of Experiments – Theory and Application*, Vienna, Austria, September 2011.

[76] NIST/SEMATECH. e-Handbook of Statistical Methods: Three-Level Full Factorial Designs. `http://www.itl.nist.gov/div898/handbook/pri/section3/pri339.htm`. [Accessed Online: 2013, March 18].

[77] K. Yang and E. H. Basem. *Design for Six Sigma – A Roadmap for Product Development, Chapter 12: Fundamentals of Experimental Design*. McGraw-Hill Professional, 2nd edition, 2008.

[78] K. Bhutta. Taguchi Approach to Design of Experiments. Master's thesis, Department of Information Systems, Box 2042, College of Business Administration, Nicholls State University, Thibodaux, LA 70310, 2003.

[79] J. L. Meriam and L. G. Kraige. *Engineering Mechanics Dynamics*, volume 2. John Wiley & Sons, INC, 6th edition, 2008.

Appendices

Appendix A

Model Parameters

Density of air ρ, (kg/m^3):	1.225
Gravitational acceleration g, (m/s^2):	9.81
Reference area of parafoil S, (m^2):	6.026
Canopy chord length c, (m):	1.526
Canopy span b, (m):	3.950
Parafoil line length L, (m):	$(0.9 - 1.1) \times b$
Number of lines nl:	48
Line diameter d, (m):	0.002
Trim angle μ, $(^\circ)$:	9-13
Payload mass m_{pl}, (kg):	30
Pitch moment of inertia I_{yy}, $(kg.m^2)$:	1.84
Payload reference area S_{refpl}, (m^2):	0.229
Payload reference length X_{refpl}, (m):	0.71
Aspect ratio of payload $(\text{Æ}R_{pl})$:	2.2
x-distance from payload to hinge r_{HX}, (m):	-0.010
z-distance from payload to hinge r_{HZ}, (m):	-0.90
Aerodynamic coefficients:	$C_{L\alpha} = 2\pi$
	$C_{D\alpha} = 0$
	$C_{m\alpha} = -0.1$
	$C_{L0} = 0.1$
	$C_{D0} = 0.2$
	$C_{m0} = 0.1$
	$C_{DL} = 1$
	$C_{Lpl\alpha} = 1$
	$C_{D0pl} = 1$
	$C_{mpl\alpha} = 0.25$

Appendix B

Parafoil Avionics Ground Station Software Readme

Originally written by Gideon van der Kolf, Stellenbosch University, July 2013

1. **Set up environment**

Copy the *CharmanderData* folder to C:

The ground station software requires that the folder *CharmanderData* be in the C:\ drive. This folder contains data files (.cfg) that is used by the ground station application. This directory (C:\CharmanderData\) is also where the ground station will log session data. Each time the application is run, a new session folder is created. Folders are numbered starting "Session 1", etc.

2. **Run the application and set up connection**

Run "Parafoil_Ground_Station_V2.exe", set up COM port and start the on-board computer (OBC).

The ground station application, "Parafoil_Ground_Station_V2.exe", is in a folder along with some .dll files. Make sure another instance is not already running, and then double-click the application to run it.

When it opens, a new session is created. The number is displayed in the title bar (e.g. Session 4). Error and information messages are shown in the *Command History* and on the *Console* tab.

Select the COM port that the RF modem is connected to. A message in the *Command History* and should indicate a successful connection (or a failure) (Opened comms on port: COM #). When connected successfully, press *Reset OBC* and *Start OBC* to restart the OBC (On-board Computer). (*Command History* should indicate Avionics: Begin Setup).

If SD card errors occurred (messages in the *Command History* will indicate this), *Format* the SD card and restart the OBC. If formatting of the SD card is necessary, do it using the ground station application and **NOT** using a laptop. The command history should say "SD format complete" and (SD Idle). If OBC has not been started then format won't complete!!

If the communications link works and the OBC started successfully, all the boxes on the GUI will start displaying data. Check the *IMU* tabs to see if data is being streamed.

3. Start estimator and logging

Check IMU data, GPS lock. Initialise and start estimator. Start logging. Note session and log file numbers.

When the OBC has successfully been started, the *IMU* tabs should show the IMU data being streamed to the ground station. Wait until GPS lock has been obtained (The *Fix Type* box on the *IMU1 (Payload)* tab should display *3D*). On the *Estimator* tab, press *Initialise Estimator* and then *Enable Estimator*. The *Estimator States* values should start to converge.

Press *Start Logging* to start the SD card logging. The *Command History* will display a message that logging has started successfully and give the log file number. Record this log file number along with the ground station session number (displayed in the titlebar) somewhere with the current flight test number, for future reference. Generally, when the system loses power or when the SD card would pop out, it shouldn't go corrupt. The logger is designed so that the data would be logged up until the point where the power was lost, and there will be an additional few seconds of rubbish data, since the data file is allocated dynamically ahead of time.

4. Data plotting after the flight test

Copy data files from SD card. Run the extraction scripts in MATLAB. Plot the data.

Data is logged on-board at a high rate (50Hz) to the SD card. The data is also streamed down to the ground station at a lower rate. The ground station logs the received data, as well as the *Command History* (Error and information messages) to a session folder in *C:\CharmanderData* as described above.

The SD card data files should be sufficient for data processing. However, the ground station log data is useful in cases where the SD data was lost or corrupt, to see the error messages history of the ground station, and to analyse cases where there were communication failures.

The *FlightTestDataPlotting* folder contains scripts for extracting the ground station and SD card log files.

Plot SD card data

Edit *ExtractSDTelemetryData.m* to point to SD data file. Data is extracted to MATLAB workspace.

Copy the data file from the SD card to a known location. Edit *ExtractSDTelemetryData.m* to point to the data file. Run the script to extract the data into the MATLAB workspace, into a structure *SdtelemetryData*.

Explore the structure, or use the *plotSDTelemetryData* script to plot certain data.

Trimming the data to the actual flight

Plot accelerometers and OBC Time. Note index range of useful flight data.

If the SD card logging was started some time before the launch, a lot of the logged data is of little use and only a small portion contains actual flight data. To determine the range of useful flight data, plot the accelerometer data.

Plot_01_TimeAndAccel.m plots this. Accelerometer spikes should indicate the start and end of the flights. The *OBC Time* plot should be a steady increasing line. Jumps will indicate where the OBC was restarted. If the OBC was abruptly switched off (e.g. after a crash), the last few seconds of data might be invalid. This will be indicated by a jump in the *OBC Time* graph.

Record the *indexes* where the flight started and ended (Look at accelerometer spikes and jumps in the *OBC Time*). These indexes can now be used to only plot the useful range of data.

The *Plot_02_MAIN.m* script, for example, only plots a range of data. Change the variables *imin* and *imax* at the top of the file to the start and end indexes observed in the OBC Time and accelerometer plots.

Plot Ground station log data

Edit the *extractGStelemetry.m* script to point to the appropriate session folder. Run the script to extract the data to the MATLAB workspace. There are several *plot* scripts which will each plot certain data. Unlike with the SD data, each category of ground station log data (GPS, IMU, OBC, etc.) has its own time vector since all the data is not logged at the same frequency.

The *MAIN.m* script aids the process of selecting the useful flight data as mentioned above with the SD data. The script will plot the OBC Time and accelerometer data and ask the user to select a time span. It is also useful to check the ground station *history.txt* file in some cases from which the time of flight can be guessed.

Appendix C

Charging Batteries Procedure

Originally written by Tracy Booysen, University of Cape Town

Current batteries are 12V, 2Ah.
Maximum charge for one 12V battery is 13.6V.
To trickle charge the maximum current should be 0.2A.

To charge a single battery:

1. Get a DC power supply.
2. Get a set of power supply leads.
3. Set the voltage of the power supply to 13.6V using the voltage knob on the power supply.
4. Set the current knob all the way to zero (voltage will drop to nothing) then turn the knob a few degrees over until the voltage returns to the level you had set (i.e. 13.6V).
5. Insert the banana plug of the negative lead (black) into the negative terminal on the power supply.
6. Insert the banana plug of the positive lead (red) into the positive terminal on the power supply. (the +ve one not the earth/green one)
7. Touch the crocodile clips together to see the current limit.
8. While holding the crocodile clips together, adjust the current limit to 0.2A using the current knob - **be sure it is 0.2A and not 2A!!!** Release the crocodile clips and the voltage should return to 13.6V and the current to 0A.

9. Unplug the positive banana plug.
10. Attach the crocodile clip of the negative lead to the negative terminal of the battery and insulate the connection.
11. Attach the crocodile clip of the positive lead to the positive terminal of the battery and insulate the connection.
12. Now reinsert the positive banana plug into the positive terminal of the power supply.
13. The battery will begin drawing current, and the voltage will be limited to the current voltage level of the battery - **DO NOT ADJUST IT**
14. Now check the current and make sure it is 0.2A - If you need to adjust it **BE VERY CAREFUL THE KNOB IS VERY SENSITIVE, TURN SLOWLY.**
15. The batteries would take 10 hours to charge fully from depletion. As they should never be fully depleted, it make take less time.
16. When the voltage indicates 13.6V on the power supply, the battery is fully charged. It is OK if it is 13.5V.

NEVER LEAVE THE BATTERIES CHARGING UNATTENDED AND CHECK THE VOLTAGES AND CURRENTS REGULARLY

Appendix D

January 2014 Flight Tests

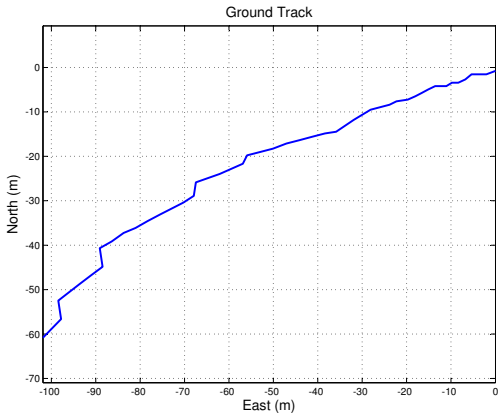

(a) Ground Track of Flight Path

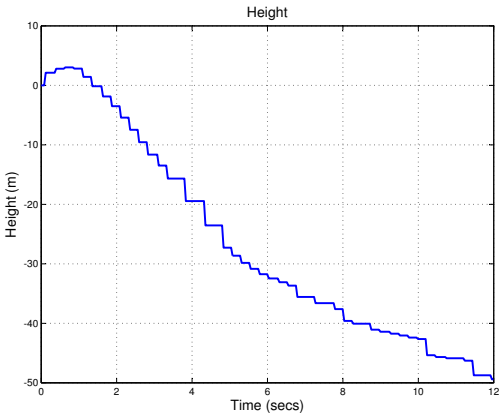

(b) Elevation vs. Time

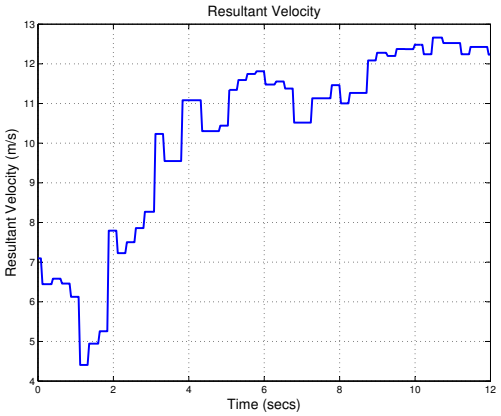

(c) Resultant Velocity vs. Time

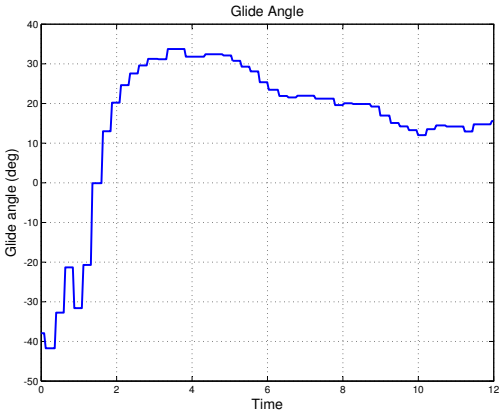

(d) Glide Angle vs. Time

Figure D.1: January Flight Test 1

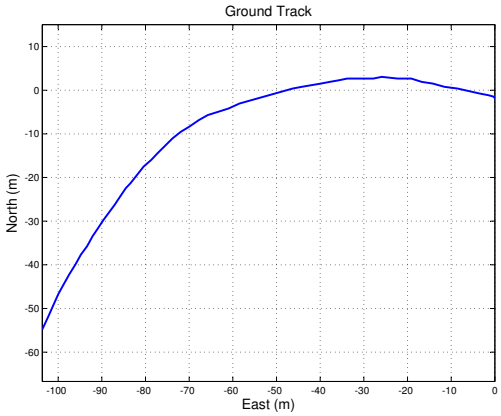

(a) Ground Track of Flight Path

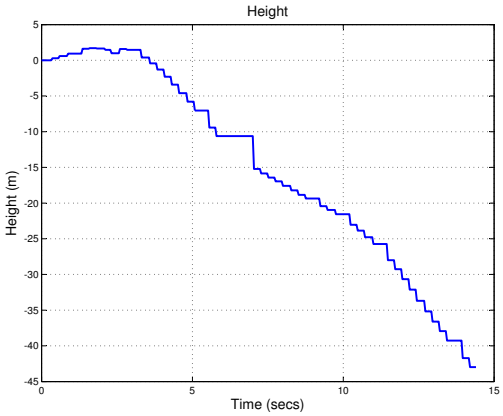

(b) Elevation vs. Time

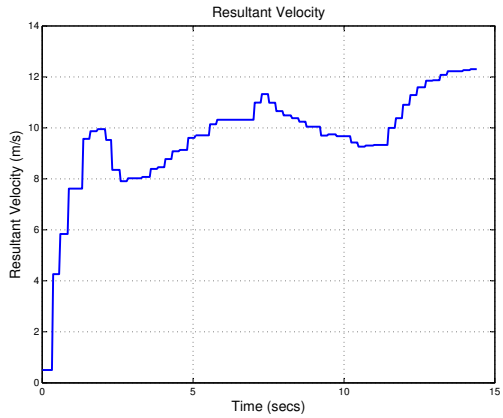

(c) Resultant Velocity vs. Time

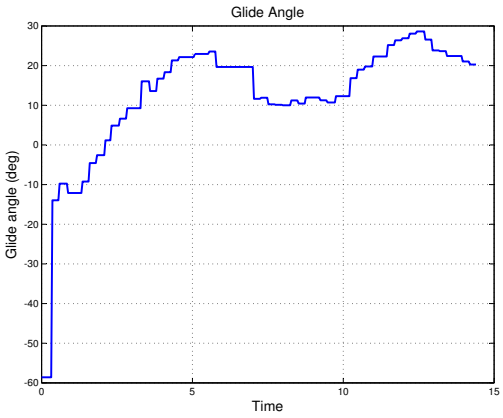

(d) Glide Angle vs. Time

Figure D.2: January Flight Test 2

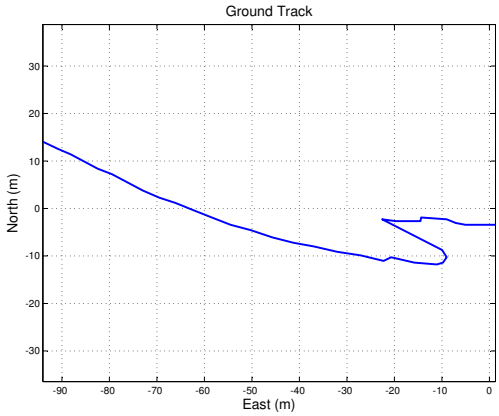

(a) Ground Track of Flight Path

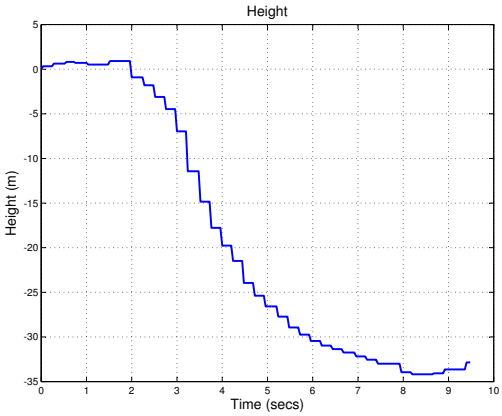

(b) Elevation vs. Time

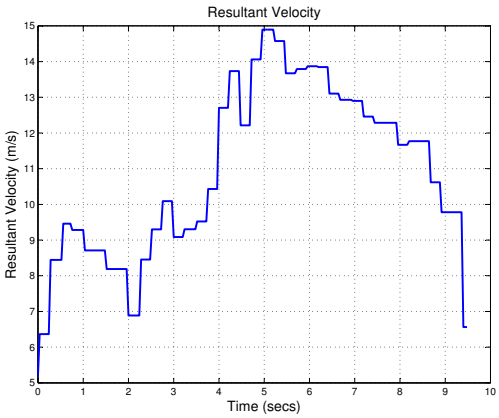

(c) Resultant Velocity vs. Time

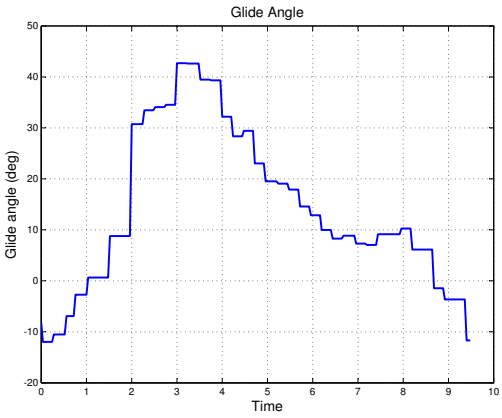

(d) Glide Angle vs. Time

Figure D.3: January Flight Test 3

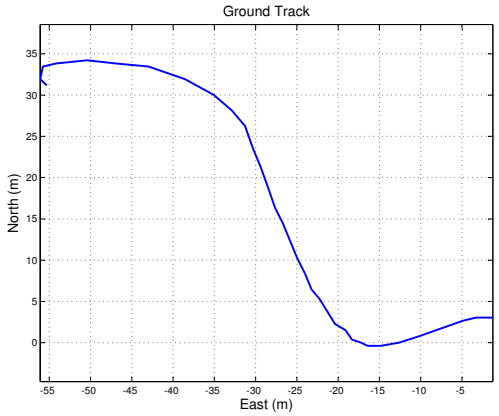

(a) Ground Track of Flight Path

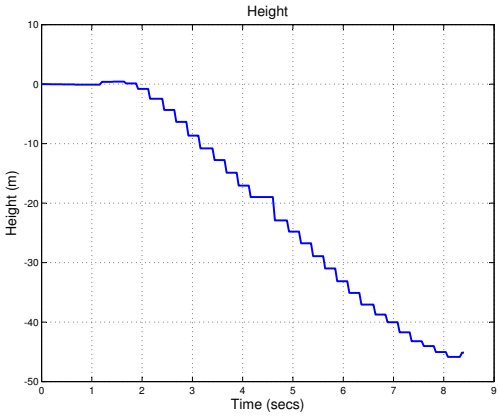

(b) Elevation vs. Time

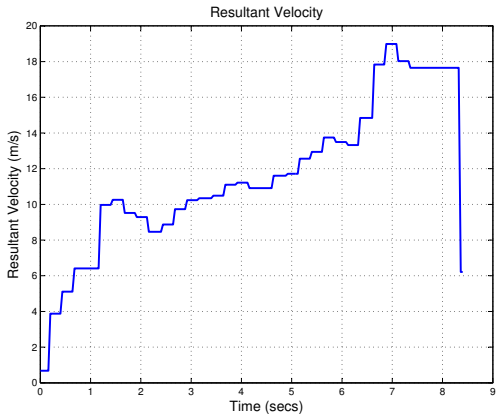

(c) Resultant Velocity vs. Time

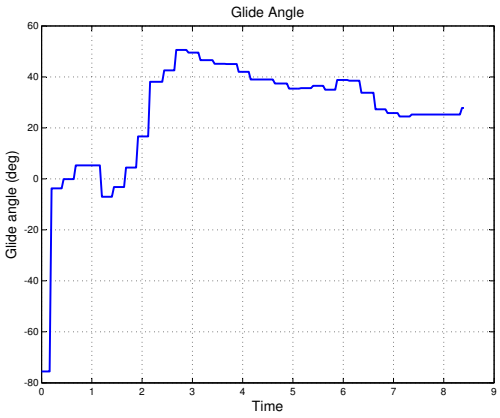

(d) Glide Angle vs. Time

Figure D.4: January Flight Test 5

Appendix E

Simulation Results

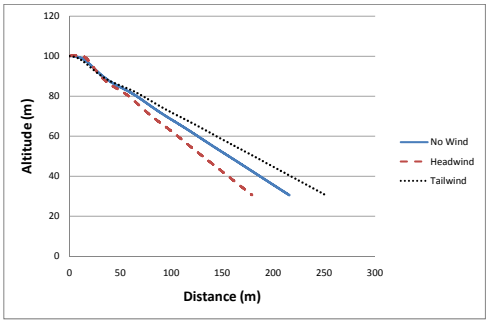

(a) Run 2

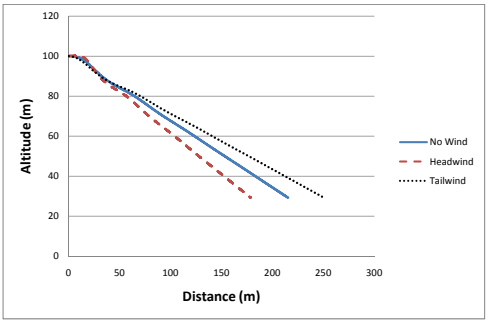

(b) Run 3

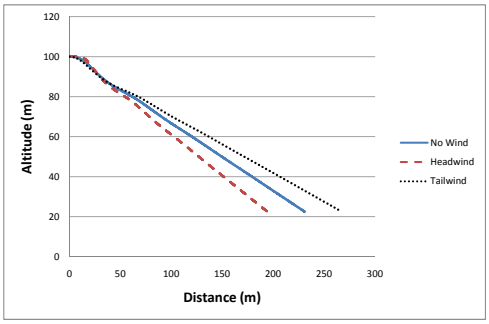

(c) Run 4

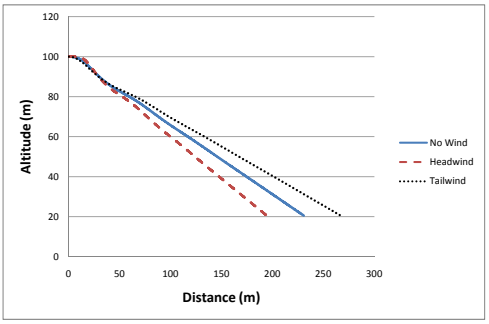

(d) Run 5

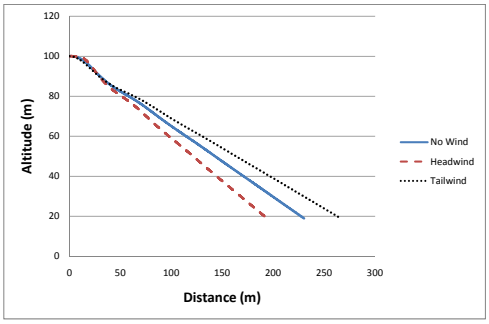

(e) Run 6

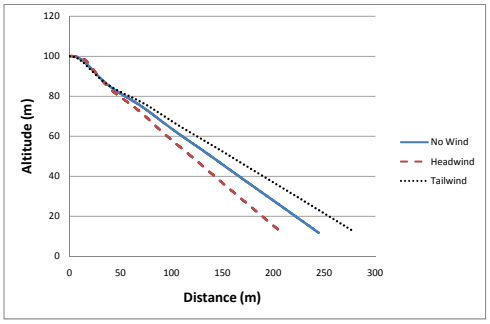

(f) Run 7

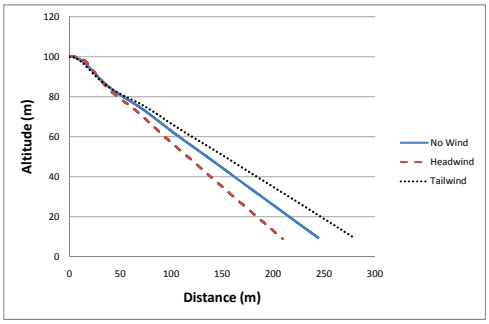

(g) Run 8

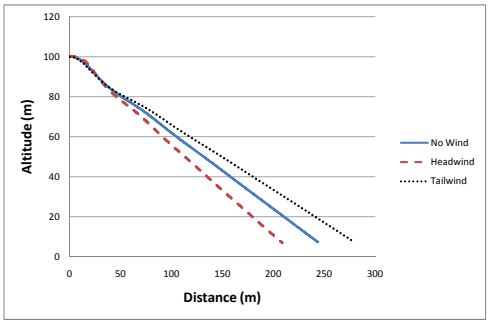

(h) Run 9

Figure E.1: Effect of Mean Wind on Altitude and Distance

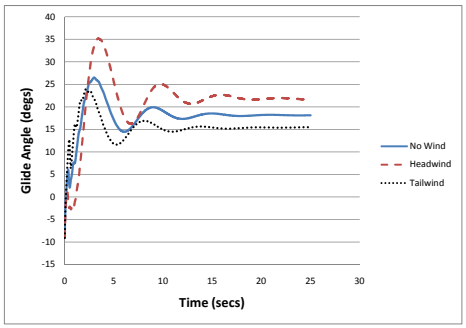

(a) Run 2

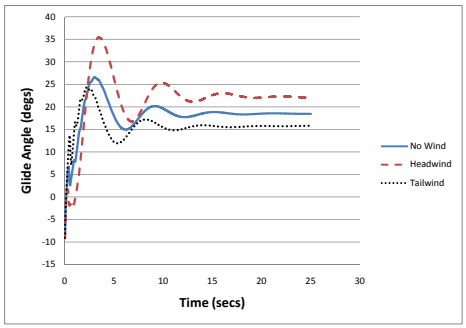

(b) Run 3

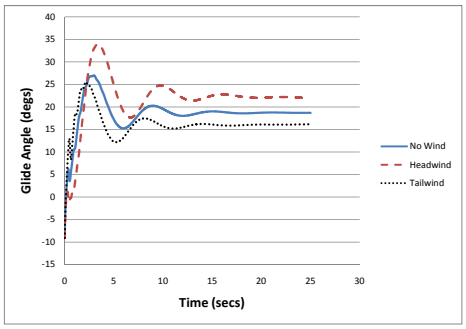

(c) Run 4

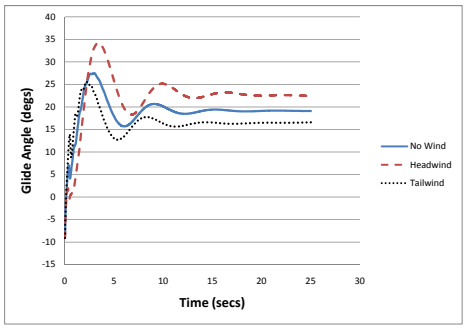

(d) Run 5

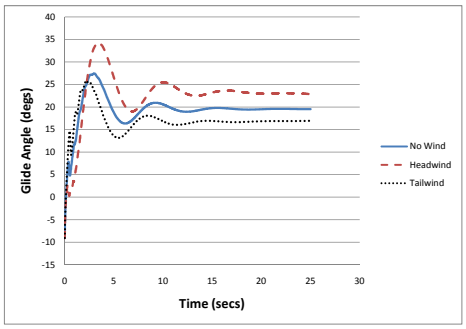

(e) Run 6

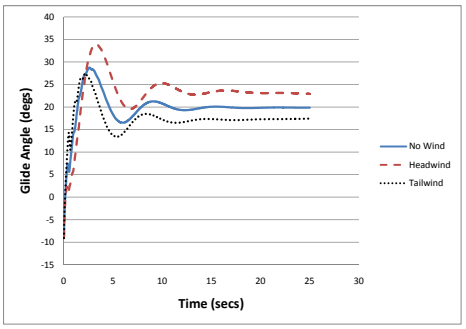

(f) Run 7

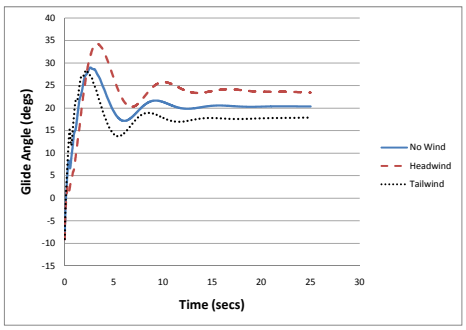

(g) Run 8

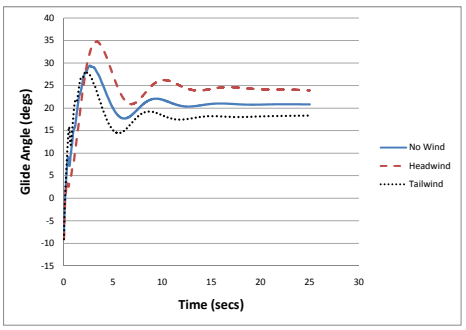

(h) Run 9

Figure E.2: Effect of Mean Wind on Absolute Glide Angle

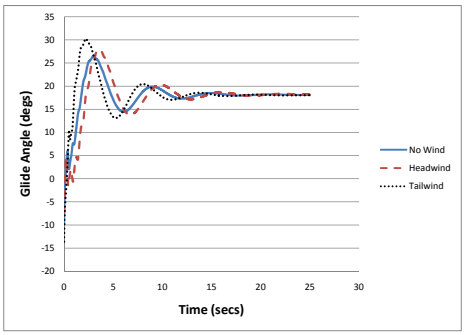

(a) Run 2

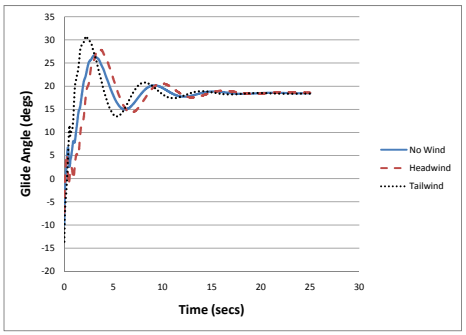

(b) Run 3

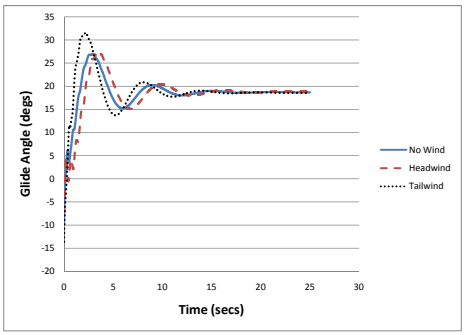

(c) Run 4

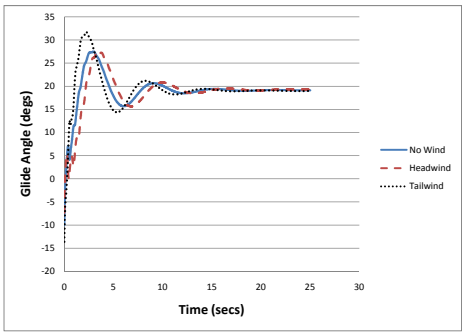

(d) Run 5

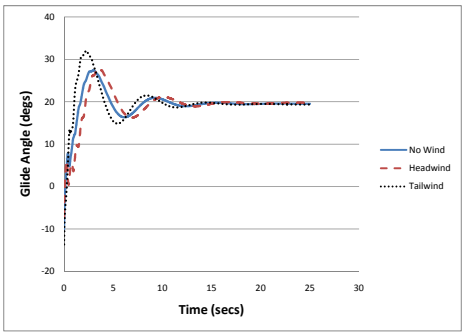

(e) Run 6

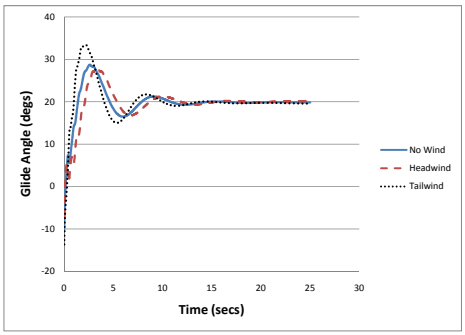

(f) Run 7

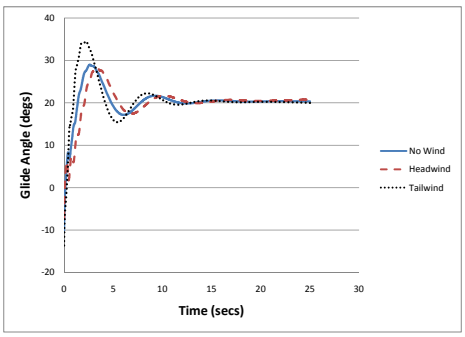

(g) Run 8

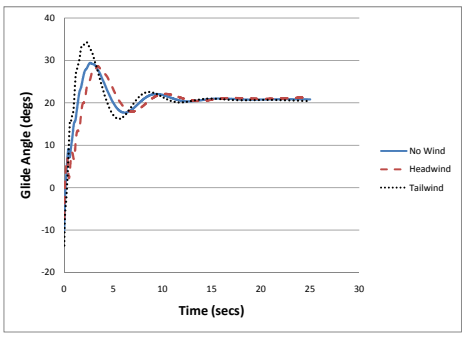

(h) Run 9

Figure E.3: Effect of Mean Wind on Relative Glide Angle

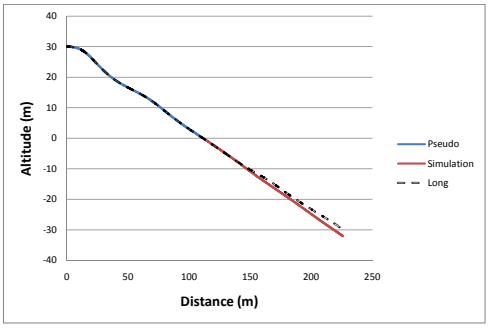

(a) Run 2

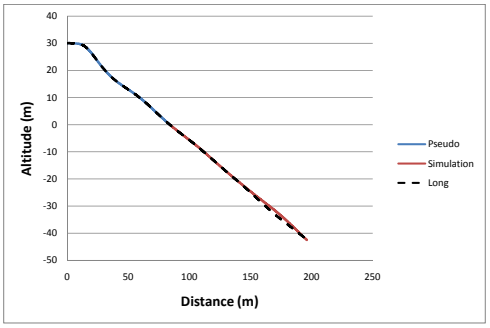

(b) Run 3

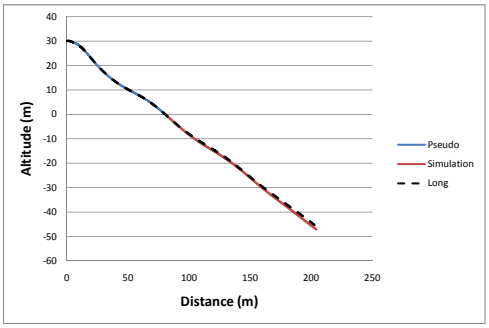

(c) Run 4

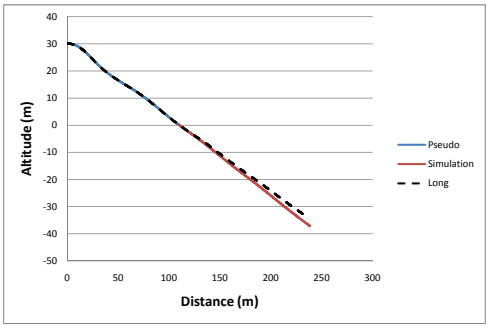

(d) Run 5

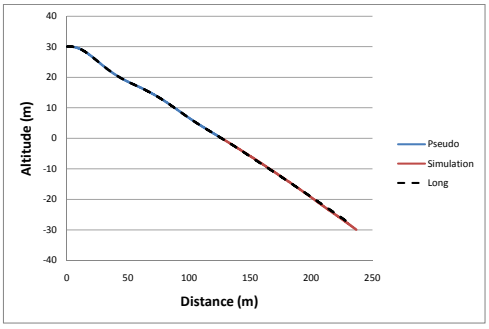

(e) Run 6

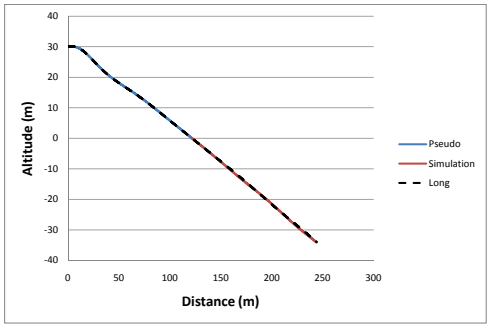

(f) Run 7

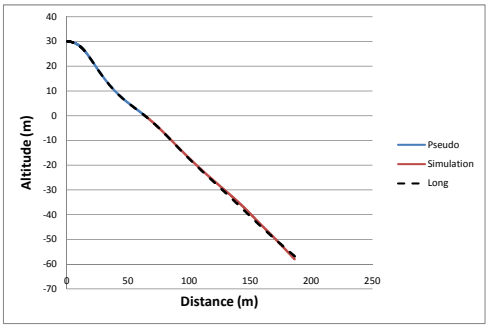

(g) Run 8

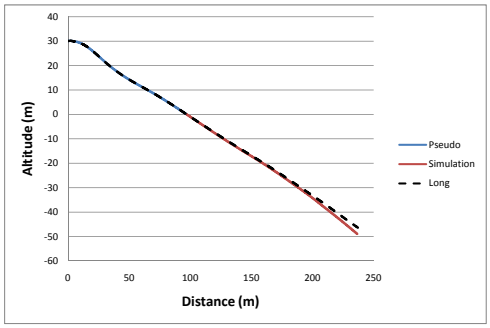

(h) Run 9

Figure E.4: Error Effect of Light Turbulence on Altitude and Distance

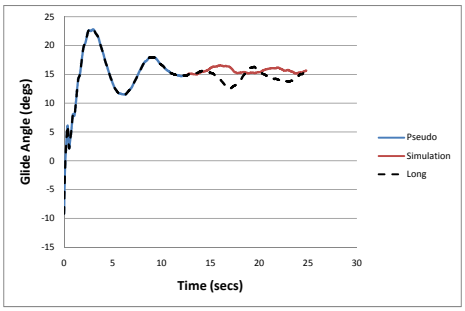

(a) Run 2

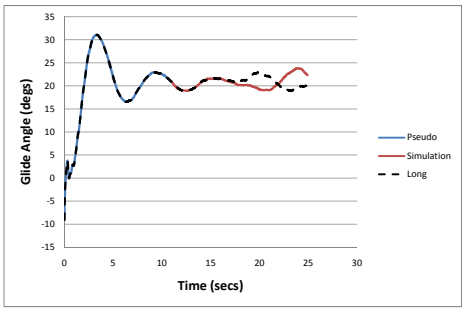

(b) Run 3

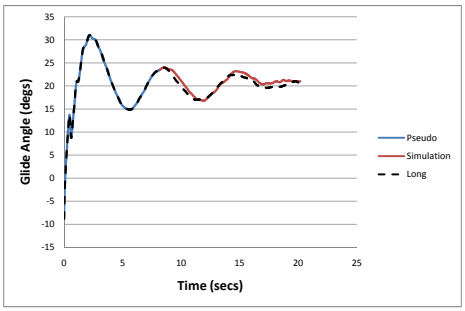

(c) Run 4

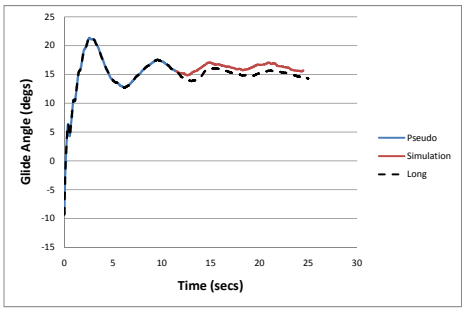

(d) Run 5

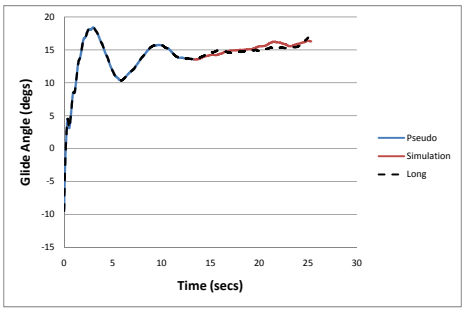

(e) Run 6

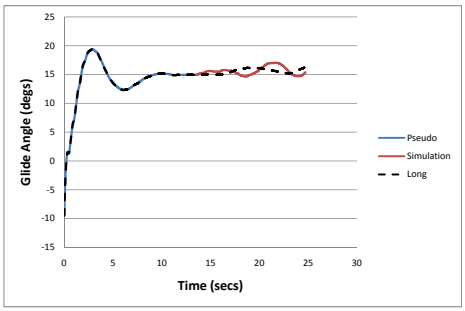

(f) Run 7

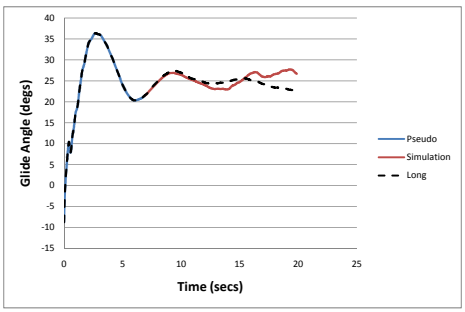

(g) Run 8

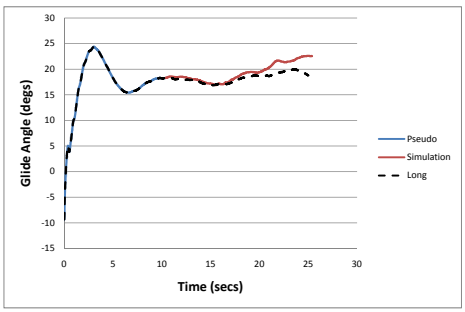

(h) Run 9

Figure E.5: Error Effect of Light Turbulence on Absolute Glide Angle

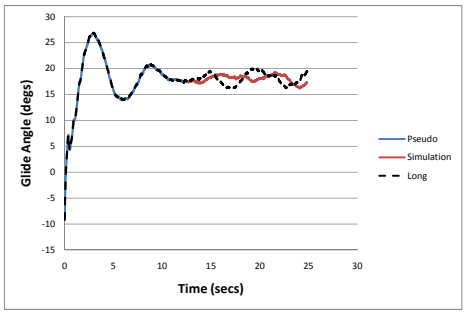

(a) Run 2

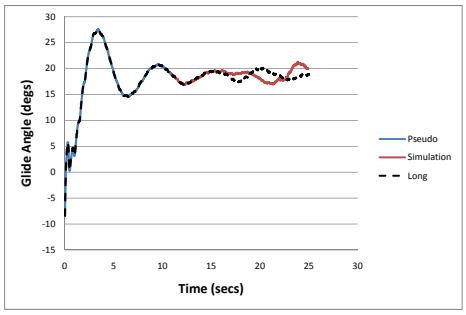

(b) Run 3

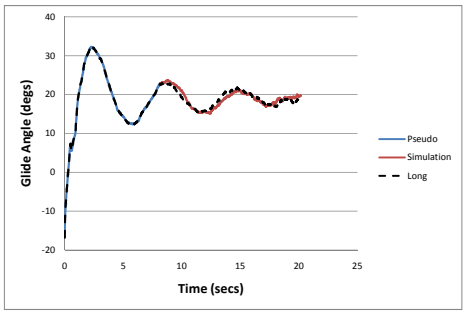

(c) Run 4

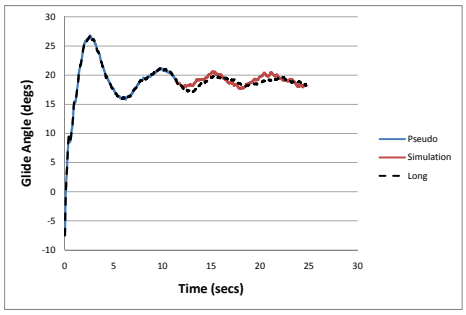

(d) Run 5

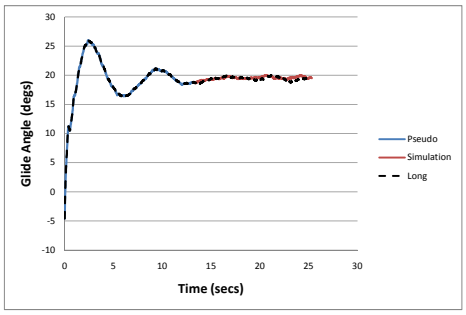

(e) Run 6

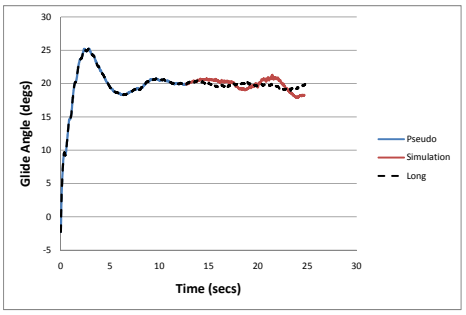

(f) Run 7

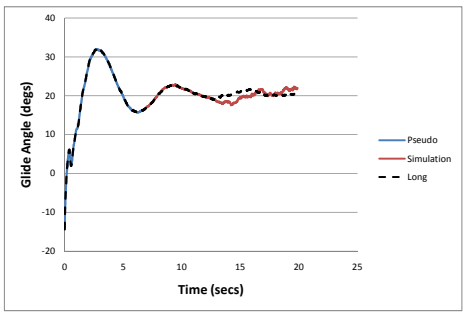

(g) Run 8

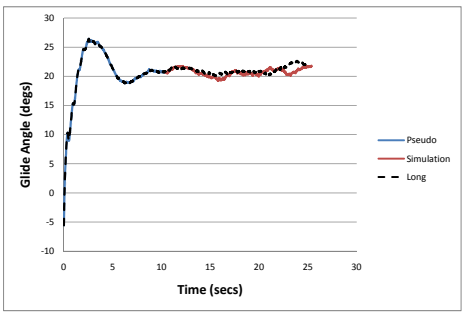

(h) Run 9

Figure E.6: Error Effect of Light Turbulence on Relative Glide Angle

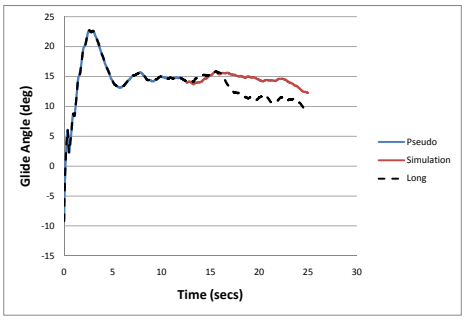

(a) Run 2

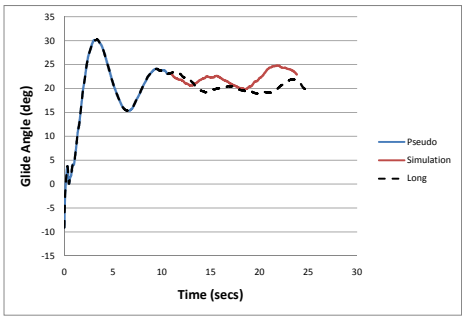

(b) Run 3

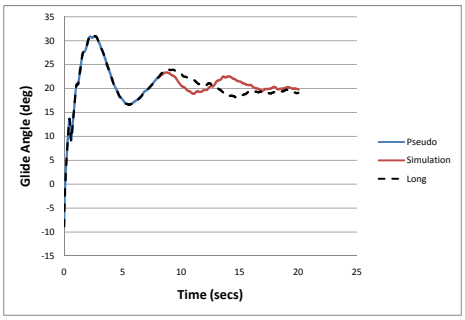

(c) Run 4

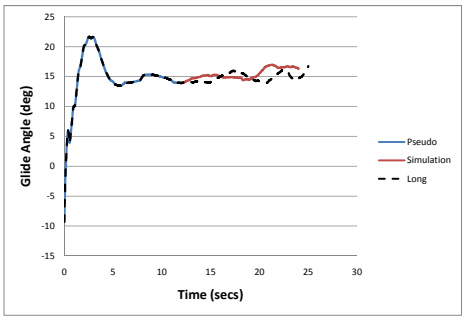

(d) Run 5

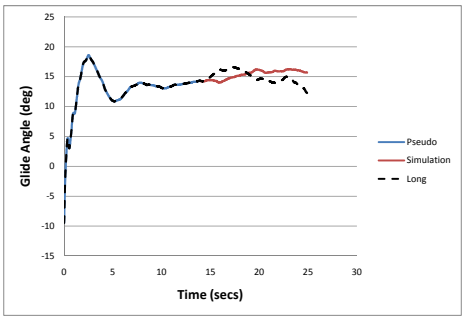

(e) Run 6

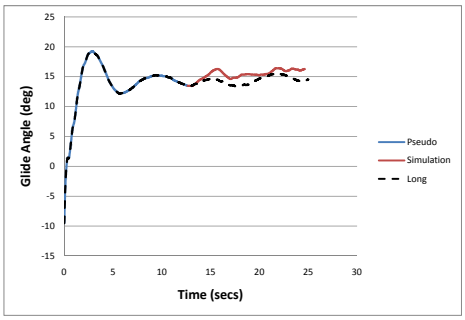

(f) Run 7

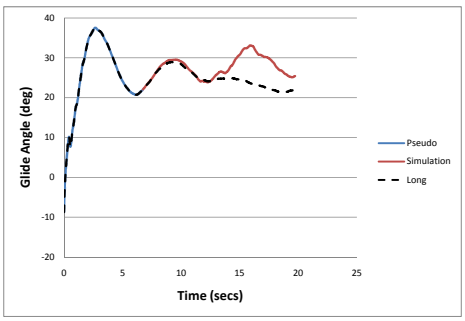

(g) Run 8

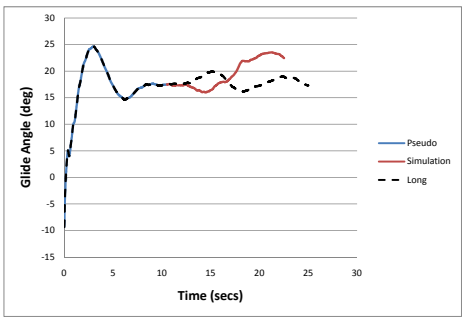

(h) Run 9

Figure E.7: Error Effect of Moderate Turbulence on Absolute Glide Angle

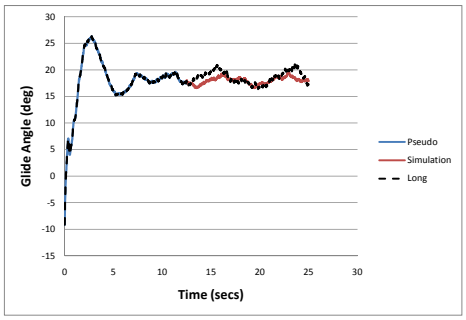

(a) Run 2

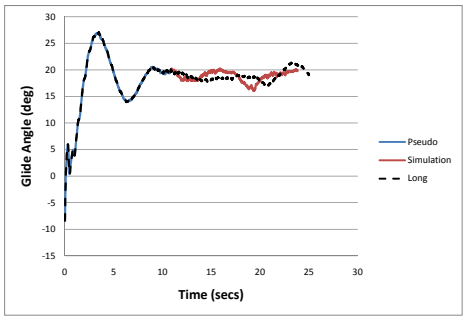

(b) Run 3

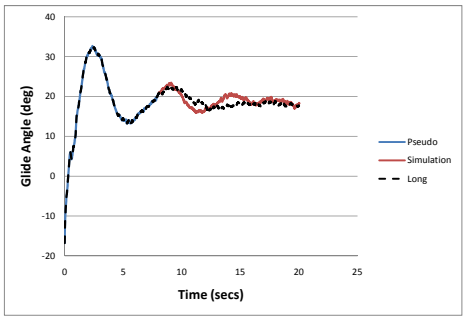

(c) Run 4

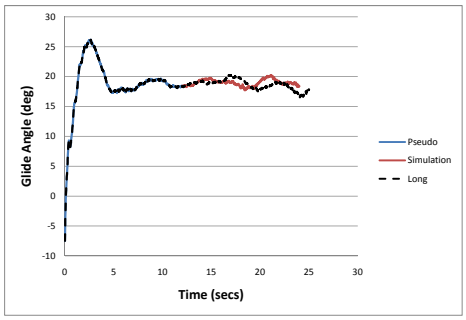

(d) Run 5

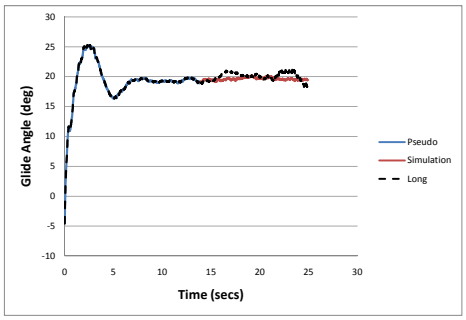

(e) Run 6

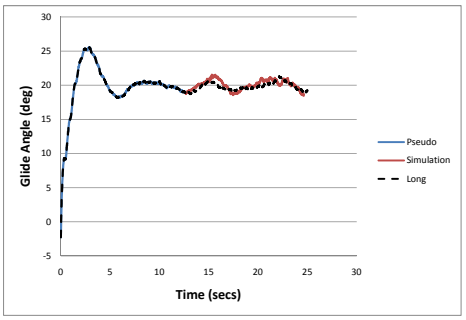

(f) Run 7

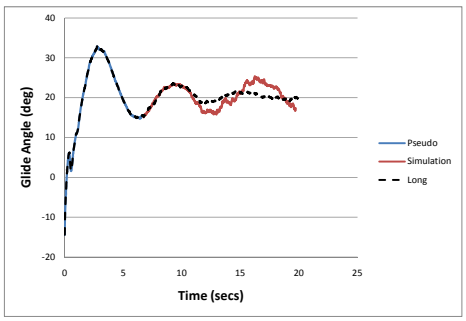

(g) Run 8

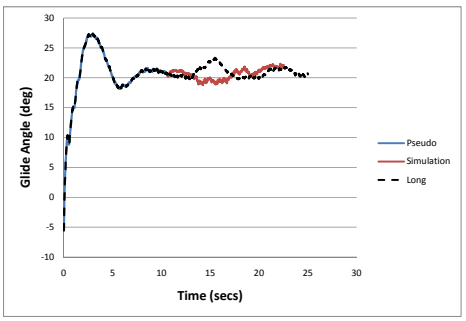

(h) Run 9

Figure E.8: Error Effect of Moderate Turbulence on Relative Glide Angle

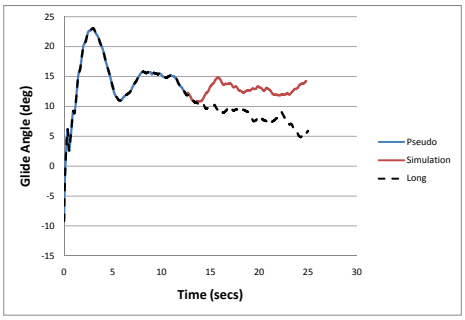

(a) Run 2

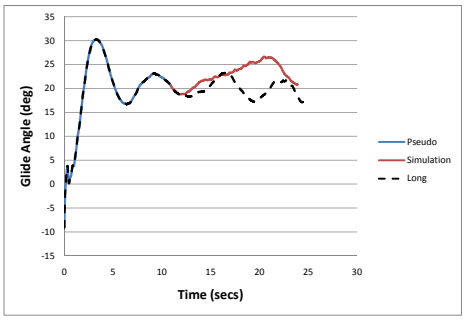

(b) Run 3

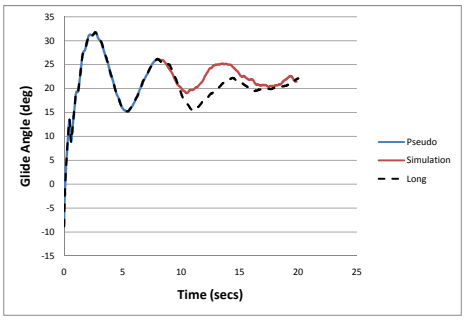

(c) Run 4

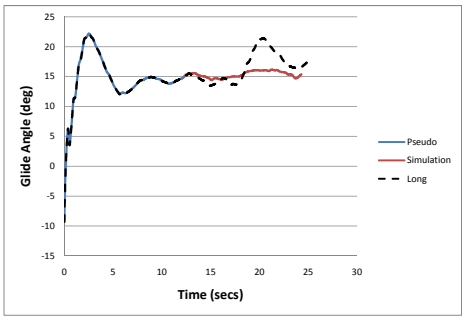

(d) Run 5

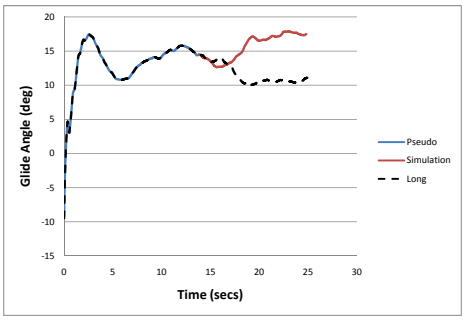

(e) Run 6

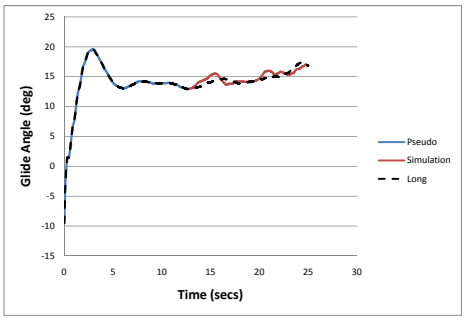

(f) Run 7

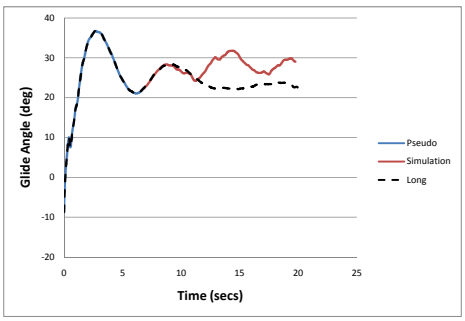

(g) Run 8

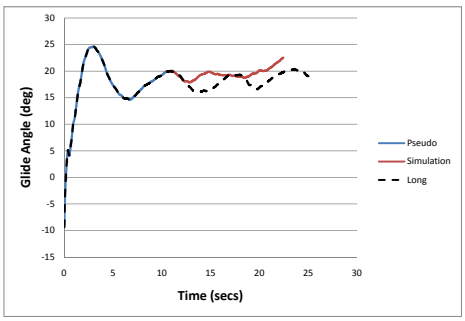

(h) Run 9

Figure E.9: Error Effect of Severe Turbulence on Absolute Glide Angle

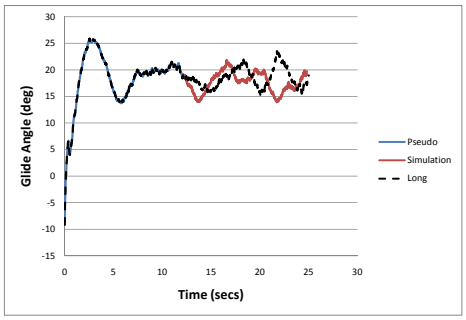

(a) Run 2

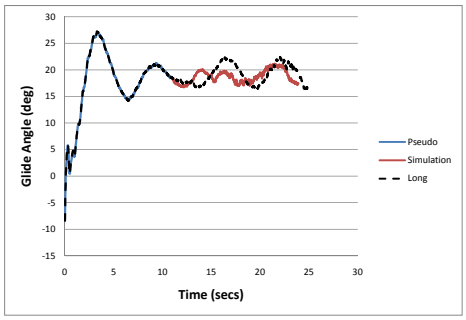

(b) Run 3

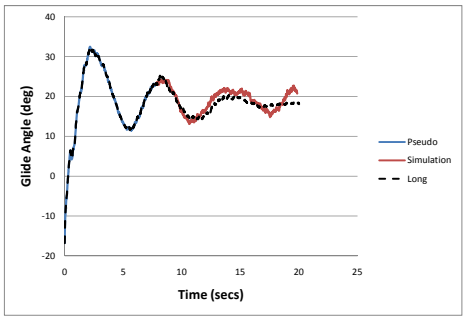

(c) Run 4

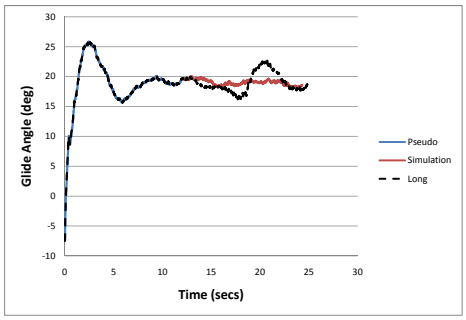

(d) Run 5

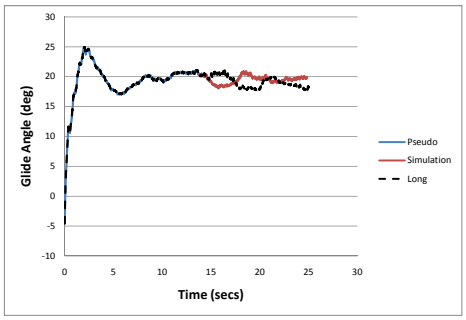

(e) Run 6

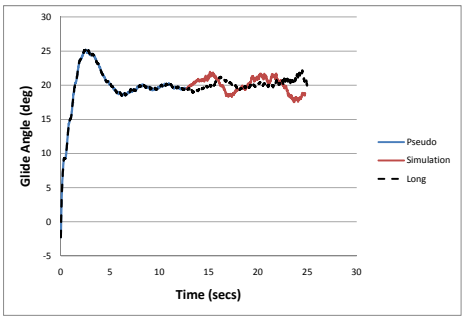

(f) Run 7

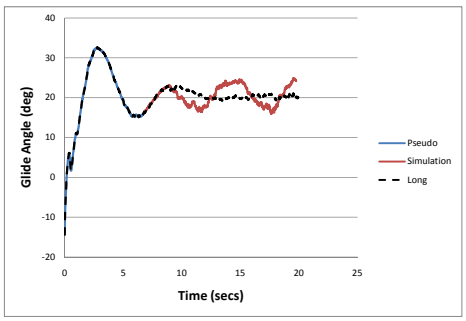

(g) Run 8

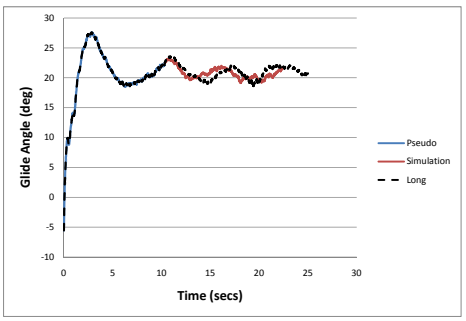

(h) Run 9

Figure E.10: Error Effect of Severe Turbulence on Relative Glide Angle

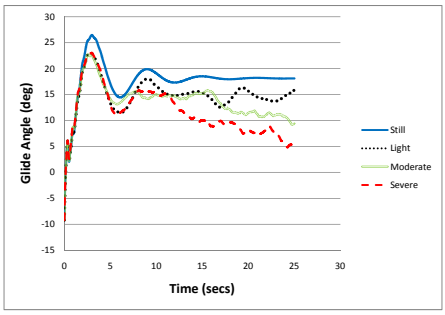

(a) Run 2

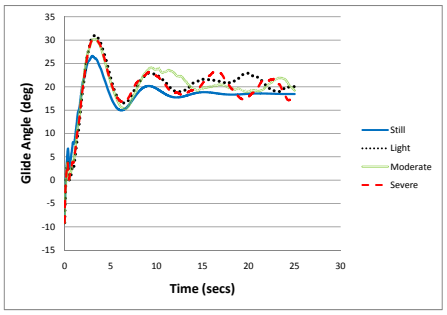

(b) Run 3

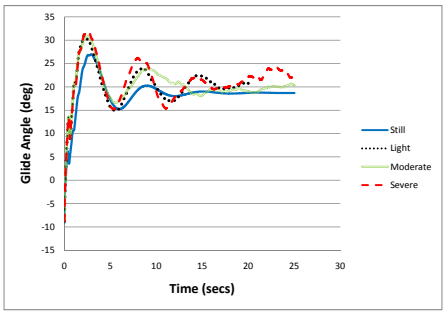

(c) Run 4

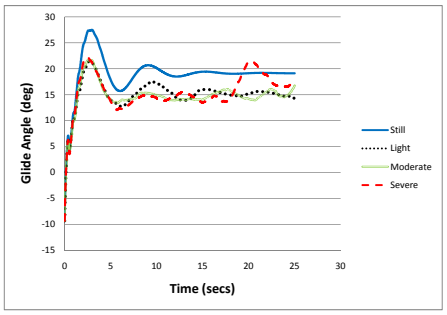

(d) Run 5

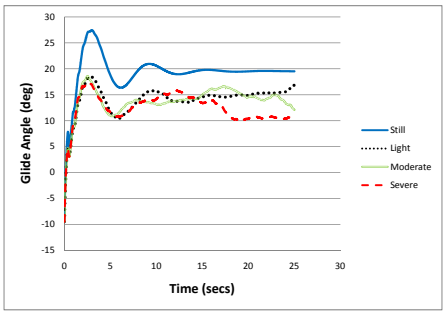

(e) Run 6

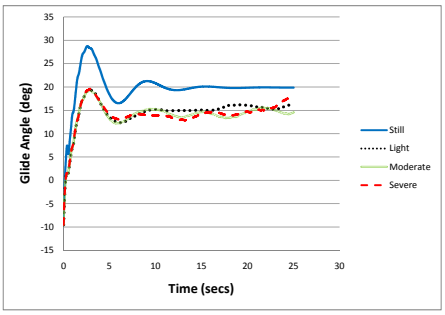

(f) Run 7

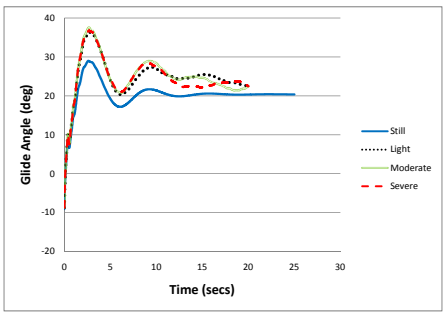

(g) Run 8

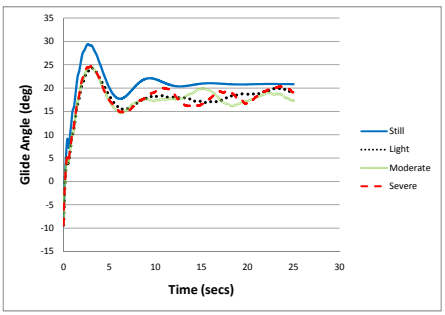

(h) Run 9

Figure E.11: Effect of Turbulence on Absolute Glide Angle

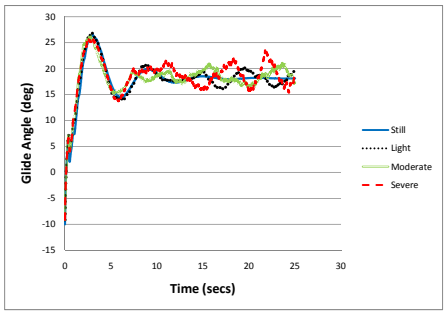

(a) Run 2

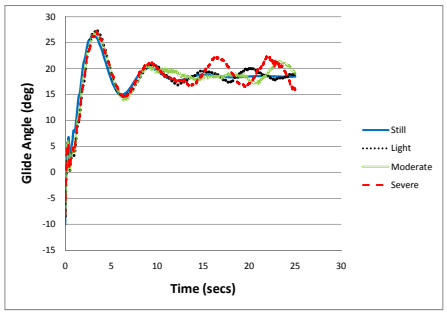

(b) Run 3

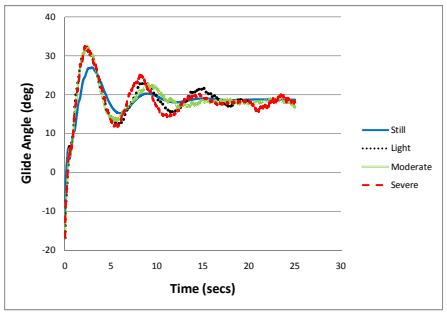

(c) Run 4

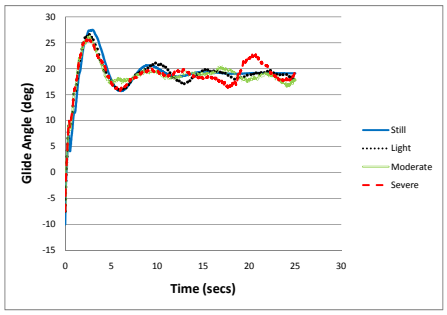

(d) Run 5

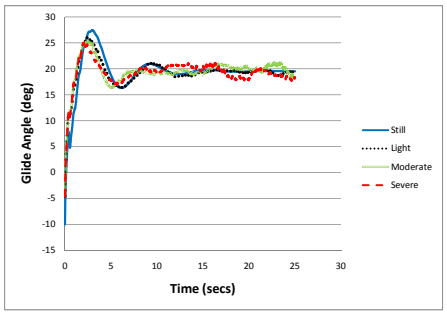

(e) Run 6

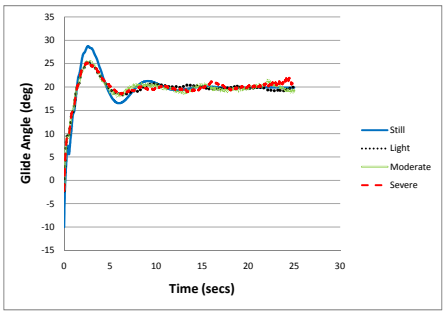

(f) Run 7

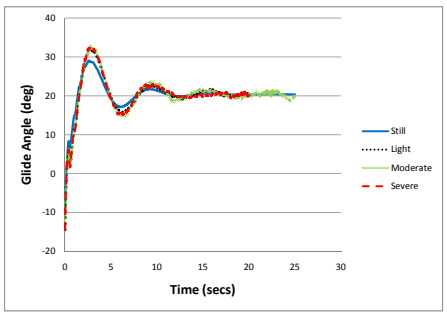

(g) Run 8

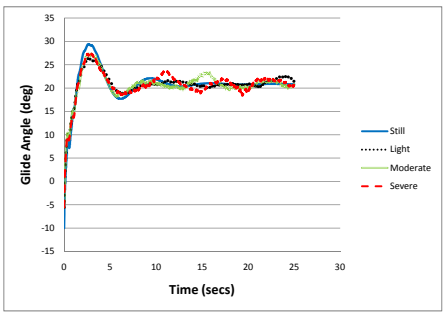

(h) Run 9

Figure E.12: Effect of Turbulence on Relative Glide Angle

Appendix F

Determine Aerodynamic Coefficients from IMU and Photography more Accurately

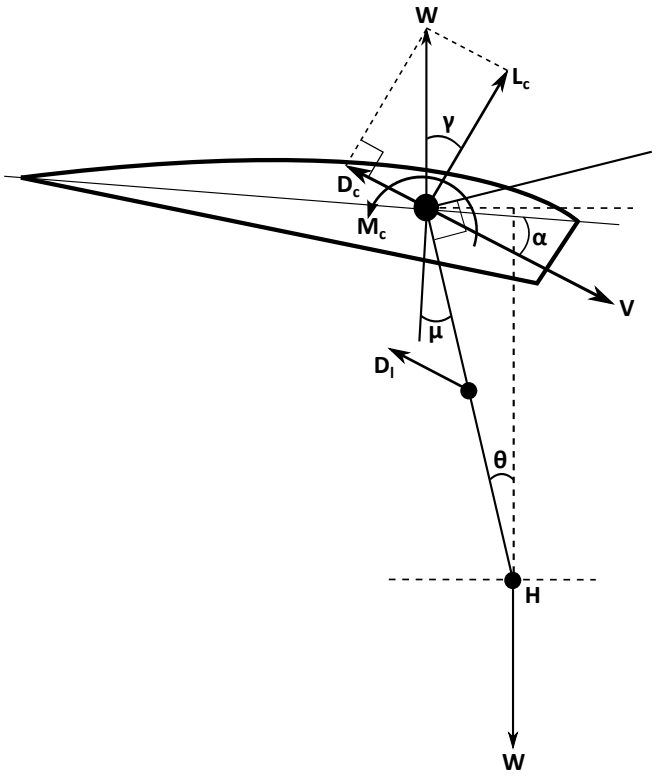

Figure F.1: Simplified Schematic of Parafoil in Steady State Glide

From force balance in steady state glide (Refer to Fig. F.1):

$$\text{Total System Lift } L = L_c = W\cos\gamma \tag{F.1}$$

$$\text{Total System Drag } D = D_c + D_l = W\sin\gamma \tag{F.2}$$

$$W^2 = L^2 + D^2 \tag{F.3}$$

$$\tan\gamma = \frac{D}{L} \tag{F.4}$$

For the parafoil:

$$\frac{1}{2}\rho V^2 C_L S = L_c = W\cos\gamma \tag{F.5}$$

$$\frac{1}{2}\rho V^2 C_D S = D_c = W\sin\gamma - D_l \tag{F.6}$$

Where:

$$\text{Line Drag } D_l = \frac{1}{2}\rho V^2 C_{DL} n d L \tag{F.7}$$

Therefore:

$$C_L = \frac{W\cos\gamma}{\frac{1}{2}\rho V^2 S} \tag{F.8}$$

$$C_D = \frac{W\sin\gamma - D_l}{\frac{1}{2}\rho V^2 S} \tag{F.9}$$

Also

$$C_L = C_{L0} + C_{L\alpha}\times\alpha \tag{F.10}$$

$$C_D = C_{D0} + \frac{{C_L}^2}{\pi \not{A} R} \tag{F.11}$$

Equation F.10 has two unknowns, namely C_{L0} and $C_{L\alpha}$, therefore two equations are needed. If two flight tests are conducted at two different trim settings, the IMU and photography can be used to accurately determine values for glide angle, angle of attack and velocity for each flight test. With this information, two equations of F.10 can be generated.

$$C_{L1} = C_{L0} + C_{L\alpha}\times\alpha_1 \tag{F.12}$$

$$C_{L2} = C_{L0} + C_{L\alpha}\times\alpha_2 \tag{F.13}$$

From Equation F.12:

$$C_{L0} = C_{L1} - C_{L\alpha}\times\alpha_1 \tag{F.14}$$

Substituting Equation F.14 into F.13:

$$C_{L\alpha} = \frac{C_{L1} - C_{L2}}{\alpha_1 - \alpha_2} \tag{F.15}$$

And substituting Equation F.15 back into F.14:

$$C_{L0} = C_{L1} - \alpha_1 \left(\frac{C_{L1} - C_{L2}}{\alpha_1 - \alpha_2} \right) \tag{F.16}$$

From Equation F.11, C_{D0} can be determined as follows:

$$C_{D0} = C_{D1} - \frac{{C_{L1}}^2}{\pi \mathcal{AR}} = C_{D2} - \frac{{C_{L2}}^2}{\pi \mathcal{AR}} \tag{F.17}$$

Similarly, from moment balance in steady state glide (Refer to Fig. F.1), C_{m0} and $C_{m\alpha}$ can be determined as follows:

$$M_c = \frac{R}{2} D_l \cos(\alpha + \mu) + WR \sin\theta \tag{F.18}$$

Therefore:

$$C_m = \frac{M_c}{\frac{1}{2}\rho V^2 Sc} \tag{F.19}$$

Also

$$C_m = C_{m0} + C_{m\alpha} \times \alpha \tag{F.20}$$

Two equations of F.20 can be generated for two flight tests.

$$C_{m1} = C_{m0} + C_{m\alpha} \times \alpha_1 \tag{F.21}$$

$$C_{m2} = C_{m0} + C_{m\alpha} \times \alpha_2 \tag{F.22}$$

Similarly, C_{m0} and $C_{m\alpha}$ can be expressed as follows:

$$C_{m\alpha} = \frac{C_{m1} - C_{m2}}{\alpha_1 - \alpha_2} \tag{F.23}$$

$$C_{m0} = C_{m1} - \alpha_1 \left(\frac{C_{m1} - C_{m2}}{\alpha_1 - \alpha_2} \right) \tag{F.24}$$

APPENDIX F. DETERMINE AERODYNAMIC COEFFICIENTS FROM IMU AND PHOTOGRAPHY MORE ACCURATELY

Appendix G

CD-ROM Contents

Attached to the inner back cover of this bound dissertation is a CD-ROM with the following:

- Soft copy of dissertation (pdf format)
- 4 MATLAB aerodynamic models (no wind, wind, turbulence and wind + turbulence)
- Excel spreadsheets of data analysis and DOE analyses
- Some images and videos taken during the experimental flight tests
- Data files logged during experimental flight tests
- MATLAB scripts to plot flight test data (courtesy of Gideon van der Kolf - Stellenbosch University)
- Parafoil avionics ground station software (courtesy of Gideon van der Kolf - Stellenbosch University)